# Interaction, directed assembly and electrophoretic mobility of silica micro and nano-rods in nematic liquid crystals



Ph.D. Thesis

Muhammed Rasi. M (15PHPH14)

Supervisor: Prof. Surajit Dhara

School of Physics University of Hyderabad Hyderabad, India

November 2021

# Interaction, directed assembly and electrophoretic mobility of silica micro and nano-rods in nematic liquid crystals

A thesis submitted for the award of the degree of

Doctor of Philosophy in Physics

by

# Muhammed Rasi. M 15PHPH14



Supervisor: Prof. Surajit Dhara

School of Physics
University of Hyderabad
Hyderabad, India
November 2021

# $$^{ m TO}$$ My family and friends

# Declaration

I, Muhammed Rasi. M, hereby declare that this Ph.D. thesis entitled "Interaction, directed assembly and electrophoretic mobility of silica micro and nano-rods in nematic liquid crystals" has been carried out by me under the supervision of Prof. Surajit Dhara, School of Physics, University of Hyderabad, as per the Ph.D. ordinances of the University. I declare to the best of my knowledge that, this is a bonafide work and no part of this thesis has been submitted for the award of a research degree by any other University.

A report on plagiarism statistics from the University Librarian is enclosed.

(Muhammed Rasi. M)

Reg. No: 15PHPH14

Date: 16/11/2021

Place: Hyderabad



# Certificate

This is to certify that the thesis entitled "Interaction, directed assembly and electrophoretic mobility of silica micro and nano-rods in nematic liquid crystals" submitted by Muhammed Rasi. M bearing Reg. No. 15PHPH14 in fulfilment of the requirements for the award of Doctor of Philosophy in Physics is a bonafide work carried out by him under my supervision and guidance.

This thesis is free from plagiarism and has not been submitted previously in part or in full to this or any other university or institution for the award of any degree or diploma.

Further, the student has the following publications before the submission of the thesis for adjudication.

- Muhammed Rasi M, K. P. Zuhail, Arun Roy and Surajit Dhara,
   N-SmA-SmC phase transitions probed by a pair of elastically bound colloids.
   Physical Review E 97, 032702(2018). Chapter-6.
- Muhammed Rasi M, Ravi Kumar Pujala and Surajit Dhara,
   Colloidal analogues of polymer chains, ribbons and 2D crystals employing orientations and interactions of nano-rods dispersed in a nematic liquid crystal.
   Scientific reports 9, 4652(2019). Chapter-3.
- 3. Muhammed Rasi M, Ravi Kumar Pujala, Sathyanarayana Paladugu and Surajit Dhara

Interactions of charged microrods in chiral nematic liquid crystals.

Physical Review E **104**, 014706(2021). Chapter-4.

Muhammed Rasi M, Ravi Kumar Pujala and Surajit Dhara,
 Electrophoretic mobility of silica micro and nano-rods in nematic liquid crystals.
 Chapter-5 (manuscript under preparation).

Further, the student has passed the following courses towards the fulfilment of coursework required for Ph.D.

SN	Course Code	Name	Credits	Pass/Fail
1)	PY801	Advanced Quantum Mechanics	4	Pass
2)	PY803	Advanced Statistical Mechanics	4	Pass
3)	PY804	Advanced Electromagnetic Theory	4	Pass
4)	PY821	Research Methodology	4	Pass

Journes Roju)

Prof. K. C. James Raju

Dean.

School of Physics,

University of Hyderabad.

DEAN

School of Physics University of Hyderabad Hyderabad-500 046, INDIA

Date: 16-11. 2021

Prof. Surajit Dhara

Thesis supervisor

School of Physics

University of Hyderabad.

Dr. Surajit Dhara
Professor
School of Physics
University of Hyderabad
Hyderabad-500 046. INDIA.

# Acknowledgement

Undertaking this Ph.D. has been a truly life-changing experience for me and it would not have been possible to do without the support and guidance that I received from many people.

My deep gratitude goes first to Prof. Surajit Dhara, who expertly guided me through my research and who shared the excitement of five years of discovery. His unwavering enthusiasm for physics kept me constantly engaged with my research. This work would not have been finished without his advice and constant feedback. I pay my high respect and regards to his dedication towards scientific research.

I would like to thank my doctoral committee members, Prof. S. Srinath, Prof. B.V.R. Tata, and Dr. G. Venkataiah, for their expert and helpful academic discussions. My special and sincere thanks go to Dr. Ravi Kumar Pujala, IISER Tirupati, for providing the samples. I thank former Deans, Prof. R. Singh, Prof. Bindu A. Bamba, Prof. V. Seshu Bai, Prof. Ashok Chatterjee and present Dean Prof. K. C. James Raju, for providing the necessary facilities in the school. I would also like to thank other faculty members and staffs for their valuable suggestions.

I am grateful for the funding for my Ph.D. from DST-SERB and CSIR for my JRF and D-SRF fellowships.

My sincere gratitude to all my research lab colleagues, Zuhail K. P., Rasna M. V., Rasmita Sahoo, P. Sathyanarayana, Junaid Ahmad Sofi, Dinesh Kumar Sahu, Praveen Kumar, Devika V. S., Abhinash and Archana for their valuable suggestions and fruitful interactions. I could not have completed this journey without the support of my friends: Avisek, Zahid, Manasa, Leela, Nilanjan, Bappaditya, Naresh, Abu Taher, Sujai, Rajesh, Hemant, Rashmi, Praneetha and Vinod. Without all of them, all these years would not have been the same, including the time we spent at university.

I would especially like to thank Dr. P. G. Sabu, my U.G. H.O.D., who has guided and motivated me to pursue research as a career.

I will be eternally grateful to my parents, Zubair and Rasiya, for providing me with the opportunities and experiences that have shaped who I am. Despite the fact that you had little understanding of what I was researching, you were supporting any decision I made. I owe thanks to my wife, Hiba, for her patience and support during my Ph.D. studies. I highly value her support and appreciate her faith in me. Also, many thanks to my sister Ramsi for her love and care, which helped me finish my thesis. I also thank my father-in-law, Mohamed Salih and mother-in-law, Narjis, for their love and support.

Last but not least, I thank Allah for all of his blessings in my life, and I am grateful for all of the mercy and kindness he has shown me over the years, as well as for guiding me to the righteous path.

## Preface

Liquid crystals (LC) are orientationally ordered anisotropic fluids, composed of shape anisotropic organic molecules. They exhibit properties of both isotropic liquids as well as the crystalline solids. The nematic (N) phase, the most common of the LC phases, where the molecules are aligned parallel to a common direction termed as "director". In the smectic phase, the molecules have positional as well as orientational order with their long axes oriented normal to the plane of the layer. In chiral nematic liquid crystals, the molecules rotate along an axis. Topological defects in LCs are singularities where the director cannot be defined and the order parameter goes to zero. They can also be produced by introducing foreign particles into the liquid crystals. There have been many studies on liquid crystal colloids, in which micro and nano particles are dispersed in LCs. Such particles with appropriate surface treatment dispersed in nematic LCs cause deformation of the director, and induce defects and interact through long-range anisotropic elastic forces. It can be either dipolar, quadrupolar, boojum or vortex-like defects in the nematic phase. The elasticity of distortions determines the interactions between the dispersed particles.

The ability of liquid crystals to spontaneously arrange foreign particles into regular geometric patterns is interesting and important for developing advanced optical materials such as photonic crystals, sensors and tunable materials. The interaction, assembly and transport of colloidal particles can be controlled via particle geometry, surface anchoring and alignment of LC molecules, temperature, as well as the external fields. So far, most of the studies on the defects, assembly and transport in liquid crystal are concentrated on spherical particles. Studies on anisotropic particles like rods, platelets, stars, bullet-shaped particles etc. are meagre. These particles create distinct elastic distortions and sometimes new types of defects and interact through anisotropic elastic forces. In this thesis, we study the interaction, assembly and transport of silical micro and nano-rods in nematic as well as chiral nematic liquid crystals. Our research also focuses on the transformation of topological defects associated with spherical particles across LC phase transitions. Our study reveals some unusual aspects of the anisotropic particles in liquid crystals.

In this thesis, we study various aspects of nano and micro silica rods in nematic LCs. We investigate the defects, interaction and the directed assembly of micro and nano-rods in nematic and chiral nematic liquid crystals. Our study includes electric field driven transport properties of micro and nano-rods. Finally, we study the transformation of topological defects across the N-SmA-SmC phase transitions. This thesis is organized into total 6 chapters, which are described as follows.

The first chapter of the thesis gives a brief explanation about liquid crystal materials and different phases that have been used in the experiment. Physical properties of liquid crystal material such as birefringence, dielectric anisotropy etc. are also included in the discussion. Then, colloids in liquid crystal and topological defect structures associated with dispersed colloids are discussed briefly.

The **second chapter** presents the experimental techniques used for studying the particle induced defect and interaction in nematic liquid crystals. It includes sample preparation, polarizing optical microscopy and particle tracking. A brief discussion of the optical tweezers set-up and the theory of optical trapping is also included.

In the **third chapter**, we focus on the spontaneous orientation, elastic interaction and directed assembly of nano-rods (length: 3  $\mu$ m and diameter: 200 nm ) co-assembled with micro-rods (length: 6.5  $\mu$ m and diameter: 750 nm ) and the microspheres in nematic LCs. We show that, with homeotropic boundary condition, the silica nano-rods are oriented either orthogonal or parallel to the nematic director. The percentage of perpendicular nano-rods are significantly larger than the parallel nano-rods. Perpendicular nano-rods create very weak elastic deformation and exhibit unusual, out-of-plane, attractive interaction. On the other hand, the nano-rods oriented parallel to the director create strong elastic deformation and show anisotropic, in-plane, dipolar interaction.

Using dynamic laser tweezers, we design various colloidal analogues of linear polymer chains, ribbons and two dimensional binary colloidal crystals. The spontaneous out-of-plane interaction is very useful for vertical assembly of silica nano-rods in nematic liquid crystal. Such studies have important bearing on the efforts in making three-dimensional, periodic nematic colloidal systems, in which the orientational direction

of the nano-rods is orthogonal to the nematic director.

In the **fourth chapter**, we report experimental studies on the interactions of silica micro-rods dispersed in chiral nematic liquid crystals (NLC). Chiral NLCs are prepared by doping a chiral agent; 4-cyano-40-(2-methylbutyl)-biphenylene (CB15) in pure nematic 5CB. The pitch was adjusted in a cell of gap d such that the nematic structure is twisted by multiples of half-pitch i.e., d = N(p/2), which is denoted here as  $N\pi$ -twisted cell. We study the pair interaction of micro-rods orientated perpendicular to the rubbing direction in a  $2\pi$ -twisted cell and discover the existence of a colloidal bound state.

In the bound state, two micro-rods are self-trapped due to the competing effect of elastic attraction and electrostatic Coulomb repulsion. We show that, the bound state is highly stable and robust against the influence of external electrical and mechanical perturbations applied by an ac electric field and the elastic distortion created by the laser tweezers. With the help of the laser tweezers, we have created an assembly of several micro-rods in the form of a linear chain. Here, the micro-rods are connected through successive bound states and it is highly stable against thermal fluctuations.

In the bound state, we study the auto and cross-correlation functions of the particle's position. The autocorrelation function decays exponentially as expected whereas a strong time delayed-anticorrelation is observed with a pronounced minimum. It means the hydrodynamic interaction is asymmetric as one micro rod moves it tends to drag the other and the correlated fluctuations relax faster than the anticorrelated fluctuations. It is also observed that the depth of the minima in  $2\pi$  cell is higher than that of  $\pi$  cell. In  $2\pi$  cell the particles are closer than  $\pi$  cell. Hence, the result is consistent with the prediction that the strength of the hydrodynamic coupling is inversely proportional to the separation. We also study the auto and cross correlations of the orientational fluctuations. The autocorrelation function decays exponentially and it can be fitted to  $\langle \theta_1(t)\theta_1(0)\rangle \sim e^{-t/\tau_o}$  with a decay constant  $\tau_0$ . The value of decay constant is comparable to the effective director relaxation time of 5CB liquid crystal. The cross correlation function is almost zero, implies that the orientational fluctuations are not coupled hydrodynamically. Our experiments present a direct mea-

surement of the hydrodynamic interaction of anisotropic microparticles revealing an unexplored aspect of liquid crystal dispersion. Apart from the interplay of elastic and electrostatic interactions, hydrodynamic interaction in concentrated solutions might play an important role in designing new colloidal structures with tunable properties.

In the **fifth chapter**, we study the transport properties of silica nano and microrods in a NLC. In a planar aligned LC cell with negative dielectric anisotropy, the electric field doesn't realign the director, however the colloidal rods propels along to the director transducing the energy of the field. The motion of the particle is due to the breaking of quadrupolar symmetry of the surrounding electro osmosis flow. The propelling velocity is nonlinear and the velocity dependence can be described as,  $v = \mu_1 (E-E_0) + \mu_3 (E-E_0)^3$ , where  $E_0$  is the threshold field required to move the particles and  $\mu_1$  and  $\mu_3$  are the linear and 3rd order mobilities, respectively.

We show that, with increasing field, not only does the particle's velocity increase, but it also tilts along the field direction. At a fixed field and frequency, we compare the velocity of a micro and a nano-rod and found that, the nano-rods propel with larger speed as compared to the micro-rods. Our experiment shows that the applied electric field has two contributions. Firstly, it creates non-linear electrophoresis and secondly, it provides an electric torque; consequently the micro-rod tilts along the field direction. We further studied the optical control on colloidal rods in nematic liquid crystal doped with azo-dendrimer. It is observed that, these rods change the direction of motion in a NLC where UV light is irradiated.

In the **sixth chapter**, we study a pair of particles connected through elastic forces across N-SmA-SmC phase transitions. When the temperature is decreased from the nematic to SmA phase the hyperbolic hedgehog defects are transformed into smectic focal line defects. In the SmC phase, the layer distortion around the colloidal pair becomes nonuniform .

We measure the inter-particle separation (D) with varying temperature. In the nematic phase, D increases linearly followed by almost a discontinuous change at the N-SmA phase transition. Below the N-SmA transition, D increases continuously with decreasing temperature. The pre-transitional behavior of D is due to the increase in

the ratio of the bend to splay elastic constant. The temperature dependence of D -  $D_0$ , just below the N-SmA transition shows a power-law behavior,  $D - D_0 \sim t^{\alpha}$ , with an exponent  $\alpha = 0.36$ , where  $t = (1 - T/T_{NA})$ , and  $D_0$  is the separation at the transition temperature. At the SmA-SmC transition point, D changes slope and increases continuously as the temperature is decreased. Below the SmA-SmC phase transition, D shows a power-law behavior  $D \sim (1 - \frac{T}{T_{AC}})^{\beta}$ , with an exponent  $\beta \approx 0.53$ . According to de Gennes, the SmA-SmC phase transition belong to the 3D XY universality class, whereas many experiments showed a classic mean-field behavior with the tilt angle  $\theta$  is an order parameter, which is given by  $\theta = \theta_0 \mid \tau \mid^{\eta}$ , where  $\eta = 0.5$ . We measured the temperature dependence of tilt angle of our sample from x-ray diffraction studies. The exponent obtained from the fitting is  $\eta = 0.48$ , which is close to the exponent  $\beta = 0.53$  of the temperature dependence of separation. Our experiment suggests that the interparticle separation D, is coupled to the order parameter  $\theta$  of the SmA-SmC phase transition.

When colloidal particles with planar anchoring are introduced in a planar cell, each particle creates a pair of antipodal surface defects, called boojums. We choose a pair of such particles and study the transformation of the defect across the N-SmA-SmC phase transitions. In the SmA phase, the boojums are transformed into two line defects which are extended on the opposite sides of the pair along the rubbing direction up to several micrometers. In the SmC phase, the non-uniformly coloured regions around the colloids indicate that the layers are distorted randomly. For boojum colloids, the interparticle separation D decreases very sharply followed by a slope change at the N-SmA phase transition. But there is no observable change in D across the SmA-SmC transition. The line joining the center-to-center of the colloids makes an angle  $\phi$  with respect to the far field director, and  $\phi$  decreases continuously with a characteristic slope change at the SmA-SmC phase transition temperature. This suggests that the interparticle separation of a pair of colloids, as well as their orientation angle are coupled to the order parameters of the phase transitions.

# **Contents**

	List	of Abbı	reviations and Symbols	xix
1	on	1		
	1.1	Liquid	l crystals	1
		1.1.1	Nematic phase (N)	2
		1.1.2	Cholesteric phase $(N^*)$	4
		1.1.3	Smectic phases	5
	1.2	Physic	cal properties	7
		1.2.1	Birefringence	7
		1.2.2	Dielectric anisotropy	8
		1.2.3	Freedericksz transition	8
	1.3	Alignr	nent of liquid crystals	10
		1.3.1	Homogeneous alignment	10
		1.3.2	Homeotropic alignment	10
	1.4	Defect	ts in nematic liquid crystals (NLCs)	11
	1.5	1.5 Colloidal interaction in NLCs		14
		1.5.1	Dipolar nematic colloids	16
		1.5.2	Quadrupolar nematic colloids	19
		1.5.3	Boojum colloids	21
		1.5.4	Anisotropic colloids in nematic liquid crystals	22
		1.5.5	Chiral nematic colloids	23
	1.6	Hydro	odynamic interaction	25
2	Ехр	erimer	ntal Setup	34
	2.1	Introd	luction	34
	2.2	Prepar	ration of liquid crystal cells	34
		2.2.1	Thickness measurement of LC cell	35

	2.3	Liquid crystals and colloidal particles	38
		2.3.1 Colloidal particles used in the experiments	38
	2.4	Lambda-plate imaging for determining director orientation	41
	2.5	Optical tweezers	45
		2.5.1 Trapping of particles in isotropic media using optical tweezers .	47
		2.5.2 Optical trapping and manipulation of microspheres in LCs	49
		2.5.3 Trapping in planar cell	50
		2.5.4 Video analysis and particle tracking	53
3	Coll	oidal analogues of polymer chains, ribbons and 2D crystals em-	
	ploy	ring orientations and interactions of silica nano-rods dispersed in	
	a ne	ematic liquid crystal	57
	3.1	Introduction	57
	3.2	Experimental	58
	3.3	Results and discussion	59
	3.4	Conclusion	71
4	Inte	ractions of silica micro-rods in chiral nematic liquid crystals	76
	4.1	Introduction	76
	4.2	Experimental	77
	4.3	Results and discussion	78
	4.4	Conclusion	95
5	Elec	ctrophoretic mobility of silica micro and nano-rods in nematic liq-	
	uid	crystals	99
	5.1	Introduction	99
	5.2	Experimental	101
	5.3	Results and discussion	101
		5.3.1 Optical control on the particle motility	107
	5.4	Conclusion	112
6	N-S	mA-SmC phase transitions probed by a pair of elastically bound	
	coll	oids	116
	6.1	Introduction	116

6.3	Experimental	
6.4 Publica	Conclusion         128           tions         132	

# List of Abbreviations and Symbols

N : Nematic phase

NLC : Nematic liquid crystal

N\* : Cholesteric phase
 SmA : Smectic-A phase
 SmC : Smectic-C phase

ITO : Indium-tin-oxide

AOD : Acousto-optic deflector  $\hat{n}$  : Liquid crystal director

S: Scalar order parameter

 $K_{11}, K_{22}, K_{33}$ : Splay, twist and bend elastic constants

 $n_o$  : Ordinary refractive index

 $n_e$  : Extra-ordinary refractive index

 $\triangle n$  : Birefringence

 $E_{th}$  : Freedericksz threshold field  $\xi$  : de Gennes-Kleman length

K: Elastic constant

W: Surface anchoring coefficient

 $\lambda$  : Wavelength  $\theta$  : Tilt angle

 $k_B$  : Boltzmann constant

 $T_{NA}$ : N-SmA phase transition temperature

 $T_{AC}$  : SmA-SmC phase transition temperature

D : Diffusion coefficient

 $\varsigma$  : Drag coefficient

p : Pitch

au : Relaxation time

 $k_x$ : Stiffness constant along the rubbing direction

 $k_y$ : Stiffness constant perpendicular to the rubbing direction

 $\eta$  : Viscosity

 $\lambda_D$  : Debye screening length

1

# Introduction

# 1.1 Liquid crystals

Liquid crystals (LCs) are materials those show an intermediate state known as mesophase between the isotropic liquids and regular solids. They change shape like a fluid but at the same time exhibit anisotropy in their optical, electrical and magnetic properties. Figure 1.1 shows a schematic representation of crystal, liquid crystal and isotropic phases, with the molecule in the shape of a rod. LCs are majorly categorized into two namely, thermotropic and lyotropic. Thermotropic liquid crystals exhibit mesophases in temperature range whereas lyotropic liquid crystals exhibit mesophase in certain temperature as well as concentration range. Depending on the

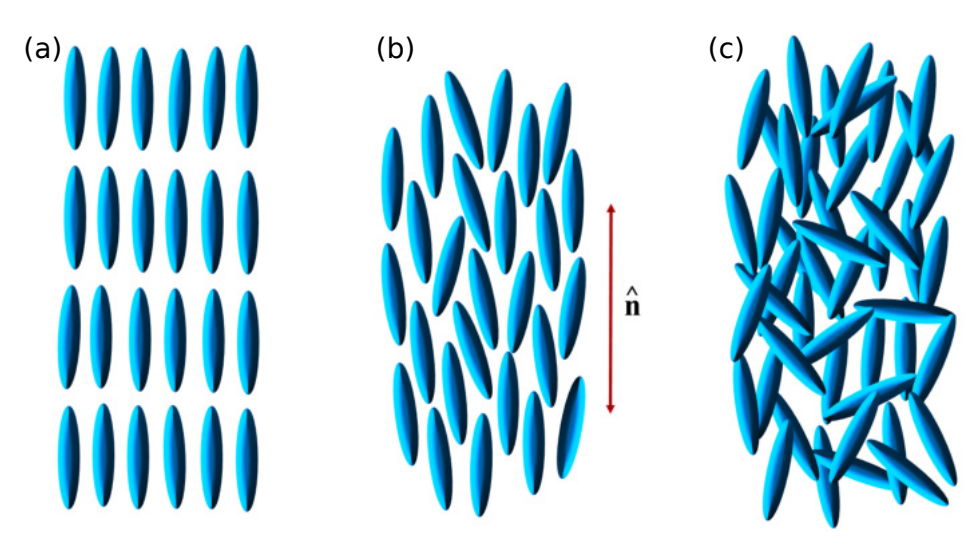


Figure 1.1: Schematic diagram showing (a) crystal, (b) liquid crystal, and (c) isotropic liquid-phase.

shape of the molecules, thermotropic liquid crystals are again sub categorized into

#### 1.1. Liquid crystals

calamitic (rod-shaped), discotic (disc-like) and bent core (bent-shaped) LCs. Thermotropic calamitic LCs are classified into nematic, smectic and cholesteric phases based on molecular ordering. Some of the phases which are relevant to the present thesis are discussed here.

#### 1.1.1 Nematic phase (N)

Nematic (N) phase is one of the most common and least ordered phase among all the known liquid crystal phases. We see thread like structures when we observe nematic liquid crystal (NLC) under a polarizing optical microscope. In a nematic phase, the molecules have no positional order, but they self-align to have long-range orientational order. Therefore, the nematic phase can be considered to be an anisotropic liquid. The direction of average molecular orientation is called the director which is represented by a unit vector  $\hat{n}$ . Nematic is usually apolar in nature, i.e.,  $\hat{n}$  and  $-\hat{n}$  are physically equivalent. But very recently a polar nematic, called splay nematic exhibiting antiferroelectric ground state has been discovered in a highly polar compounds [1]. Most of the nematic liquid crystals are uniaxial, which means they have one principal axis and other two orthogonal axis are equivalent. A schematic representation of the nematic liquid crystal is shown in Fig. 1.2.

The degree of orientational ordering of the calamitic molecules in the nematic phase is determined by the nematic order parameter S. To define the local orientation at a point r=(x,y,z), let us consider that nematic LC molecule is a rigid rod with a unit vector a along the long axis. Average of this unit vector becomes zero because nematic is apolar in nature. Since it is not possible to introduce a vector order parameter for liquid crystal, we introduce a second rank tensor  $S_{\alpha\beta}$  [2], which is defined by

$$S_{\alpha\beta} = \langle a_{\alpha}a_{\beta} \rangle - \frac{1}{3}\delta_{\alpha\beta}, \qquad \alpha, \beta = x, y, z$$
 (1.1)

General form of order parameter, for a uniaxial nematics is given by

$$S_{\alpha\beta}(\vec{r}) = S(n_{\alpha}(\vec{r})n_{\beta}(\vec{r})) - \frac{1}{3}\delta_{\alpha\beta}$$
 (1.2)

where S is the measure of degree of alignment of the long axes of the molecules along  $n(\vec{r})$ . The expression in the parenthesis describes the spatial variation of  $n(\vec{r})$ . The

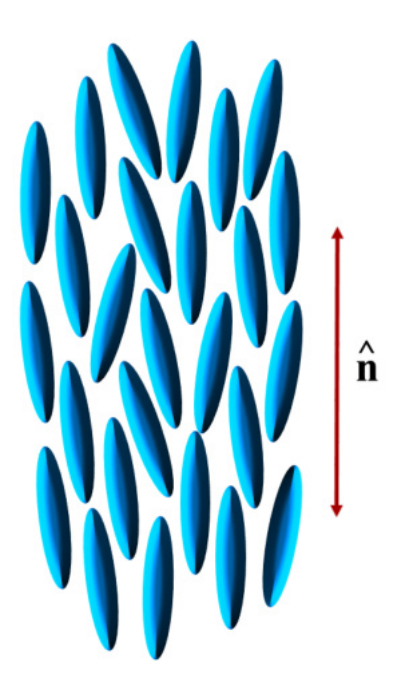


Figure 1.2: Schematic representation of LC molecules in the nematic phase,  $\hat{n}$  signifies the director.

scalar order parameter for cylindrically symmetric molecules is defined in the form of a second order Legendre polynomial

$$S = \frac{1}{2} < 3\cos^2\theta - 1 > \tag{1.3}$$

where  $\theta$  is the angle made by the long axis of the molecules with the local director. The angular brackets denote the time-average of the angles  $\theta$  over the ensemble of molecules. S=0 for an isotropic system, whereas S=1 for a perfectly aligned system. Generally, for a nematic liquid crystal the value of S varies from 0.3 to 0.8 with temperature.

For a uniformly aligned nematic LC, the director field  $\hat{n}$  is uniform and gives the lowest free energy. The distortion in the director field give rise to elastic energy. This is analogous to conventional solids with positional ordering. By considering only the elastic deformation of the NLC, the elastic free energy (Frank-Oseen) density can be written as [3,4]

$$f = \frac{1}{2} [K_{11}(\vec{\nabla} \cdot \vec{n})^2 + K_{22}(\vec{n} \cdot \vec{\nabla} \times \vec{n})^2 + K_{33}(\vec{n} \times \vec{\nabla} \times \vec{n})^2]$$
 (1.4)

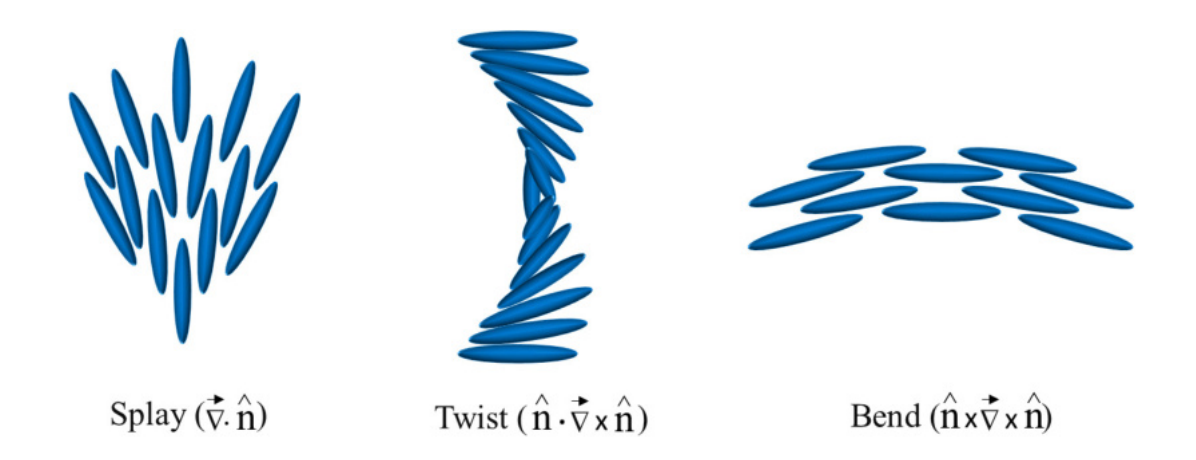


Figure 1.3: Schematic diagram of different elastic deformations.

The three terms in this expression corresponds to a specific elastic deformation with a specific elastic constant.  $K_{11}$  is the splay elastic constant,  $K_{22}$  is the twist elastic constant and  $K_{33}$  is the bend elastic constant. All three elastic deformations are schematically represented in Fig. 1.3. Usually in rod-like molecules,  $K_{33} > K_{11} > K_{22}$  and these are positive with an order of  $10^{-12}$  N.

### 1.1.2 Cholesteric phase $(N^*)$

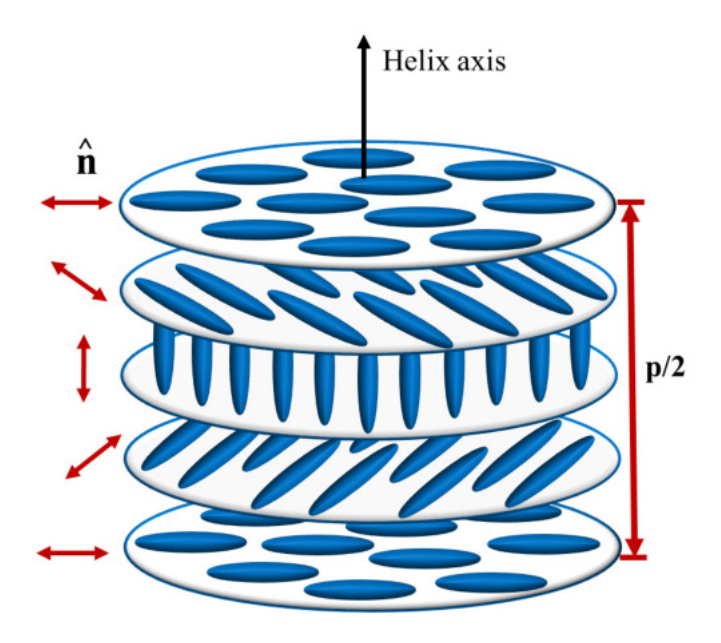


Figure 1.4: Schematic representation of the cholesteric phase, where p is the pitch.

#### 1.1. Liquid crystals

Cholesteric liquid crystals are also known as chiral nematic liquid crystals, where molecules are chiral or chiral dopants are added in the NLC. In chiral NLCs, the director rotates spontaneously along a direction and creates helical structure (see Fig. 1.4). The distance covered by a full rotation of the director  $\hat{n}$  is known as pitch, p and the repetition period is half pitch, p/2. The directors  $n(\vec{r})$ , and  $-n(\vec{r})$  are considered to be equal by looking at the mirror symmetry of a plane normal to the pitch axis.

#### 1.1.3 Smectic phases

In the smectic phase, the liquid crystal molecules maintain the general order of the nematic phase but are also aligned in layers. The simplest and most common layered structure is known as smectic-A (SmA) phase, in which the molecules order into layers, with the layer normal parallel to the director. This is the least ordered smectic phase. Also layer thickness is about equal to the molecular length. A schematic representation of the molecular arrangement of rod like molecules in the SmA phase is shown in Fig. 1.5. The density variation along the layer normal assumed to be along the  $\hat{z}$  direction can be written as,

$$\rho(z) \simeq \rho_0 + \psi e^{iq_A \cdot z} \tag{1.5}$$

where  $\rho_0$  is the average density and  $\hat{z}$  is the unit vector along Z-axis. This defines a complex order parameter known as smectic density wave

$$\psi(x) = \mid \psi \mid e^{iq_A z + \phi} \tag{1.6}$$

where  $|\psi|$  is the complex amplitude of the density wave,  $q_A = 2\pi \hat{z}/d$ , where d is the layer thickness and  $\phi$  is an arbitrary phase. In the nematic phase,  $\psi = 0$ , and in SmA phase,  $\psi$  is non-zero.

Smectic-C (SmC) phase is similar to the SmA phase. Here the molecules again form a layer structure but the director makes an angle  $\theta$  to the layer normal. The tilt angle  $\theta$  (polar) reduces the layer thickness. Projection of director vector in the x-y plane makes an azimuthal angle  $\phi$  with respect to the positive x-axis, though it does not affect the layer thickness. A schematic representation of the molecular arrangement of rod-like molecules in the SmC phase is shown in Fig. 1.6. Some smectic phases present a special type of order in the layers plane characterized by short-range positional order

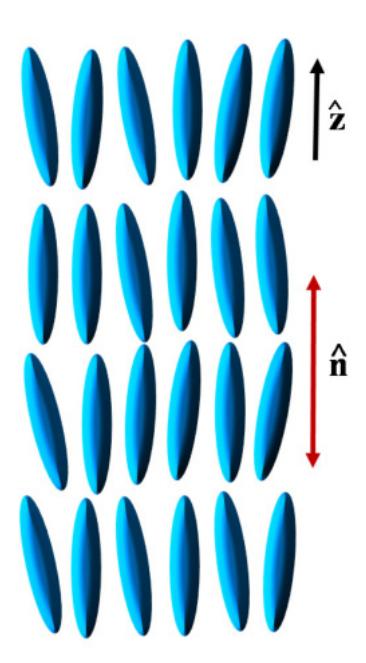


Figure 1.5: Schematic of the SmA phase. The director  $\hat{n}$  is oriented parallel to the layer normal  $\hat{z}$ .

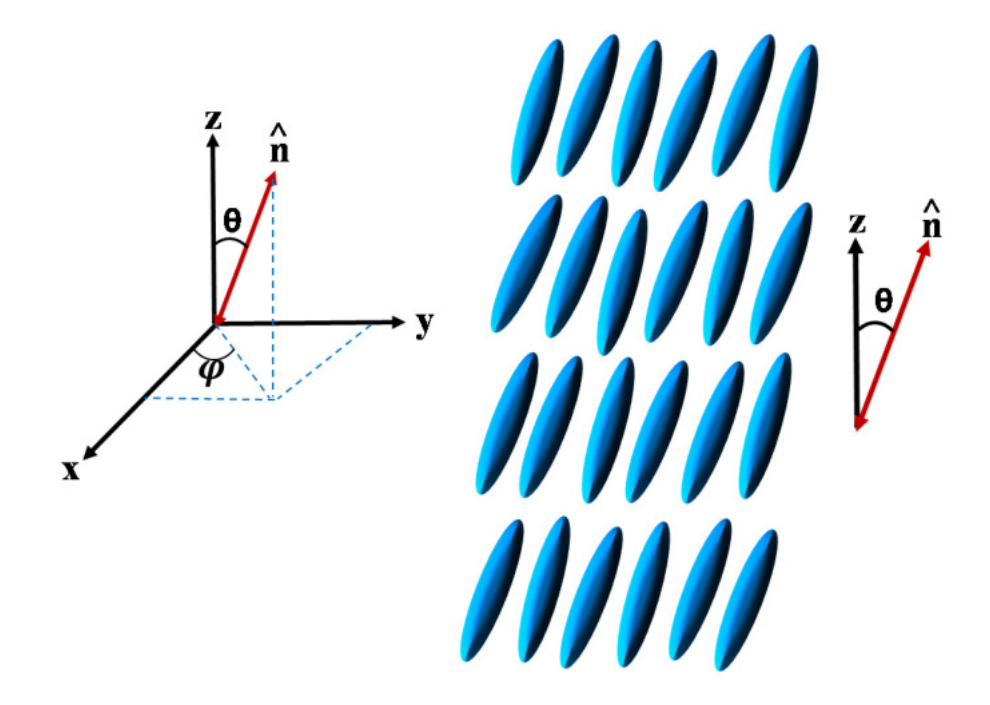


Figure 1.6: Schematic of a SmC phase. The director  $\hat{n}$  makes an angle  $\theta$  with the layer normal  $\hat{z}$ .

#### 1.2. Physical properties

(in a hexagonal lattice) and long-range orientational order of the axis of the local lattice bonds. In the SmI phase, LC molecules are tilted toward the hexagons vertex. SmI and SmG are more ordered phase than SmC phase.

Any smectic layer deformation can increase the free energy. Small deformations of these layers can be described by the displacement field u. Director field  $\hat{n}$  is normal to the layers at each point and given by [5],

$$\hat{n} = (n_x, n_y, 1) = \left(-\frac{\partial u}{\partial x}, -\frac{\partial u}{\partial y}, 0\right)$$
(1.7)

The Frank-Oseen elastic energy (f) for the SmA LC is given by [6],

$$f = \frac{B}{2} \left( \frac{\partial u}{\partial z} \right)^2 + \frac{K_{11}}{2} \left( \frac{\partial^2 u}{\partial x^2} + \frac{\partial^2 u}{\partial y^2} \right)^2 \tag{1.8}$$

where B is called the layer compression elastic modulus which measures the energy cost associated with compressing or stretching of the smectic layers. The typical value of layer compression elastic modulus in smectic liquid crystal is  $B \simeq 0.4\text{-}1.4 \times 10^8$  dyn/cm<sup>2</sup>.

# 1.2 Physical properties

#### 1.2.1 Birefringence

When light enters in a liquid crystal sample, it is being broken up into two components, which travels with two different velocities. Faster one is called ordinary ray and slower one is called extra ordinary ray. Refractive indices corresponding to ordinary and extra ordinary rays are  $n_o$  and  $n_e$ , respectively and given by

$$c_o = c_o/n_o \tag{1.9}$$

and

$$c_e = c_o/n_e \tag{1.10}$$

where  $c_o$  and  $c_e$  corresponds to the velocity of the ordinary and extraordinary rays, respectively. Due to different velocities, the waves get out of phase as they propagate.

#### 1.2. Physical properties

The waves are recombined when they come out from the material with different polarization. Refractive indices corresponding to ordinary and extra ordinary rays are  $n_o$  and  $n_e$  respectively. For a nematic LC,  $n_e=n_{\parallel}$  and  $n_o=n_{\perp}$ . The difference in the refractive indices of the extraordinary and the ordinary waves is called the birefringence of the material and is written as,

$$\Delta n = n_e - n_o = n_{\parallel} - n_{\perp} \tag{1.11}$$

 $\triangle n$  is positive for calamitic liquid crystals and typically varies from 0.01 to 0.2 [7]. Orientational order can be calculated by using the relation  $S \approx \triangle n/\triangle n_0$ , where  $\triangle n_0$  is the birefringence in a completely aligned system when S=1.

#### 1.2.2 Dielectric anisotropy

Generally, dielectric constant  $\epsilon$  is a measure of the response of the material towards an external electric field. In uniaxial nematics, the dielectric constant  $\epsilon_{\parallel}$  and  $\epsilon_{\perp}$  are measured with electric field parallel and perpendicular to the director  $(\hat{n})$ . The dielectric constant is influenced by the structure of the molecule, permanent dipole moments and order parameter. The dielectric anisotropy is given by [8],

$$\Delta \epsilon = \epsilon_{\parallel} - \epsilon_{\perp} \tag{1.12}$$

The dielectric constants and the anisotropy are temperature dependent. Usually the magnitude of anisotropy increases with decreasing temperature and it is proportional to S. The dielectric anisotropy could be positive or negative.

#### 1.2.3 Freedericksz transition

Liquid crystals are usually influenced by the external electric and magnetic responses. Depending on the sign of the dielectric anisotropy  $\Delta \epsilon$ , the director can be oriented parallel or perpendicular to the field direction. If an electric field is applied orthogonal to a homogeneously aligned nematic liquid crystal, the director will tend to reorient along the field direction if the dielectric anisotropy is positive ( $\Delta \epsilon > 0$ ). Similar reorientation of liquid crystal molecules is observed in homeotropic nematic cell when

 $(\triangle \epsilon < 0)$ . Such reorientation of the director by external fields is known as electric Freedericksz transition [9]. The dielectric displacement  $\vec{D}$  in a NLC is given by [10]

$$\vec{D} = \epsilon_o \epsilon_\perp \vec{E} + \epsilon_o \Delta \epsilon (\hat{n} \cdot \vec{E}) \hat{n} \tag{1.13}$$

The dielectric energy density is written as

$$W_{diel} = -\int_0^E \vec{D} \cdot d\vec{E} = -\frac{1}{2} \epsilon_o \epsilon_\perp \vec{E}^2 - \frac{1}{2} \epsilon_o \Delta \epsilon (\hat{n} \cdot \vec{E}^2)$$
 (1.14)

The threshold field required for the reorientation is given by

$$E_{th} = \frac{\pi}{d} \sqrt{\frac{K_{11}}{\epsilon_o \Delta \epsilon}} \tag{1.15}$$

A schematic representations of molecular reorientation under the effect of applied field is shown in Fig 1.7.

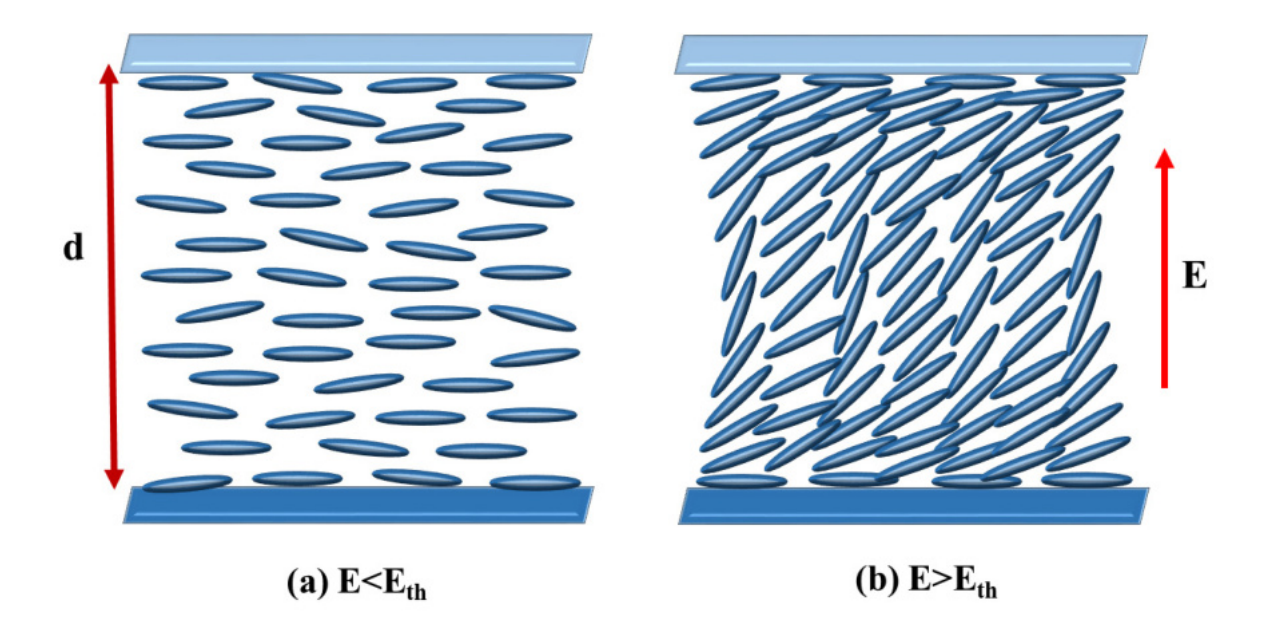


Figure 1.7: Schematics of the director orientation (a) below and (b) above the threshold field.

# 1.3 Alignment of liquid crystals

Uniform alignment of LC molecules enables us to measure different physical properties such as birefringence, dielectric anisotropy etc. This is also very important for the display application. Generally, there are two types of alignments are preferred for physical measurements namely, planar or homogeneous and homeotropic. Desired alignment of the LC molecules can be achieved by coating appropriate polyimide on the substrate.

#### 1.3.1 Homogeneous alignment

Homogeneous or planar alignment of LC can be achieved by coating the surface of the glass plates with appropriate polyimide (AL-1254) and rubbing. A schematic representation of homogeneous alignment is shown in Fig. 1.8(a). The photograph of a rubbing machine (HOLMARC) is shown in Fig. 1.8(c).

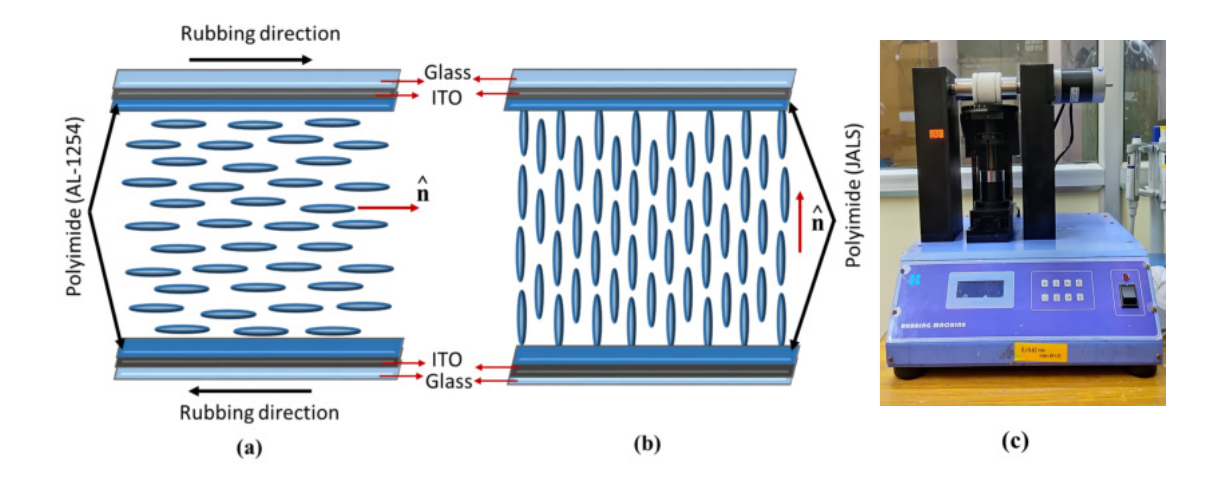


Figure 1.8: Schematic diagrams of the (a) homogeneous and (b) homeotropic alignments of the liquid crystal molecules. (c) The rubbing machine in the laboratory.

#### 1.3.2 Homeotropic alignment

Homeotropic alignment of LC can be achieved by coating the glass surface with suitable polyimide (JALS-204). A schematic representation of homeotropic alignment is shown

in Fig 1.8(b).

# 1.4 Defects in nematic liquid crystals (NLCs)

Topological defects are singularities that occurs in the mediums with long-range order, like, superfluid helium, crystalline solids and liquid crystals etc [6,11,12]. These are discontinuity or singularity in mathematical language and occurs as a consequence of broken continuous symmetry [13]. The defect has a core region, where the order parameter goes to zero, and a far field region characterized by non vanishing strain.

LCs are ideal materials for studying and manipulating topological defects. Different liquid crystal phases like nematic, cholesteric, smectic-A and smectic-C, have different types of defects. In a nematic liquid crystal, topological defects can be classified into (1) line defects (disclinations) and (2) point defects (hedgehogs and boojums) [3] and can be well understood by the homotopy theory. The core of the defect can be recognized as a singular point or line which can be identified under polarizing optical microscope as they scatters light because of reduced order at the core. A 'schlieren' texture can be seen when a planar nematic liquid crystal cell is observed under an optical microscope. The black brushes in the Fig. 1.9(a) come together in a point and these are generally two or fourfold. Position of the singular point does not change, but the brushes rotates on rotating the crossed polarizer. It shows orientation of the director changes around a defect. The four dark brushes, those shown in Fig. 1.9(b), represent the "radial" director distortion.

A major interest of studying topological defects in LC is that the defects are visually observable under optical polarizing microscope. Strength of the defect or also known as the winding number and it is denoted as 's' with an integer or semi-integer number, which shows number of times the director rotates by an angle  $2\pi$  when one encircles the defect core as shown in Fig. 1.9(b). Positive or negative value of the strength indicates the rotational direction of the nematic director. Few commonly observed defects with corresponding strength are shown schematically in Fig. 1.10.

The strength, s, of a disclination is the angle by which the director rotates along a

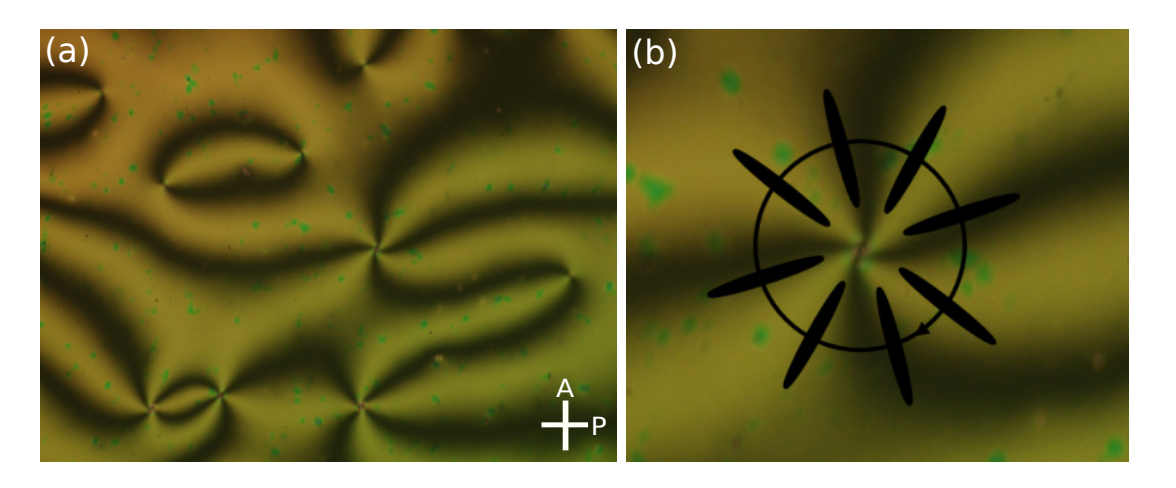


Figure 1.9: (a) Optical photomicrograph of planar schlieren textures of nematic liquid crystal cell. (b) Enlarged region around a defect.

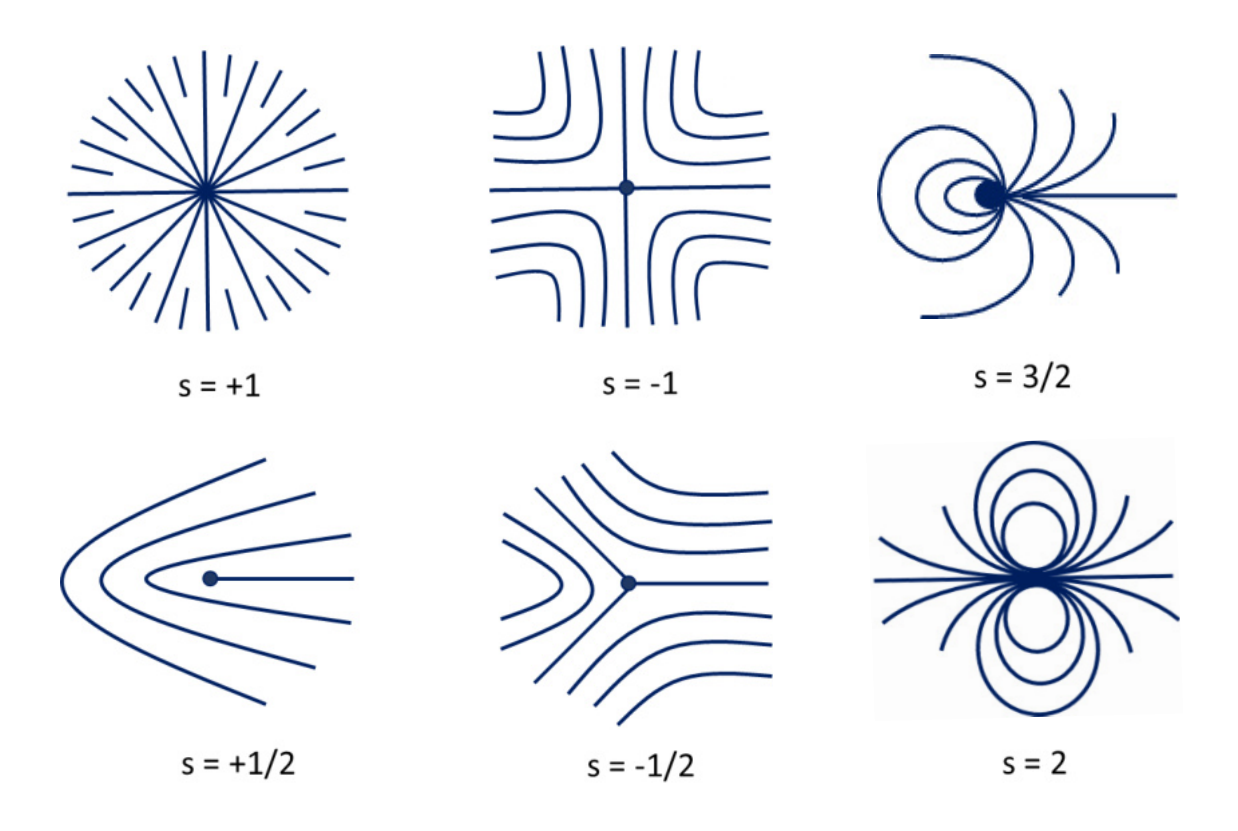


Figure 1.10: Schematic representation of 2D distortions found in nematic liquid crystal with various topological charge s.

closed loop enclosing the disclination by  $2\pi$  (see Fig. 1.9(b)),

$$\oint \frac{d\phi}{dl}dl = 2\pi s$$
(1.16)

where  $\phi$  defines the director orientation in a plane. In a general form, the elastic free energy density given by Eq. (1.4) can be written as

$$f = \frac{1}{2}K(\nabla\phi)^2 \tag{1.17}$$

The Euler-Lagrange minimisation condition corresponding to Eq. (1.17) is

$$\nabla^2 \phi = 0 \tag{1.18}$$

It has the solution of the form

$$\phi = s \times tan^{-1} \left(\frac{y}{x}\right) + D = s\alpha + \beta \tag{1.19}$$

In the nematics, s can be any multiple of  $\pm 1/2$  because of the symmetry of the medium.

Like nematics, there are defects called dislocations in the smectic LCs due to their layered structure. In the presence of dislocation, the change in the layer displacement field, u, integrated along a closed loop enclosing the dislocation line is

$$\oint du = (nd)\hat{z} = \vec{b} \tag{1.20}$$

where  $\vec{b}$  is called the Burgers vector of the dislocation and d is the layer spacing [14].

There are two types of dislocations in smectic A LC: the edge dislocations for which  $\vec{b}$  is perpendicular (Fig. 1.11(a)) and the screw dislocations for which  $\vec{b}$  is parallel to the dislocation line (Fig. 1.11(b)). A layered structure with fluid character within the smectic layers leads to the formation of a special type of texture accompanying focal conic domains (FCDs). These FCDs are generally observed in SmA LCs and Fig. 1.11(c) exhibits a schematic diagram of LC director configuration defect lines of FCD [15]. They are basically formed of concentric cylinders. Figure 1.11(d) shows polarizing optical photomicrographs of focal conic defects observed under crossed polarizer.

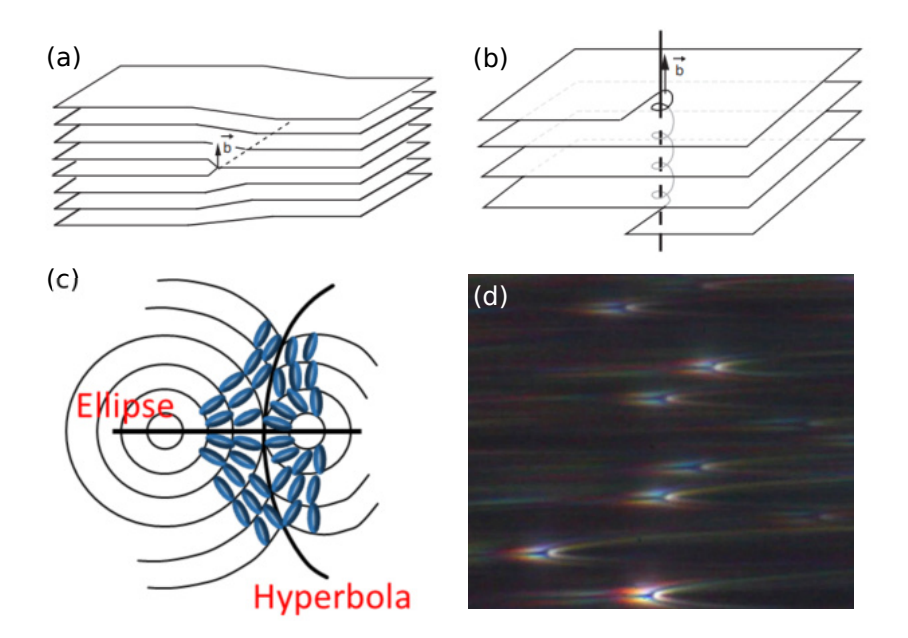


Figure 1.11: (a) Edge and (b) screw dislocations. (c) Smectic layers and LC director configuration of focal conic domains (FCD). (d) Polarizing optical micrograph (POM) of typical focal conic defects in the SmA phase.

# 1.5 Colloidal interaction in NLCs

Liquid crystal-colloids are defined as the dispersion of nano and micro meter sized particles in the host liquid crystal media [16–18]. In this thesis, we deal with mostly rod-shaped and also spherical colloids dispersed in either NLCs or chiral NLCs [19–22]. By "colloids" we mean the micrometer-sized particles. These particles are levitated in the bulk due to the director field that pushes the particles away from the bottom. When spherical colloids are dispersed in NLC, there is a distortion of director field around the colloid which gives an elastic energy that scales as KR, where K is the average elastic constant and R is the particle radius [23, 24]. The distortion around a particle depends on the surface anchoring of the LC molecules which cost a surface anchoring energy that scales as  $WR^2$ , where W is the surface anchoring coefficient. The ratio of the elastic constant and the anchoring strength has the dimension of length and is given by  $\xi = K/W$ , called as de Gennes-Kleman length. Elastic constant K can be estimated as  $K \sim k_B T/a \sim 10$  pN, where a is the typical molecular length which

is about 1 nm and T is the temperature. Considering the anchoring energy W ranges from  $10^{-6}$  J/m<sup>2</sup> to  $10^{-3}$  J/m<sup>2</sup>,  $\xi$  ranges from 10 nm to 10  $\mu$ m.

Liquid crystal colloids can be categorized into type-I and type-II on the basis of de Gennes-Kleman length. In type-I LC colloids, the size of the particles is much smaller ( $R << \xi$ ) and this usually occurs in the case of nanoparticles. Such particles do not create noticeable distortion in the nematic director field. But they significantly affect the anisotropic physical properties of the LCs like elastic, viscous, dielectric and optical anisotropy, etc. In type-II LC colloids,  $R >> \xi$ , and the microparticles create visible elastic distortion in the nematic director field which induces long range interaction among the particles. Such interactions lead to the formation of complex colloidal structures [25–28].

As we mentioned earlier, topological defects are the consequence of broken continuous symmetry [13]. The breaking of the symmetry in the near-field region, which is obtained either by the anchoring strength or by the shape of the particle, leads to the different solutions in the far-field nematic region. At far distances from the particle, the director field tends to be uniform  $n_0=(0,0,1)$  and is written as  $n=(n_x,n_y,1)$ . In the one-constant approximation, the Frank free energy is given by [29],

$$f = \frac{K}{2} \int d^3r [(\nabla n_x)^2 + (\nabla n_y)^2]$$
 (1.21)

The equilibrium equations are the Laplace equations for the transverse components  $n_{\mu}$  ( $\mu=x,y$ ),

$$\nabla n_{\mu} = 0 \tag{1.22}$$

At large distances r, it can be expanded in multipoles,

$$n_{\mu} = \frac{A\mu}{r} + \frac{P_{\mu}.r}{r^3} + \frac{c_{\mu}^{ij}r_ir_j}{r^5} + \dots$$
 (1.23)

The first term in Eq. (1.23) is connected with the "charge", the second with the dipole moment, and the last term is connected with the quadrupole moment.

Different types of topological defect structures such as elastic dipole, quadrupole,

hexapole, octupole etc are observed which are stabilised by the anchoring strength and cell confinement [3,11].

#### 1.5.1 Dipolar nematic colloids

When microspheres with homeotropic surface anchoring are dispersed in a planar nematic cell, they act as a source of topological defect with charge Q = +1. Because of the boundary conditions, the total topological charge of the nematic colloidal system is zero. Therefore, the particle induce another defect with charge Q = -1 in its vicinity [3,13]. One of the possible defects is a hyperbolic hedgehog along with the particle form a defect pair (Fig. 1.12(b) and 1.12(c)). The topological charge +1 of a radial hedgehog represented by the spherical particle and hyperbolic defect has -1 charge which makes the total charge zero. Another possibility is a disclination loop that encircles the spherical particle like a Saturn ring and form an elastic quadrupole defect [30, 31].

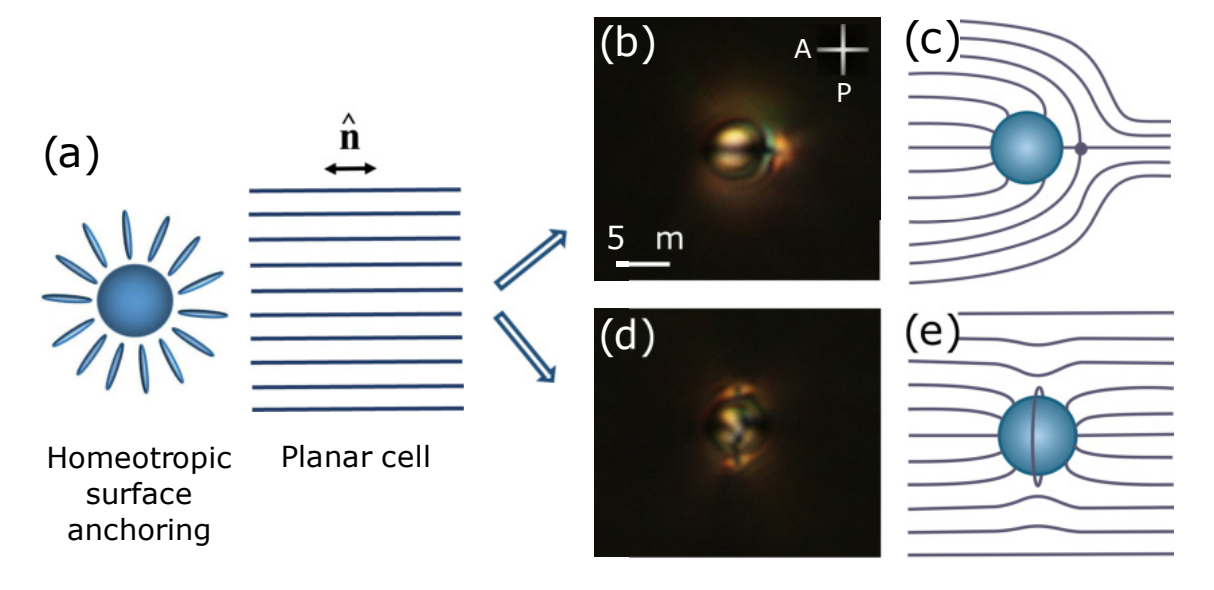


Figure 1.12: (a) Microsphere with homeotropic surface anchoring dispersed in a uniformly aligned planar cell of liquid crystal molecules. Optical photomicrographs of microspheres under crossed polarizers which forms (b) elastic dipolar defect and (d) elastic quadrupolar defect. The schematic representation of director field corresponding to the (c) elastic dipole and (e) quadrupole.

Schematic representation of homeotropic surface alignment on a micro-sphere and corresponding possible defect structures are shown in Fig. 1.12.

#### 1.5. Colloidal interaction in NLCs

When the two colloids are brought at a close separation, their region of elastic distortion overlaps and they start to interact to minimise the energy of deformation. Figure 1.13(a) shows some snapshots of two microspheres interacting in a nematic LC.

The time dependence of particle separation R(t) for a pair of microsphere shows the nature of the elastic interaction (Fig. 1.13(b)). In this case, inertial forces are negligible, and the elastic force  $F_{el}$  is balanced by a drag force given by,  $F_{drag} = -\zeta dR(t)/dt$ , where  $\zeta$  is a drag coefficient and dR(t)/dt is the particle velocity. Therefore the equation of motion is given by  $F_{el} + F_{drag} = 0$ . For particles with dipolar configuration, the corresponding force is given by  $F_{el} = -k/R^4$  where k is a constant. Therefore the equation of motion can be written as

$$-\frac{k}{R^4} = \zeta \frac{dR}{dt} \tag{1.24}$$

Integrating the equation of motion, we get

$$\int_0^t kdt = \int_R^{R_0} \zeta R^4 dR \tag{1.25}$$

Solving the integral, we get

$$kt = \zeta(\frac{R_0^5}{5} - \frac{R^5}{5}) \tag{1.26}$$

After rearranging we get

$$R(t)^5 = R_0^5 - 5\frac{k}{\zeta}t\tag{1.27}$$

Finally the time dependent particle separation can be written as

$$R(t) = (R_0^5 - 5\alpha t)^{1/5} (1.28)$$

where  $\alpha = k/\zeta$ ,  $\zeta$  being the viscous drag coefficient and  $R_0$  is the centre-to-centre

separation at t = 0 s [32]. Similarly for quadrupolar interaction,  $F_{el} = -k/R^6$  and the separation can be written as

$$R(t) = (R_0^7 - 7\alpha t)^{1/7} \tag{1.29}$$

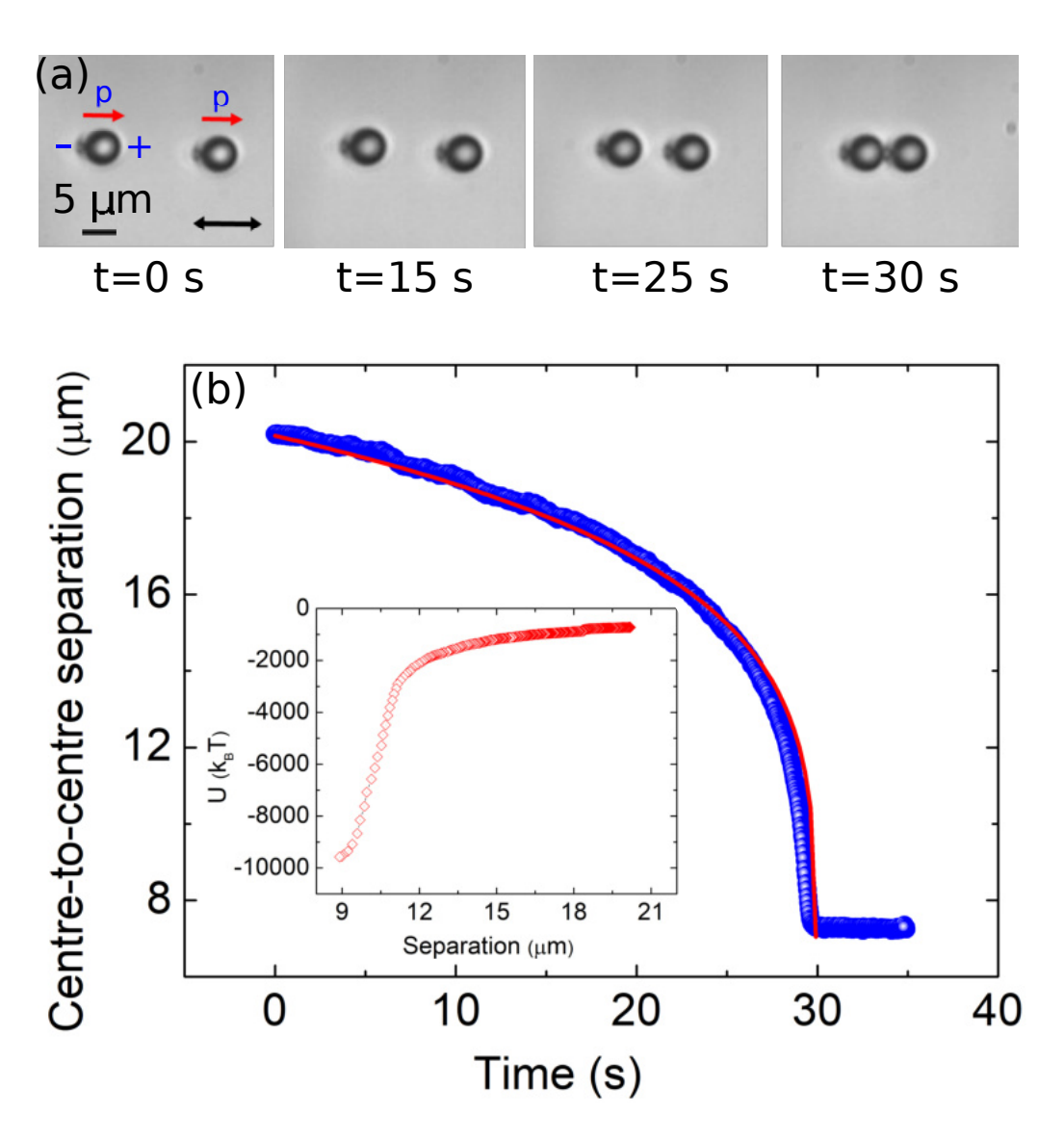


Figure 1.13: (a) Snapshots of interaction of a pair of dipolar microspheres in nematic phase, where the red arrows indicates direction of elastic dipole moment (p). (b) Time dependence of separation of two interacting microspheres. Red curve indicates the least square fit to the equation:  $R(t) = (R_0^5 - 5\alpha t)^{1/5}$  for dipolar type interaction. The inset shows the corresponding interaction potential, where the particles diameter is 5.2  $\mu$ m.

Figure 1.13(b) shows a typical time dependent separation of two dipolar particles and

corresponding fitting to the Eq. (1.28). The interaction potential can be estimated by using video microscopy technique. Here the acceleration of the particle is negligible, therefore  $F_{net} = 0$ , i.e. drag force is balanced by the structural force, which is given by,

$$F = 6\pi R (\eta_x \frac{\partial \vec{r}_x}{\partial t} + \eta_y \frac{\partial \vec{r}_y}{\partial t})$$
 (1.30)

where R is the radius of microsphere,  $\eta_x$  and  $\eta_y$  are the viscosity along and perpendicular to the director, respectively and  $\frac{\partial \vec{r}_i}{\partial t}$  is the corresponding velocity of the particle. Velocity is measured by tracking the particle trajectory using appropriate computer program. The corresponding potential energy can be calculated from  $U=\int F dr$ .

Using an electrostatic analogy, at the large distance, the behaviour of nematic mediated interactions has been studied theoretically. Using one-constant approximation, and considering  $n(r) = (n_x, n_y, 1 - O(n_x^2, n_y^2))$ , the elastic free energy is written as [33]

$$f \simeq \frac{K}{2} \int d^3r ((\nabla n_x)^2 + (\nabla n_y)^2 + O(n_x^4, n_y^4))$$
 (1.31)

The effective dipolar interaction potential is derived as [13],

$$U = C_1 \frac{K}{r^3} \left( 1 - 3\cos^3 \theta \right)$$
 (1.32)

where  $C_1$  is a proportionality constant that depends on the size of the microsphere, r is the particle separation and  $\theta$  is the angle between the far field director and the vector connecting the centres of the particles.

#### 1.5.2 Quadrupolar nematic colloids

As it has been shown in the earlier section, there are two common defects possible. Like dipolar defect, there can be a quadrupolar defect (Saturn ring defect) with a winding number of -1/2 around the colloid (Fig. 1.12(d) and 1.12(e)). Figure 1.14(a) presents few snapshots of a pair of quadrupolar interacting particles. Figure 1.14(b) shows the time dependent separation and corresponding fitting to  $R(t) = (R_0^7 - 7\alpha t)^{1/7}$ .

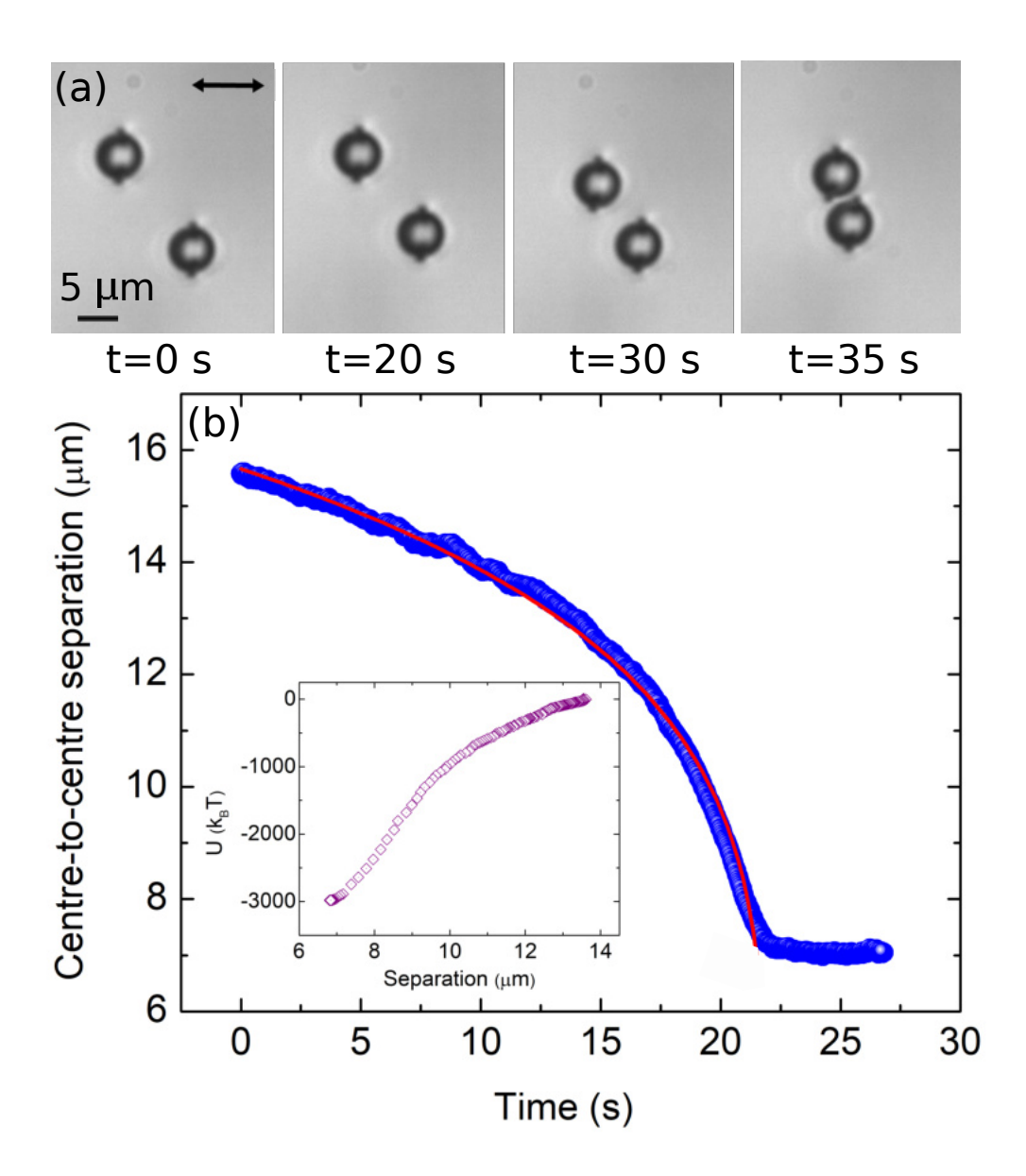


Figure 1.14: Snapshots of interaction of a pair of quadrupolar microspheres in the nematic phase (b) Time dependence of centre-to-centre separation of two microspheres. Solid red curve indicates the least square fit to the equation:  $R(t) = (R_0^7 - 7\alpha t)^{1/7}$  for quadrupolar type interaction. The inset shows the corresponding interaction potential, where the particles diameter is 5.2  $\mu$ m.

The interaction between a pair of microspheres with quadrupolar defect also mediated by defects. The strength of interaction between two quadrupoles is inversely proportional to the separation  $r^5$  between two colloids and is given by [13].

$$U = C_2 \frac{K}{r^5} \left( 9 - 90 \cos^2 \theta + 105 \cos^4 \theta \right)$$
 (1.33)

where  $C_2$  is a proportionality constant. We measured the interaction potential between two quadrupolar spheres as shown in the inset of Fig 1.14(b). The minimum of quadrupolar interaction energy is  $\simeq 3000 \text{ k}_B\text{T}$  and is found to be lower than dipole-dipole interaction energy ( $\simeq 10000 \text{ k}_B\text{T}$ ) for a given size of the colloids.

#### 1.5.3 Boojum colloids

When particles are treated for planar anchoring, they create a pair of antipodal surface defects called boojums [3,34,35]. Figure 1.15 shows boojum defects in which a pair of dark spots on the poles of the microsphere each with a strength of -1/2. Fig. 1.15(c) shows the director distortion around the microsphere and observed under polarizing optical micrographs (POM) (Fig. 1.15(b)). The interaction between a pair of boojum colloids are quadrupolar and the potential energy shows  $r^{-5}$  dependence and hence boojum defects can be named as planar quadrupole.

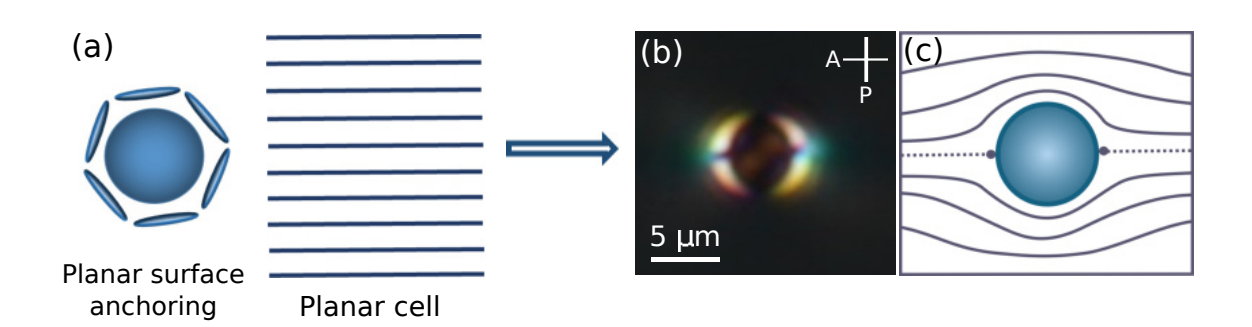


Figure 1.15: (a) Microsphere with planar surface anchoring in a uniformly aligned planar nematic cell. (b) Polarizing optical micrographs (POM) of microsphere with boojum defect. (c) Schematic representation of director distortion around the boojum colloid.

#### 1.5.4 Anisotropic colloids in nematic liquid crystals

Recently, there has been a growing interest in anisotropic colloids such as rod-like, star-shaped, peanut shaped, cubical, platelet type, ring-like particles etc [36–41]. Figure 1.16 shows POM images of a few anisotropic particles, dispersed in NLCs. For non-spherical particles, the orientations, induced topological defects and the elastic interactions are delicate to the shape and genus of the particles. Such colloids are very useful for designing self-assembled colloidal structures and superstructures.

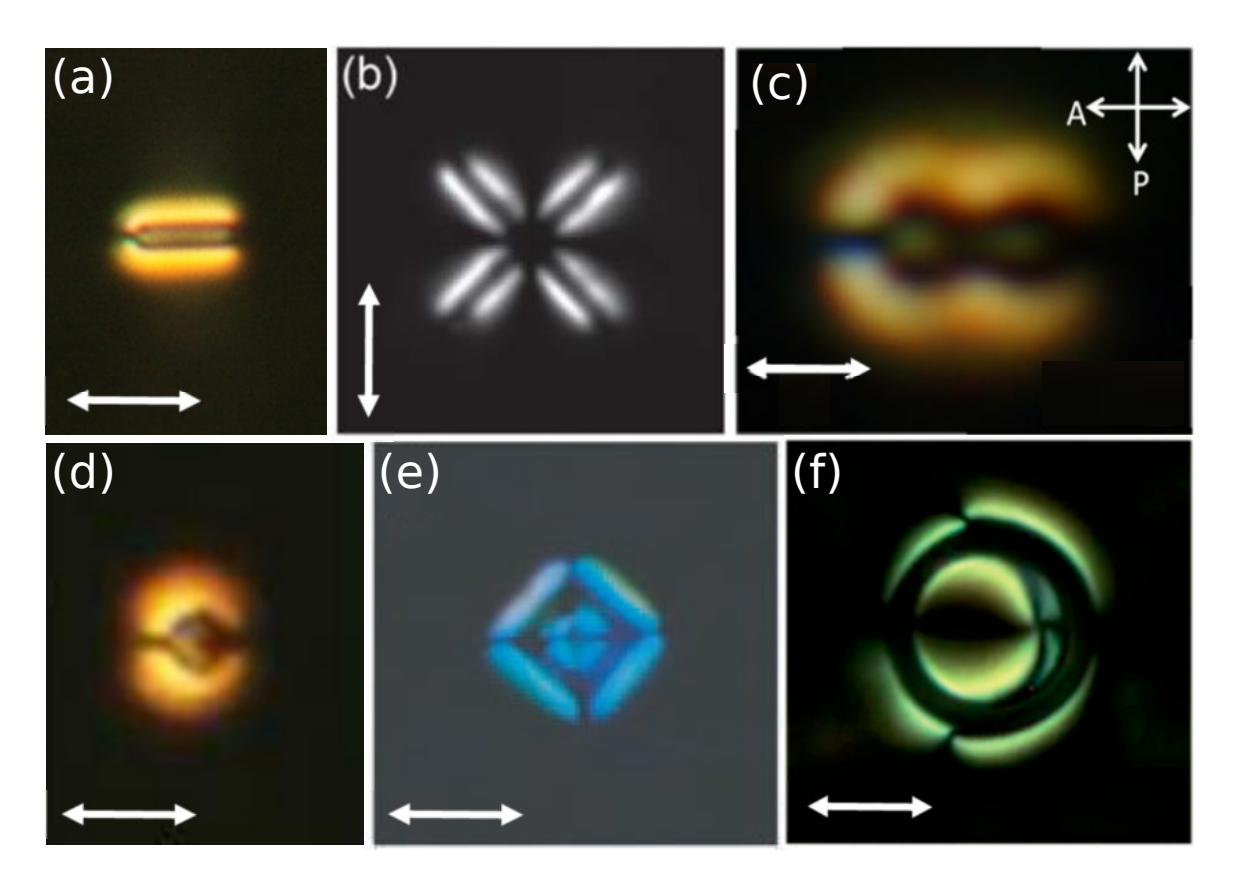


Figure 1.16: Polarizing optical micrographs (POM) of (a) rod-like, (b) star-shaped [37], (c) peanut shaped [39], (d) cubical [38], (e) platelets [40], and (f) ring shaped [41] particles dispersed in NLC. The white colour arrows indicate the nematic director. Images are adapted from the above mentioned references.

#### 1.5.5 Chiral nematic colloids

Chirality plays a significant role in condensed matter physics and beyond. The systems with the dispersion of micro or nano-sized colloidal particles in a chiral nematic liquid crystal (NLC) are called chiral nematic colloids [19, 44]. Such systems can be prepared simply by adding appropriate chiral dopant in to the NLC. Chirality has a large impact on colloidal interaction such as formation of metastable state, reconfigurable colloidal interaction in chiral nematics in 3D and 2D systems [19, 20]. Figure 1.17 shows a schematic diagram which represents the defect loop forms around a microsphere dispersed in chiral NLC with different chirality. Topological 1/2 disclination loops are observed in the helix direction around the particle surface. In case of  $\pi$  twisted cell (see Fig. 4.3(b)), the wrapping of a defect loop appears similar to "eight number" (Fig. 1.17(a)). If the chirality is further increased, the complexity of the defect loop increases with the twist in the cell as shown in Fig. 1.17(a-c). Tkalec et al. has explained the formation of knotted and linked loops of topological defects in chiral nematic colloids (Fig. 1.18(A-J)) [22].

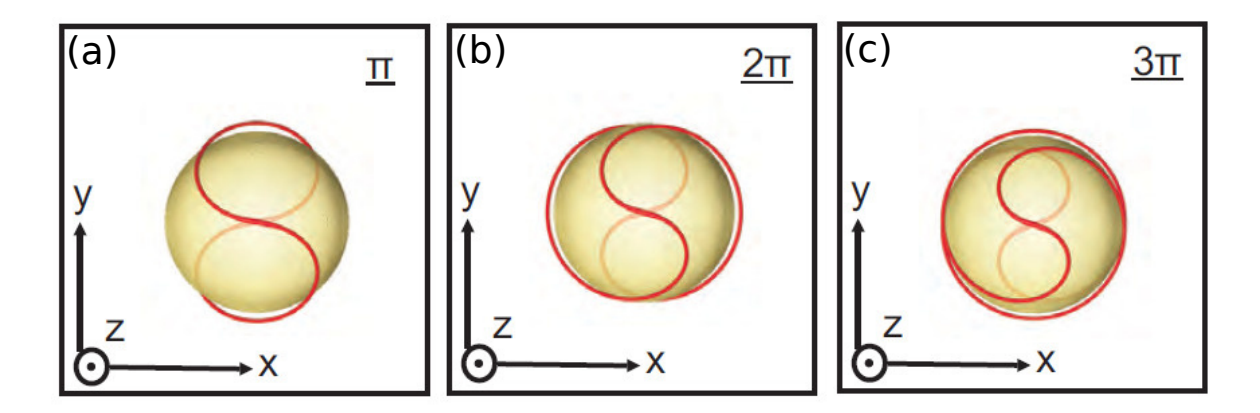


Figure 1.17: The defect loop around a spherical microparticle dispersed in (a)  $\pi$ -twisted, (b)  $2\pi$ -twisted and (c)  $3\pi$ -twisted chiral nematic liquid crystal cells. Defect lines are marked with red colour in all three images. Images are adapted from Ref. [20].

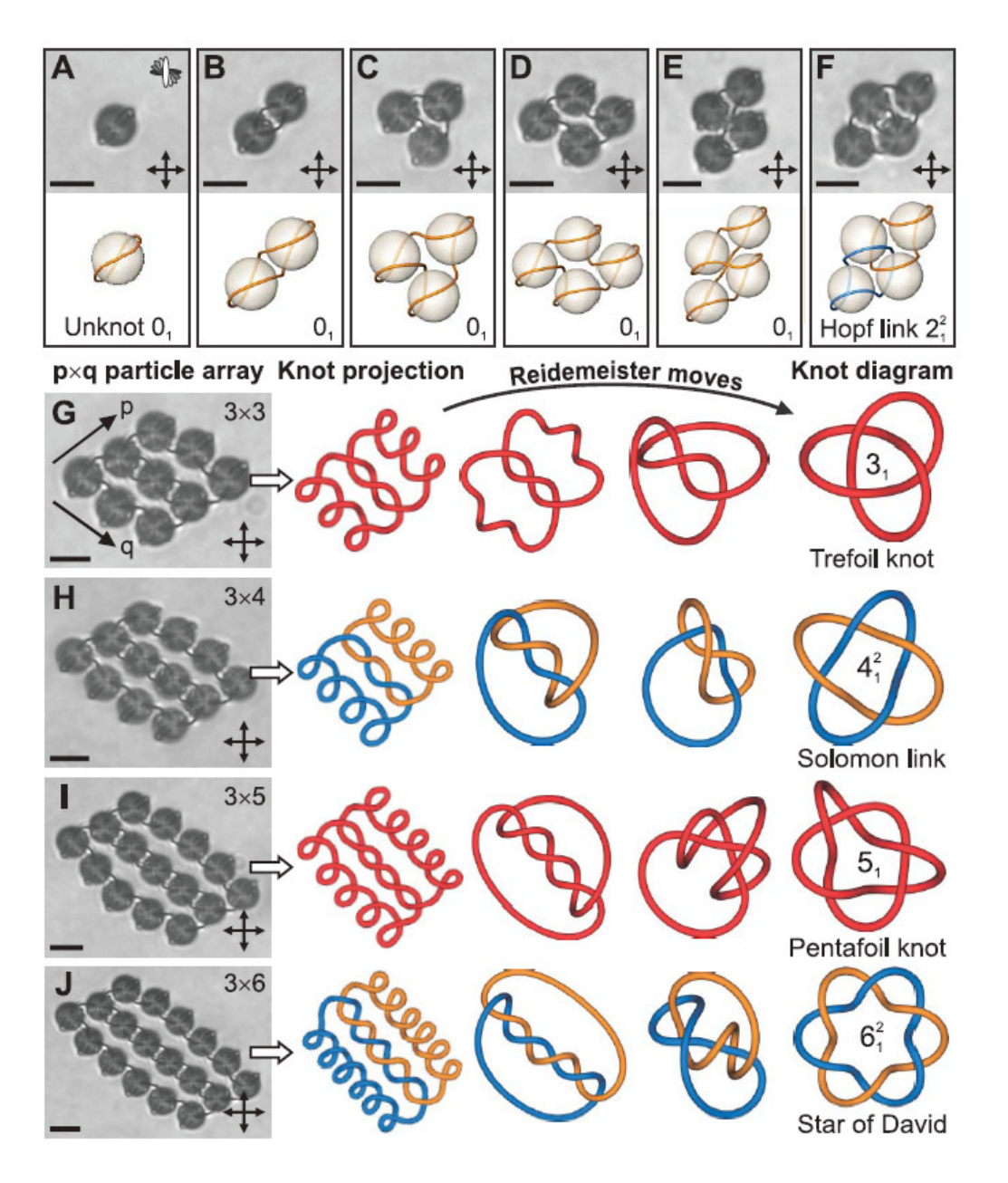


Figure 1.18: knotted and linked topological defect loops in chiral NLC. Images are adapted from Ref. [22].

# 1.6 Hydrodynamic interaction

Colloidal particles in a fluid stimulate long-range flows, and likewise respond to the fluid motion. Colloidal particles interact hydrodynamically with one another by generating and reacting to the local velocity of a fluid. In many physical systems, hydrodynamic interactions play a crucial part, including colloidal suspensions, solution polymers, and protein microscopy dynamics.

The hydrodynamic interaction of Brownian particles in aqueous solution was investigated by optically trapping a pair of microspheres at close separation. It was done by measuring the position of the particles and calculating the autocorrelation and cross-correlation functions. The traps were made by focusing orthogonally polarized laser beams of 1064 nm. The average position of individual spheres is determined by the position of the corresponding laser trap. Here, we present a brief theoretical description on the hydrodynamic interactions of two Brownian particles at close proximity [45]. This discussion will be useful for describing the experimental results in chapter-4.

Let  $r_1$  and  $r_2$  are the position of the trapped spheres, which can be tracked by using a video microscopy technique. The trajectories  $r_1(t)$  and  $r_2(t)$ , were measured for a pair of particles with mean separations,  $r=|r_1 - r_2|$ . The autocorrelation is calculated by analysing the Brownian motion of a single confined sphere. When a particle moving at a constant velocity U in a fluid of viscosity  $\eta$ , experiences a hydrodynamic drag force  $F_D$ . Here the force direction is opposite to the particle motion. The velocity of the sphere at the low-Reynold numeric limit is written as [46],

$$U = -b_0 F_D \tag{1.34}$$

where  $b_0$  is the particle's mobility. From the Stokes's law

$$b_0 = \frac{1}{6\pi na} \tag{1.35}$$

When a particle is bounded by a potential, U(x), the drag force increases. The net force acts on the particle consist of a Gaussian force f(t), along with an additional force due to the potential field,  $-\frac{dU}{dx}$ . Considering the potential is harmonic, the equation

of motion of a confined sphere can be written as Langevin equation,

$$\frac{dx}{dt} = b_0[f(t) - kx(t)] \tag{1.36}$$

where the Gaussian force f(t) can be well written as

$$\langle f(t) \rangle = 0$$
  
 $\langle f(t)f(t') \rangle = 2b_0^{-1}k_BT\delta(t - t')$  (1.37)

The position autocorrelation function  $\langle x(t)x(0)\rangle$  is deduced by solving the Langevin equation using conventional techniques. Since in the long time unit, it has just one characteristic time-scale, the autocorrelation decays exponentially.

$$\langle x(t)x(0)\rangle = \frac{k_BT}{k}exp\left(-\frac{t}{\tau}\right)$$
 (1.38)

where  $\tau$  is the decay time, which is the amount of time it takes a particle to diffuse a distance l, where  $l = \sqrt{\frac{2k_BT}{k}}$ .

The movement of a two bounded particles is different as compared to the previous case in that hydrodynamic interaction couples the two particles' motions together. When one particle moves, a flow in the surrounding fluid occurs, causing the location of a neighboring second particle to fluctuate. The cross correlation function of position of the particles interacted through hydrodynamic forces is examined here. It is assumed in this case that two trapped particles are the same size and are held in optical traps with similar force constants. In the framework of Langevin dynamics for a low Reynolds number system, the hydrodynamic interactions between two spheres can be described by a mobility tensor  $b_{ij}$ .

$$\begin{pmatrix} U_1 \\ U_2 \end{pmatrix} = \begin{pmatrix} b_{11} & b_{12} \\ b_{21} & b_{22} \end{pmatrix} \begin{pmatrix} F_1 \\ F_2 \end{pmatrix} \tag{1.39}$$

where the two spheres are tagged as 1 and 2 and consequently the equivalence of the two particles implies that  $b_{11} = b_{22}$  and  $b_{12} = b_{21}$ . Because the Stokes equation is linear, each of the matrices  $b_{ij}$  may be decomposed into a pair of mobility coefficients that represent motion either parallel to or perpendicular to the line of the centres [47].

$$b_{ij}(r) = A_{ij}(r)\frac{\hat{r}\hat{r}}{r^2} + B_{ij}\left(1 - \frac{\hat{r}\hat{r}}{r^2}\right)$$
 (1.40)

where the coefficients,  $A_{ij}$  and  $B_{ij}$  denote the longitudinal and transverse mobilities, respectively. Here, the discussion is restricted to only about longitudinal motion,  $A_{11}$  and  $A_{12}$  are the mobility coefficients needed for hydrodynamic studies. The coordinates  $x_1$  and  $x_2$  are mutually dependent because the mobility coefficient,  $A_{12}$ , links the fluctuations along the line of the two spheres' centres. Their cross correlation is determined from the solution of the Langevin equation

$$\begin{pmatrix} \dot{x}_1 \\ \dot{x}_2 \end{pmatrix} = \begin{pmatrix} A_{11} & A_{12} \\ A_{12} & A_{11} \end{pmatrix} \begin{pmatrix} f_1(t) - kx_1 \\ f_2(t) - kx_2 \end{pmatrix}$$
 (1.41)

where

$$\langle f_i(t) \rangle = 0$$
  
 $\langle f_i(t)f_j(t') \rangle = 2(A^{-1})_{ij}k_BT\delta(t-t')$  (1.42)

The normal coordinates  $X_i$  are introduced,

$$X_i = \sum_j c_{ij} x_j \tag{1.43}$$

The corresponding equation of motion can be written as [48],

$$\frac{dX_i}{dt} = -k\lambda_i X_i + F_i(t) \tag{1.44}$$

with i=1 or 2. It is proven that the  $c_{ij}$  matrix comprise of the normalised eigen vectors of mobility matrix  $A_{ij}$ . The normal modes are

$$X_{1} = \frac{1}{\sqrt{2}}(x_{1} + x_{2})$$

$$X_{2} = \frac{1}{\sqrt{2}}(x_{1} - x_{2})$$
(1.45)

where  $X_1$  is the symmetric relative motion and  $X_2$  is the antisymmetric relative motion between the two particles along the lines of their centres.  $\lambda_i$  is the mobility of the two modes, which are the eigenvalues of the matrix  $c_{ij}$ ,

$$\lambda_1 = A_{11} + A_{12}$$

$$\lambda_2 = A_{11} - A_{12}$$
(1.46)

while  $F_i$  satisfy the following,

$$\langle F_i(t) \rangle = 0$$

$$\langle F_i(t)F_j(t') \rangle = 2\delta_{ij}\lambda_i k_B T \delta(t - t')$$
(1.47)

The correlation functions are determined using the Eq. (1.44) as

$$\langle X_i(t)X_j(0)\rangle = \delta_{ij}\frac{k_BT}{k}exp\left(-\frac{t}{\tau_i}\right)$$
 (1.48)

where  $\tau_i$  is the decay time which can be written as

$$\tau_i = \frac{1}{k\lambda_i} \tag{1.49}$$

inverting the coordinate transformation of Eq. (1.43) gives

$$h_{ij}(t) = \frac{\langle x_i(t)x_j(0) \rangle}{\sqrt{\langle x_i^2 \rangle \langle x_j^2 \rangle}}$$
(1.50)

The normalized time auto and cross correlation functions can be written as

$$h_{11}(t) = \frac{1}{2} \left[ exp\left(-\frac{t}{\tau_1}\right) + exp\left(-\frac{t}{\tau_2}\right) \right]$$

$$h_{12}(t) = \frac{1}{2} \left[ exp\left(-\frac{t}{\tau_1}\right) - exp\left(-\frac{t}{\tau_2}\right) \right]$$
(1.51)

The auto and cross-correlation functions can also be written in terms of the vector component  $R_i$  (i = x, y, z) of the particle position and can be expressed as [49],

$$\langle R_{1,i}(t)R_{1,j}(0)\rangle = \langle R_{2,i}(t)R_{2,j}(0)\rangle$$

$$= \delta_{ij} \frac{k_B T}{2k_i} \left(e^{-t(1+\epsilon_i)/\tau_i} + e^{-t(1-\epsilon_i)/\tau_i}\right)$$
(1.52)

and

$$\langle R_{1,i}(t)R_{2,j}(0)\rangle = \langle R_{2,i}(t)R_{1,j}(0)\rangle$$

$$= \delta_{ij} \frac{k_B T}{2k_i} \left(e^{-t(1+\epsilon_i)/\tau_i} - e^{-t(1-\epsilon_i)/\tau_i}\right)$$
(1.53)

where  $\tau$  is the relaxation time that can be expressed as  $\tau = \zeta/k_i$  where  $k_i$  is the effective stiffness constant.  $\epsilon$  is a dimensionless parameter.

# References

- X. Chen et al., First-principles experimental demonstration of ferroelectricity in a thermotropic nematic liquid crystal: Polar domains and striking electro-optics. PNAS, vol. 117, pp. 14021-14031, 2020.
- [2] P. G. de Gennes and J. Prost, *The physics of liquid crystals*. 2nd Ed, Clarendon Press, Oxford, 1993.
- [3] H. Stark, Physics of colloidal dispersions in nematic liquid crystals. Phys. Rep., vol. 351, pp. 387-474, 2001.
- [4] S. Chandrasekhar, *Liquid Crystals*. Cambridge University Press, 1992.
- [5] M. Kleman and O. D. Lavrentovich, Soft Matter Physics: An Introduction. Springer-Verlag Berlin, 2003.
- [6] P. M. Chaikin and T. C. Lubensky, Principles of Condensed Matter Physics. Cambridge University Press, Cambridge, 2000.
- [7] W. H. de Jeu, *Physical properties of liquid crystalline materials*. Liquid Crystal Monographs, Gordon and Breach, 1980.
- [8] W. Maier and G. Meier, Z. Naturforsch, vol. 16a, pp. 262, 1961.
- [9] L. M. Blinov and V. G. Chigrinov, *Electrooptic effects in liquid crystal materials*. Springer-Verlag, New York, 1996.
- [10] H. Gruler and G. Meier, Electric field-induced deformations in oriented liquid crystals of the nematic type. Mol. Cryst. Liq. Cryst., vol. 16, pp. 299-310, 1972.

- [11] M. Kleman and O. D. Lavrentovich, Topological point defects in nematic liquid crystals. Philosophical Magazine, vol. 86, pp. 4117–4137, 2006.
- [12] N. D. Mermin, The topological theory of defects in ordered media. Rev. Mod. Phys., vol. 51, pp. 591-648, 1979.
- [13] T. C. Lubensky, D. Pettey and N. Currier, Topological defects and interactions in nematic emulsions. Phys. Rev. E, vol. 57, pp. 610-625, 1998.
- [14] J. Friedel, *Dislocations*. 1st Ed, Pergamon Press: Oxford, UK, 1964.
- [15] Y. H. Kim, D. K. Yoon, H. S. Jeong, O. D. Lavrentovich and H. Jung, Smectic liquid crystal defects for self-assembling of building blocks and their lithographic applications. Adv. Funct. Mater., vol. 21, pp. 610-627, 2011.
- [16] P. Poulin, H. Stark, T. C. Lubensky and D. A. Weitz, Novel colloidal interactions in anisotropic fluids. Science, vol. 275, pp. 1770-1773, 1997.
- [17] S. Ramaswamy, R. Nityananda, R. V. Aaghunathan and J. Prost, *Power-Law forces between particles in a nematic*. Mol. Cryst. Liq. Cryst., vol. 288, pp. 175-180, 1996.
- [18] B. I. Lev and P. M. Tomchuk, Interaction of foreign macrodroplets in a nematic liquid crystal and induced supermolecular structures. Phys. Rev. E, vol. 59, pp. 591-602, 1999.
- [19] V. S. R. Jampani, M. Skarabot, S. Copar, S. Zumer and I. Muševič, Chirality screening and metastable states in chiral nematic colloids. Phys. Rev. Lett., vol. 110, pp. 177801, 2013.
- [20] V. S. R. Jampani, M. Skarabot, M. Ravnik, S. Copar, S. Zumer and I. Muševič, Colloidal entanglement in highly twisted chiral nematic colloids: Twisted loops, Hopf links, and trefoil knots. Phys. Rev. E, vol. 84, pp. 031703, 2011.
- [21] J. S. Lintuvuori, K. Stratford, M. E. Cates and D. Marenduzzo, Colloids in cholesterics: size-dependent defects and non-Stokesian microrheology. Phys. Rev. Lett., vol. 105, pp. 178302, 2010.

- [22] U. Tkalec, M. Ravnik, S. Cŏpar, S. Zŭmer and I. Muševič, *Reconfigurable knots* and links in chiral nematic colloids. Science, vol. 333, pp. 62-65, 2011.
- [23] I. Muševič, M. Škarabot, U. Tkalec, M. Ravnik and S. Žumer, Two-dimensional nematic colloidal crystals self-assembled by topological defects. Science, vol. 313, pp. 954-958, 2006.
- [24] P. Poulin, V. Cabuil and D. A. Weitz, Direct measurement of colloidal forces in an anisotropic solvent. Phys. Rev. Lett., vol. 79, pp. 4862-4865, 1997.
- [25] I. Muševič, Optical manipulation and self-assembly of nematic colloids: colloidal crystals and superstructures. Liq. Cryst. Today, vol. 19, pp. 2-12, 2010.
- [26] S. Park, Q. Liu and I. I. Smalyukh, Colloidal surfaces with boundaries, apex Boojums, and nested elastic self-assembly of nematic colloids. Phys. Rev. Lett., vol. 117, pp. 277801, 2016.
- [27] A. Nych, U. Ognysta, M. Škarabot, M. Ravnik, S. Žumer and I. Muševič, Assembly and control of 3D nematic dipolar colloidal crystals. Nat. Commun., vol. 4, pp. 1489, 2013.
- [28] U. Ognysta et al., 2D interactions and binary crystals of dipolar and quadrupolar nematic colloids. Phys. Rev. Lett., vol. 100, pp. 217803, 2008.
- [29] B. I. Lev, S. B. Chernyshuk, P. M. Tomchuk and H. Yokoyama, Symmetry breaking and interaction of colloidal particles in nematic liquid crystals. Phys. Rev. E, vol. 65, pp. 021709, 2002.
- [30] S. Alama, L. Bronsard and X. Lamy Analytical description of the Saturn-ring defect in nematic colloids. Phys. Rev. E, vol. 93, pp. 012705, 2016.
- [31] H. Stark, Saturn-ring defects around microspheres suspended in nematic liquid crystals: an analogy between confined geometries and magnetic fields. Phys. Rev. E, vol. 66, pp. 032701, 2002.

- [32] M. V. Rasna et al., Orientation, interaction and laser assisted self-assembly of organic single-crystal micro-sheets in a nematic liquid crystal. Soft Matter, vol. 11, pp. 7674-7679, 2015.
- [33] M. Tasinkevych and D. Andrienko, Colloidal particles in liquid crystal films and at interfaces. Cond. Mat. Phys., vol. 13, pp. 33603, 2010.
- [34] Q. Liu, B. Senyuk, M. Tasinkevych and I. I. Smalyukh, Nematic liquid crystal boojums with handles on colloidal handlebodies. PNAS. U.S.A., vol. 110, pp. 9231-9236, 2013.
- [35] M. R. Mozaffari, M. Babadi, J. Fukuda and M. R. Ejtehadi, Interaction of spherical colloidal particles in nematic media with degenerate planar anchoring. Soft Matter, vol. 7, pp. 1107-1113, 2011.
- [36] U. Tkalec, M. Skarabot and I. Muševič, Interactions of micro-rods in a thin layer of a nematic liquid crystal. Soft Matter, vol. 4, pp. 2402-2409, 2008.
- [37] C. P. Lapointe, K. Mayoral and T. G. Mason, Star colloids in nematic liquid crystals. Soft Matter, vol. 9, pp. 7843–7854, 2013.
- [38] D. V. Sudhakaran, R. K. Pujala and S. Dhara, Orientation dependent interaction and self-assembly of cubic magnetic colloids in a nematic liquid crystal. Adv. Opt. Mater., vol. 8, pp. 1901585, 2020.
- [39] D. K. Sahu, T. G. Anjali, M. G. Basavaraj, J. Aplinc, S. Čopar and S. Dhara, Orientation, elastic interaction and magnetic response of asymmetric colloids in a nematic liquid crystal. Scientific reports, vol. 9, pp. 81, 2019.
- [40] C. P. Lapointe, T. G. Mason and I. I. Smalyukh, Shape-controlled colloidal interactions in nematic liquid crystals. Science, vol. 326, pp. 1083-1086, 2009.
- [41] B. Senyuk et al., Topological colloids. Nature, vol. 493, pp. 200-205, 2013.
- [42] S. V. Burylov and Y. L. Raikher, Orientation of a solid particle embedded in a monodomain nematic liquid crystal. Phys. Rev. E, vol. 50, pp. 358-367, 1994.

- [43] M. D. Lynch and D. L. Patrick, Organizing carbon nanotubes with liquid crystals. Nano Lett., vol. 2, pp. 1197–1201, 2002.
- [44] S. Čopar, T. Porenta, V. S. R. Jampani, I. Muševič and S. Žumer, Stability and rewiring of nematic braids in chiral nematic colloids. Soft Matter, vol. 8, pp. 8595-8600, 2012.
- [45] P. Bartlett, S. I. Henderson and S. J. Mitchell, Measurement of the hydrodynamic forces between two polymer-coated spheres. Phil. Trans. R. Soc. Lond. A, vol. 359, pp. 883-895, 2001.
- [46] J. Happel and H. Brenner, Low Reynolds number hydrodynamics. Englewood Cliffs, NJ:Prentice-Hall, 1965.
- [47] G. K. Batchelor, Brownian diffusion of particles with hydrodynamic interaction.J. Fluid. Mech., vol. 74, pp. 1-29, 1976.
- [48] M. C. Wang and G. E. Uhlenbeck, On the theory of the Brownian motion II. Rev. Mod. Phys., vol. 17, pp. 323, 1945.
- [49] J. C. Meiners and S. R. Quake, Direct measurement of hydrodynamic cross correlations between two particles in an external potential. Phys. Rev. Lett., vol. 82, pp. 2211, 1999.

# **Experimental Setup**

#### 2.1 Introduction

In this chapter, we discuss about the experimental set up used in this thesis. First we describe surface treatment of the particles and preparation of colloidal dispersion including liquid crystal cell preparation. Experimental techniques such as optical tweezers and principle of trapping of particles in LCs are explained. Also the method of manipulation of topological defects in liquid crystals is explained briefly at the end of this chapter.

# 2.2 Preparation of liquid crystal cells

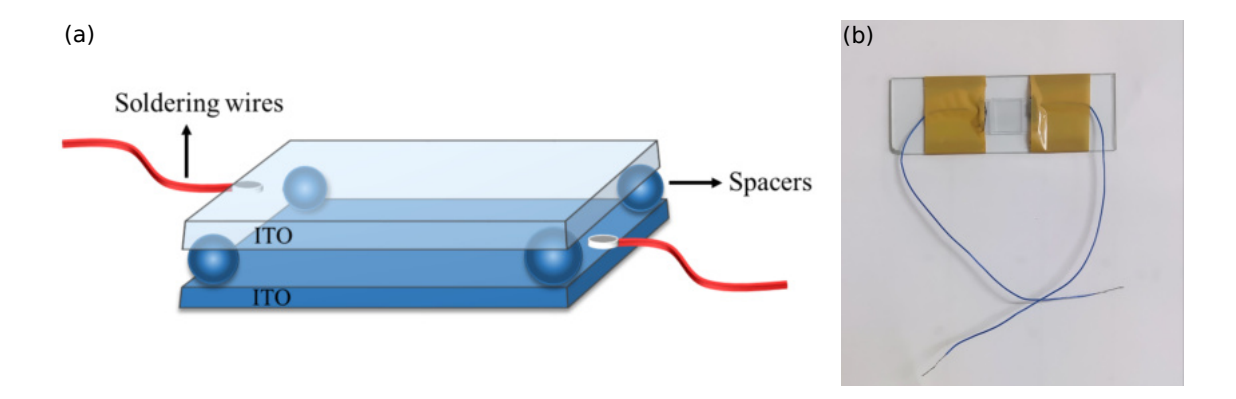


Figure 2.1: (a) Schematic diagram of a liquid crystal cell. (b) Photograph of the LC cell used in the experiment. The overlapped region is where LC colloids are dispersed.

A pair of indium-tin-oxide (ITO) coated glass sheets (area  $1.5 \times 1.1 \text{ cm}^2$ ) of thickness 0.7 mm are used to prepare liquid crystal cells. The ITO glass plates are cleaned thoroughly several times by using soap water. They are further cleaned through sonication

using an ultrasonicator water bath with distilled water and acetone. After cleaning, the glass plates are dried by blowing nitrogen gas. Then AL-1254 Polyimide is spin coated on the ITO coated side of the glass plates. Spin coating has done in two steps. In the first step, spin coater rotates at a speed of 4000 rotation/minute (rpm) for 20 seconds and 6000 rpm in the next 20 seconds. The coated glass plates are cured in a hot furnace at 180 °C for one hour. The cured glass-plates are rubbed unidirectionally with a rubbing machine to get planar cells in which the LC director is oriented along the rubbing direction. Finally, a pair of glass plates are attached antiparallely one over another with their rubbed side facing each other. They are attached using a UV curable adhesive (NOA-81) and silica spacers which provides required cell gap. For electric field experiments, copper wires are connected to the cells using ultrasonic soldering (Sunbonder USM-IV). Figure 2.1(a) shows the top view of a cell schematically. A photograph of the cell is shown (Fig. 2.1(b)). Also a flowchart that describes different stages of cell preparation describes in Fig. 2.2. A standard interference technique is used to measure the cell gap with the help of a high resolution spectrometer (Ocean Optics HR4000CG-UV-NIR).

#### 2.2.1 Thickness measurement of LC cell

The reflection probe of the Ocean Optics spectrometer consist of 7 optical fibers as shown in Fig. 2.3(a). The empty cell is kept under reflection probe and it is illuminated by light through outer six fibres of the probe. Reflected light is collected by central fibre and signal is detected through the spectrometer. The spectrum consist of alternative maxima and minima as shown in Fig. 2.3(b) and is analysed using a SpectraSuite software. The thickness of the gap between the cell is calculated by using the formula,

$$d = \frac{\lambda_m \lambda_n}{\lambda_n - \lambda_m} \times \frac{n - m}{2} \tag{2.1}$$

where  $\lambda_m$  and  $\lambda_n$  are wavelengths of  $\mathbf{m}^{th}$  and  $\mathbf{n}^{th}$  maxima or minima respectively.

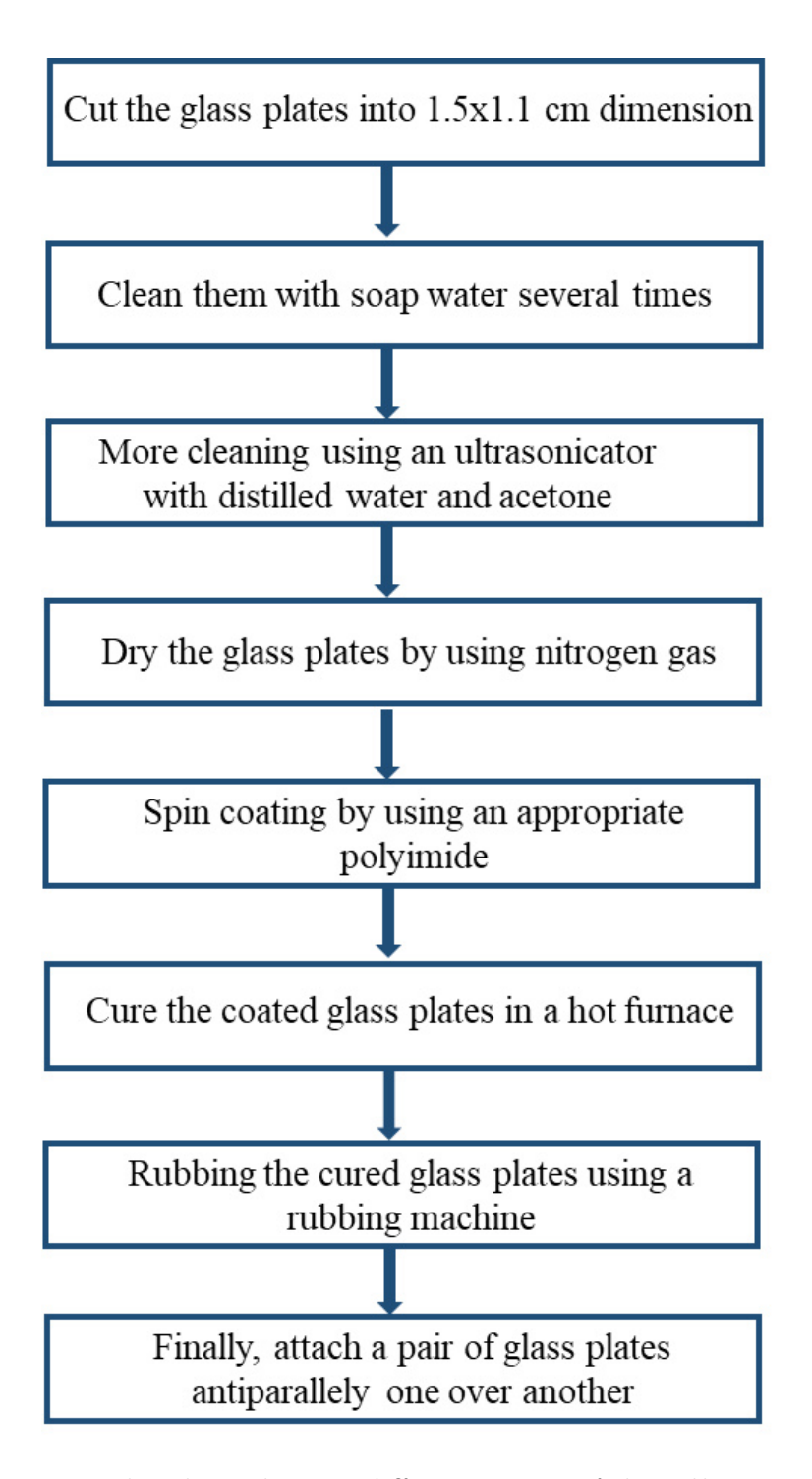


Figure 2.2: Flowchart showing different stages of the cell preparation.

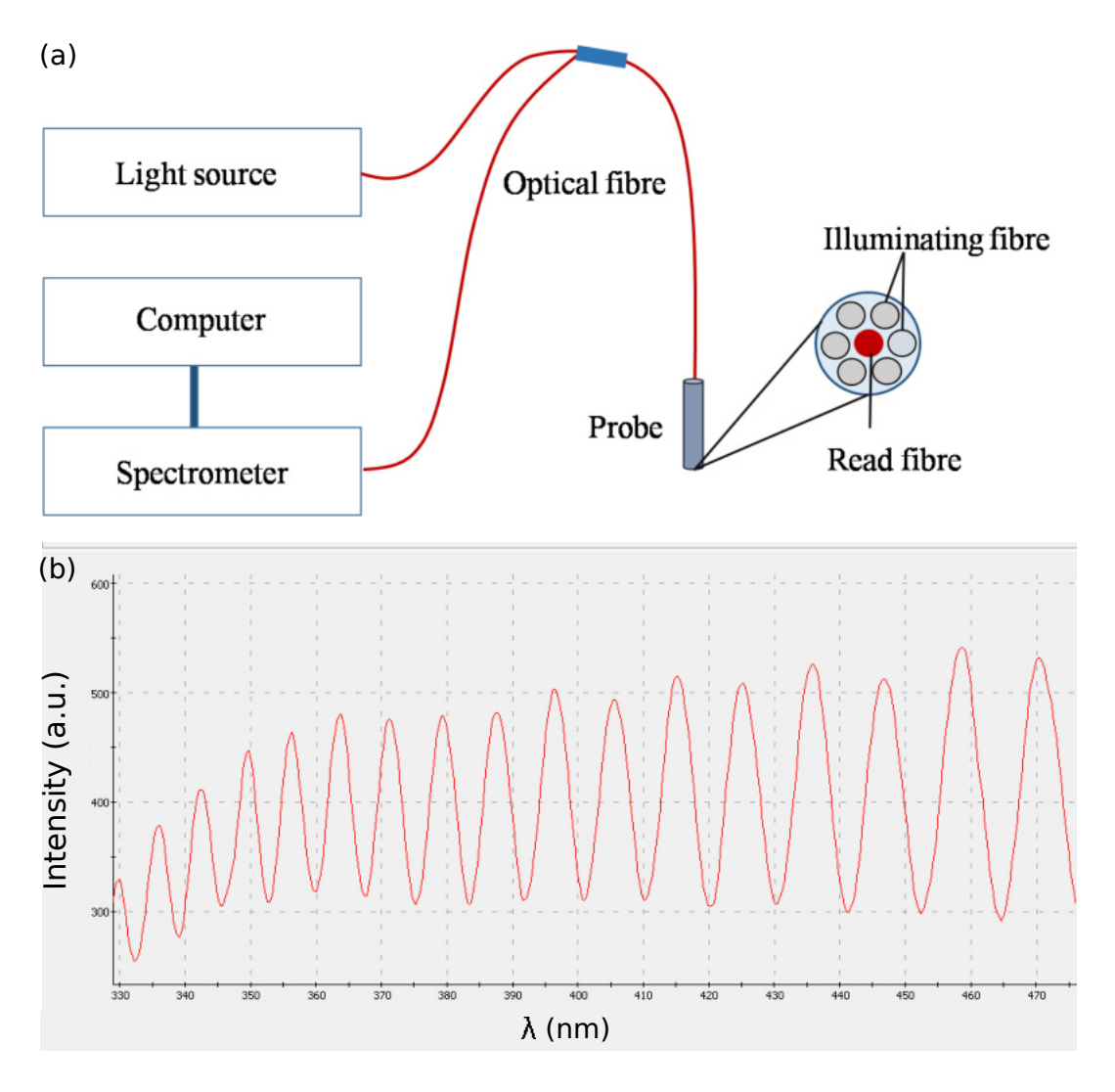


Figure 2.3: (a) Schematic diagram for measurement of cell thickness. (b) The intensity variation from an empty cell.

# 2.3 Liquid crystals and colloidal particles

We used several liquid crystals for our experiments. Chemical formula of the LCs used are represented in Fig. 2.4. 5CB (4-cyano-4'-pentylbiphenyl) is a room temperature nematic LC having a typical birefringence  $\Delta n \simeq 0.18$ . The dielectric anisotropy of 5CB is positive. The compound C8H17PyPhOC10H21 exhibits following phase transitions: Cr 33.2 °C SmC 57.7 °C SmA 65.5 °C N 68 °C I. We used CB15 (4-cyano-40-(2-methylbutyl)-biphenylene) as a chiral agent for preparing chiral nematic. It has the following phase transitions: Cr 4 °C N\* 54 °C I. The liquid crystal MLC-6608 is a room temperature nematic mixture, where  $\Delta \epsilon < 0$ . The birefringence of MLC-6608 at room temperature is  $\Delta n \simeq 0.08$ .

Figure 2.4: Chemical formula and phase sequence of 5CB, CB15 and C8H17PyPhOC10H21 liquid crystals.

#### 2.3.1 Colloidal particles used in the experiments

We mostly used rod-shaped silica nano and microparticles with two different sizes. Particles with length 6.5  $\mu$ m and diameter 0.75  $\mu$ m are designated as micro-rods and particles with length 3  $\mu$ m and diameter 200 nm are designated as nano-rods. The silica micro and nano-rods were synthesized by a wet chemical method and prepared follow-

ing the procedure reported by Kujik et al. [1]. 3 gm of PVP (Polyvinylpyrrolidone) was first dissolved in 30 ml of 1-pentanol. Then 3 ml ethanol (100 percent, Interchema), 0.84 ml Milli Q water, and 0.2 ml aqueous sodium citrate dyhydrate (0.17 M, 99 percent Sigma-Aldrich) were added after full dissolution of PVP. The mixture was thoroughly mixed and bubbles were removed. Finally, 0.3 mL of Tetraethyl orthosilicate (TEOS, 98 percent Sigma-Aldrich) was applied to the reaction mixture, gently shaken, and allowed to proceed for 24 hours. After centrifuging and fractionating the mixture, micro and nano rods were obtained with the desired aspect ratio. To impose homeotropic anchoring of the LC molecules on the particle's surface, the particles were treated with a surface coupling agent called DMOAP (N,N-dimethyl-Noctadecyl-3-aminopropyl-trimet-hoxy-silyl chloride) [2,3]. The planar surface anchoring of the LC molecules on the particle's surface is achieved by using another coupling agent called MAP (N-methyl-3-aminopropyltrimethoxysilane). Fig. 2.5 shows the molecular structures of these surface coupling agents. LC mesogens align on the coated particle's surface by physicochemical processes and the anisotropic forces generated from functionalized surface coupling agent.

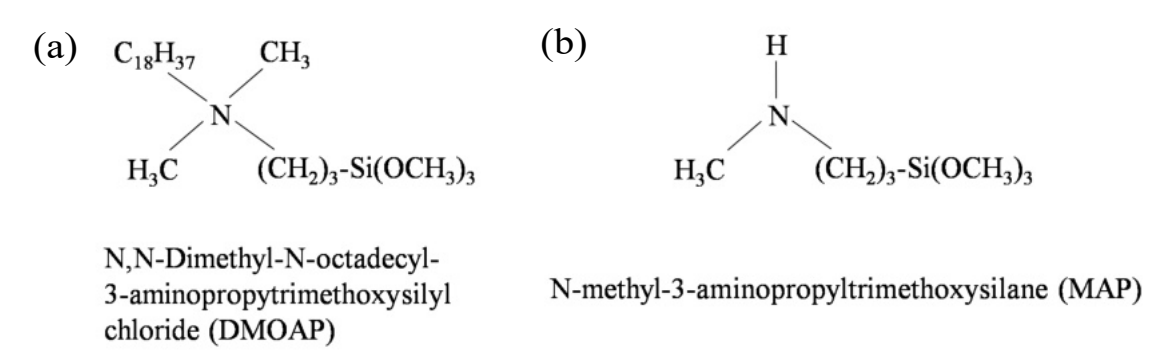


Figure 2.5: Chemical formula of surface coupling agents (a) DMOAP and (b) MAP.

Figure 2.6(a) shows a flow chart that describes the steps involved in DMOAP coating. Surface treatment procedure is as follows: We prepare a colloidal solution by mixing untreated silica particles and 500  $\mu$ l of distilled water in a 1 ml centrifuge tube and add 2 wt percentage of DMOAP or MAP (whichever is needed) solution to above prepared colloidal solution. Then mix the solution for 5 minutes to obtain uniform alignment of octadecyl chains on the particle surface. This can be done by placing our solution in a vortex mixer. After mixing, we centrifuge it for 6 minutes with appropriate rpm to remove excess solution from the treated silica particles. We remove the solution

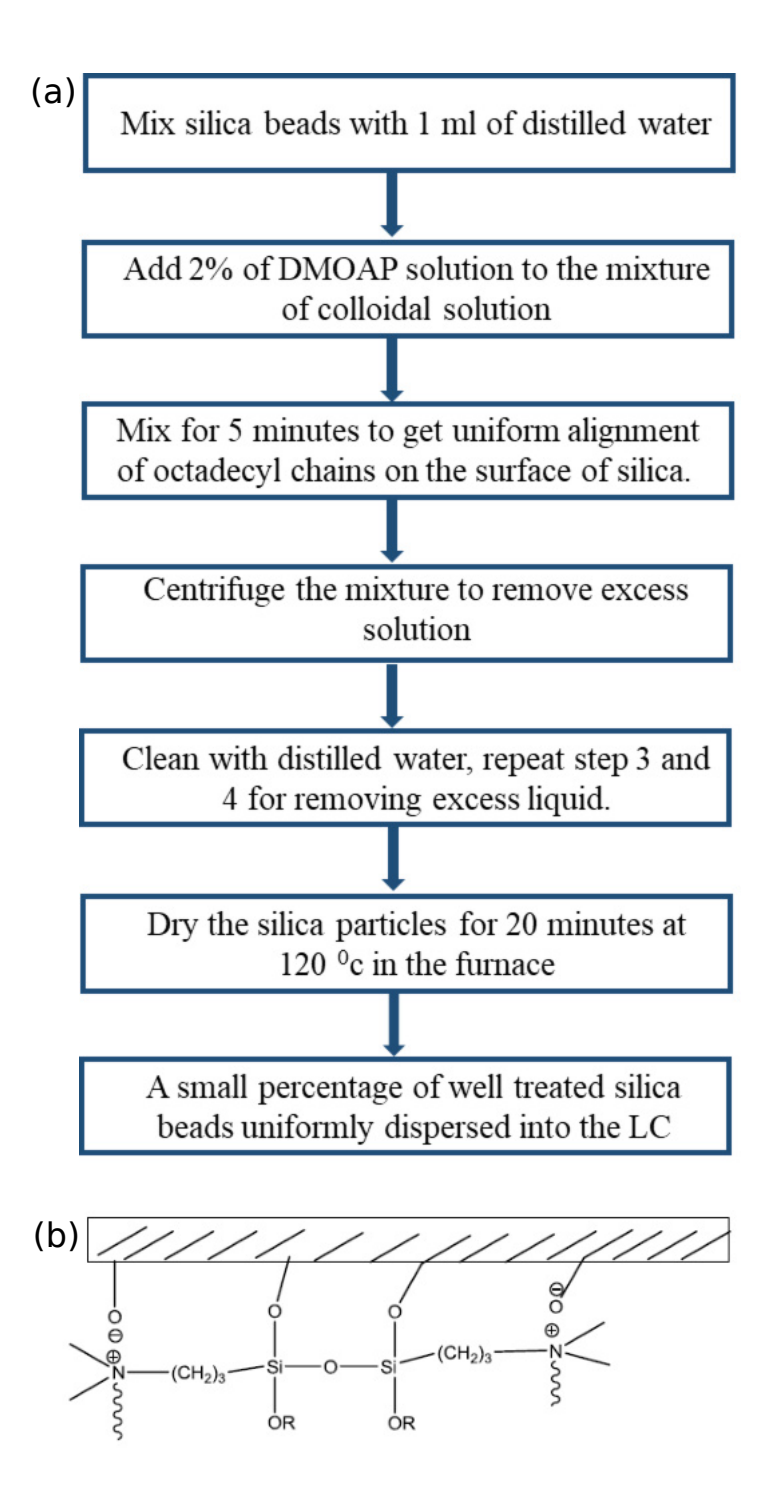


Figure 2.6: (a) The step by step procedure for DMOAP coating. (b)Formation of DMOAP film on treated Silica

in the centrifuge tube by keeping the sedimented particles at the bottom. Then we clean it with distilled water again, and repeat the process for 3 or 4 times. We dry the surface treated particles for 20-25 minutes at 120 °C in a hot furnace. Finally the prepared particles were uniformly dispersed in nematic liquid crystal to obtain liquid crystal colloids. Figure 2.6(b) shows the octadecyl hydrocarbon chains lying normal to the substrate that provides homeotropic anchoring to the LC molecules.

# 2.4 Lambda-plate imaging for determining director orientation

The interference colours observed in the liquid crystal medium with an additional  $\lambda$ -plate kept in between the polarizer and the sample, have been used to determine the orientation of LC directors. This can be achieved by comparing the interference colours with the colours of the Michel-Levy chart [4,5]. Interference colours are divided into orders according to the magnitude of the retardation: 0-550 nm (first order), 550-1100 nm (second order), 1100-1650 nm (third order). A graphical representation of the classical Michel-Levy interference colour chart is presented in the Fig. 2.7, which helps us to understand the order of retardation.

When microparticles are dispersed in a uniformly aligned LC media, they create elastic distortion around them. To study the director orientation around the particle, images were captured under crossed polarizers with an additional  $\lambda$ -plate (retardation plate) inserted between polarizer and sample. The first order retardation plate introduces a relative retardation of exactly one wavelength (530 nm) between ordinary and extraordinary wavefronts. Such wavefronts do not pass through because they are perpendicular to the analyzer (see Fig. 2.8(a)). But orthogonal wavefronts of all other wavelengths experience some degree of retardation, and therefore able to pass a component vector through the analyzer. The effect of  $\lambda$ -plate in polarized white light by a combination of three different wavefronts are shown in Fig. 2.8. Magenta-red colour is observed when a first order retardation plate is kept in the optical path as a result of combination of all visible light spectrum with green wavelength band is missing (blocked by the analyzer). This can be observed in the absence of the sample.

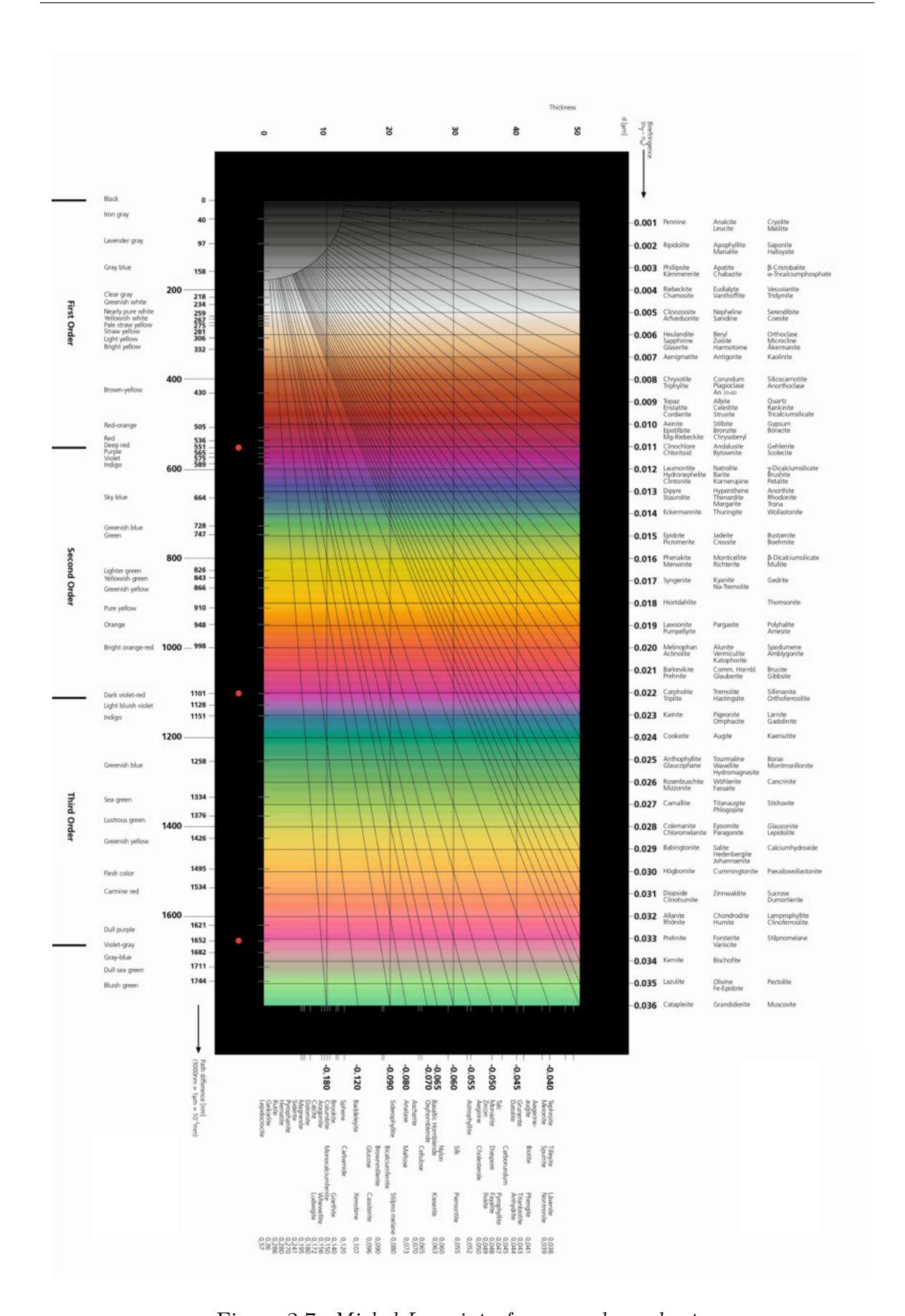


Figure 2.7: Michel-Levy interference colour chart

When a birefringent sample with a wavefront ellipsoid parallel to the retardation plate is inserted into the optical path, then the colour band will be shifted to longer wavelength, i.e. red colour. Then blue and green wavelength will be elliptically polarized and display second order blue (see Fig. 2.8(b)). But when the sample is rotated by 90 degrees, ellipsoidal wavefront will be perpendicular to the retardation plate, which cause the colour band to shift towards the blue side. Then elliptically polarized green and red wavelengths recombine to form a first order yellow colour (Fig. 2.8(c)).

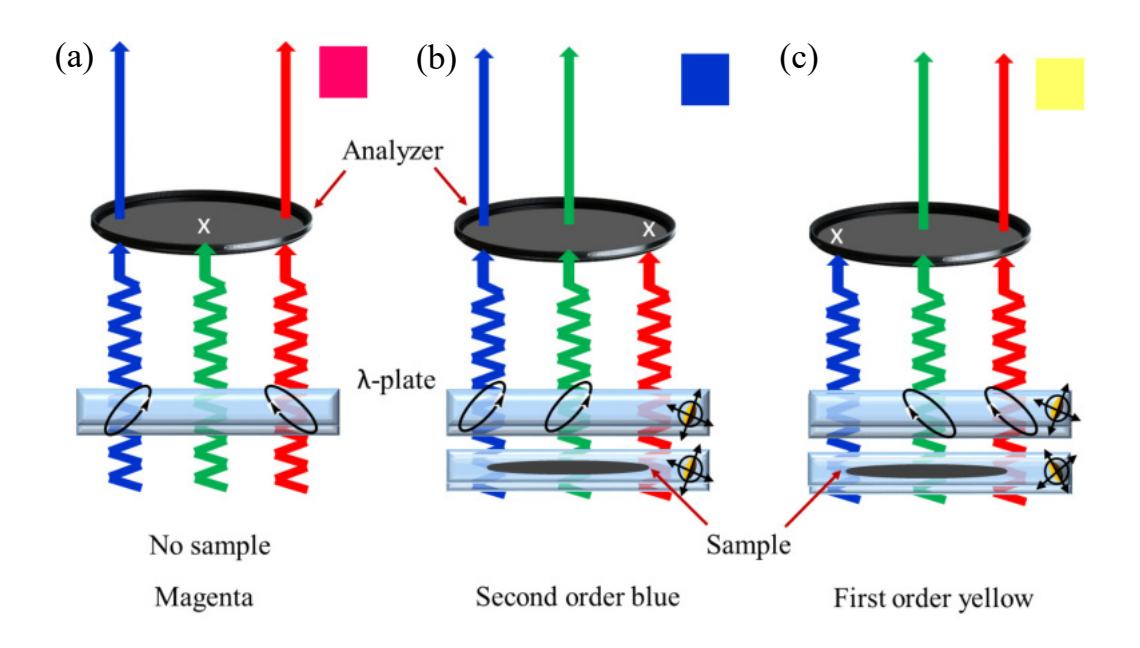


Figure 2.8: The effect of  $\lambda$ -plate in polarized white light, shown by a combination of red, green, and blue wavefronts. (a) Without a specimen in the optical pathway. A birefringent specimen is added in the optical pathway with an ellipsoidal wavefront (b) parallel and (c) perpendicular to the retardation plate. Adapted from Olympus website.

This method helps us to study the director orientation around the colloidal particle in liquid crystals. As we discussed, the images are captured under crossed polarizers with a  $\lambda$ -plate inserted between the polarizer and the sample. The relation between the liquid crystal orientation and the observed colour with inserted  $\lambda$ -plate is shown in Fig. 2.9(a). The magenta colour relates to a parallel or perpendicular director orientation with respect to the polarizer, whereas blue and yellow colours represent clock-wise and anticlock-wise rotation of the director, respectively. Photograph of a first order retardation plate in the laboratory is illustrated in Fig. 2.9(b). A dipolar

microsphere of 5.2  $\mu$ m is shown with crossed polarizer (Fig. 2.9(c)) and an additional  $\lambda$ -plate with slow axis oriented as shown, inserted between the polarizers and sample (Fig. 2.9(d)). It is observed that the region just above the micro-sphere is bluish and the region just below is yellowish, which suggests that the liquid crystal director is rotated clockwise above and anti-clockwise below the microsphere. The director distortions surrounding a dipolar microsphere is schematically shown in Fig. 2.9(e), where the defect is situated on the right side.

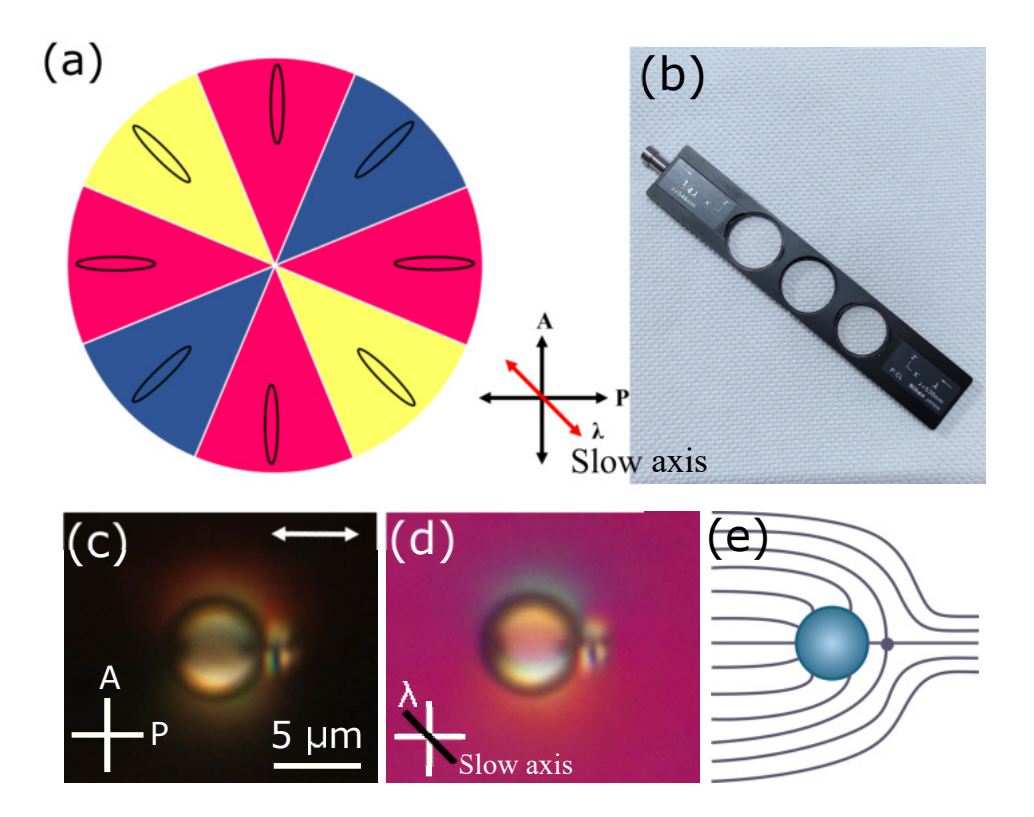


Figure 2.9: (a) Relation between the liquid crystal orientation and observed colour under polarizing microscope with inserted  $\lambda$ -plate. Red arrow shows the slow axis of the  $\lambda$ -plate. (b) First order retardation plate with a retardation of 530 nm. Polarizing optical microscopy (POM) images of a dipolar microsphere with, (c) crossed polarizers and (d) an additional  $\lambda$ -plate with slow axis oriented as shown, inserted between the polarizers and sample. (e) The LC director distortions around a microsphere with dipolar defect.

### 2.5 Optical tweezers

For our experiments, a laser tweezer is built on an inverted polarizing microscope (Nikon Eclipse Ti-U) using a CW solid state laser working at 1064 nm. The advantage of using an inverted microscope is, it gives larger stability and ease of multiple beam incorporation. The optical set-up schematically shown in Fig. 2.10. The inverted microscope is equipped with a halogen lamp, a polarizer and an analyzer, sample stage, objective and several ports for connecting cameras. On one of the two left ports, a colour camera (Nikon DS-Ri2, colour) is connected with a suitable adapter. On the right side, a CCD camera (IDS UI-3370CP, 2048-2048 pixels, resolution 4.19 MPix, black/white) is connected for particle manipulation and recording the video. The sample mounted on the XY-stage is illuminated by a halogen lamp. The XY-stage movement in the focal plane can be controlled by using a joystick which is connected with a controller. Objectives used in our experiments are 60X air (WD = 2.6 - 1.8mm), 60X water immersion (WD = 2.8 mm) and 100X water immersion (WD = 2.5mm). The high numerical aperture (NA) are used to create tightly focused laser spot on the sample with limited diffraction. For high temperature liquid crystals, a hotstage along with a PID controller (Instec Inc.) is used with an accuracy of  $\pm 0.1$  °C. The sample is placed on a hot stage, which is connected with temperature controller is kept above the XY-stage. All other optical devices are connected with our computer through various programmes. A photograph of our optical tweezer setup is presented in Fig. 2.11.

An acousto-optic deflector (AOD) is connected with the laser tweezer, which enables us to create and control multiple traps simultaneously. The AOD and the required software were purchased from Aresis. The AOD which is connected to the laser tweezer has a safety switch is to switch off the laser in case of any emergency. Using a laser beam of about 1 Watt is sufficient to trap and even manipulate around 100 colloidal particles. The piezo-transducer creates sound waves of a certain wavelength  $\lambda$  in the TeO<sub>2</sub> crystal and incoming laser beam is deflected by the sound wave created in TiO<sub>2</sub> crystal inside AOD (Fig. 2.12). The direction of the diffracted beam is determined by a Bragg's condition and is given by  $\Delta\theta = \lambda f/\nu$ . Finally, the deflected beam is focused

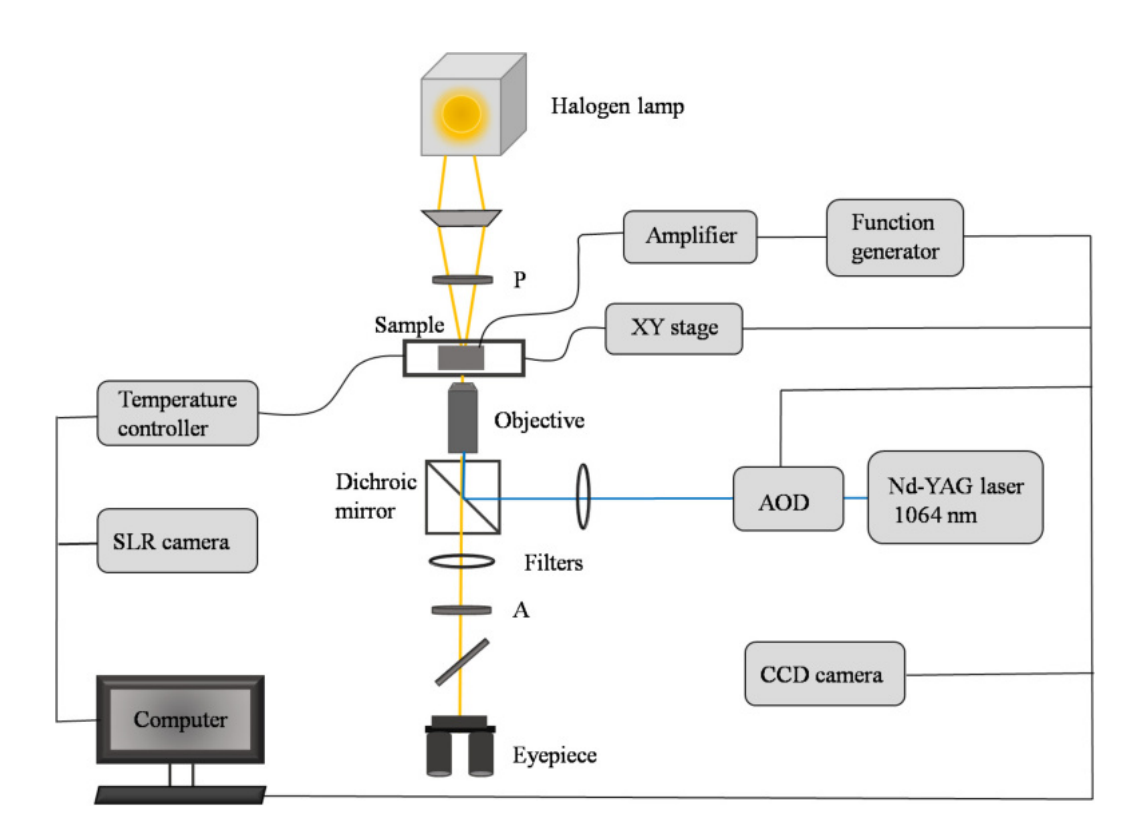


Figure 2.10: Schematic diagram of the laser tweezers.

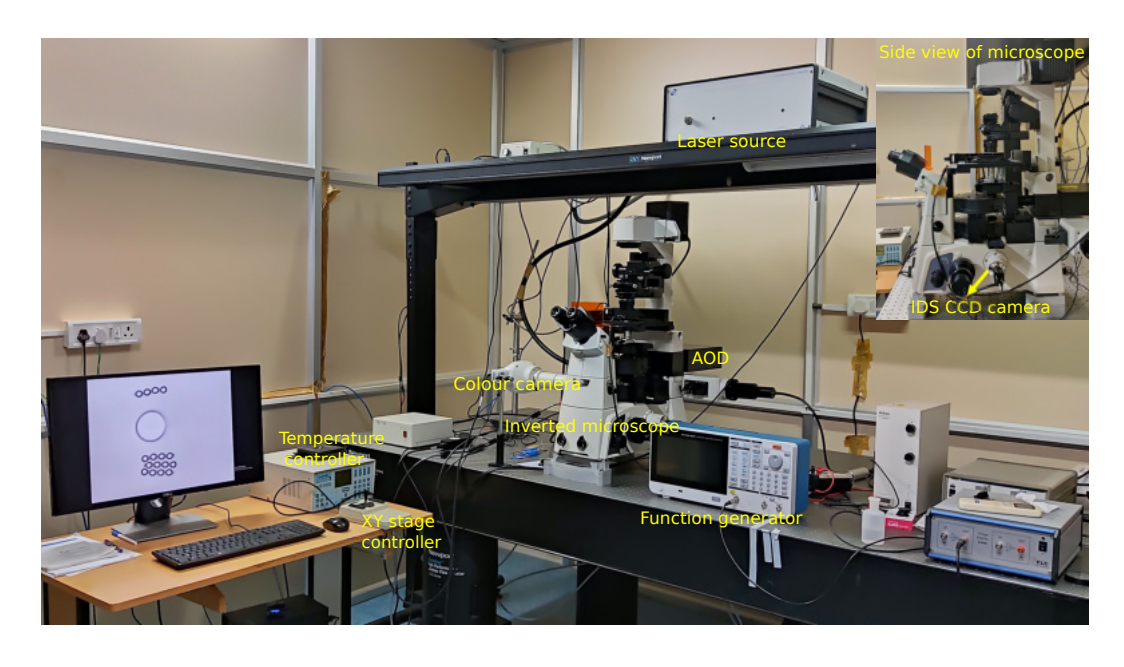


Figure 2.11: The Photograph shows the Laser tweezers setup. Side view of microscope is given in the inset. Some of the components are marked in the image with yellow colour.

into our sample through the objective connected to the microscope.

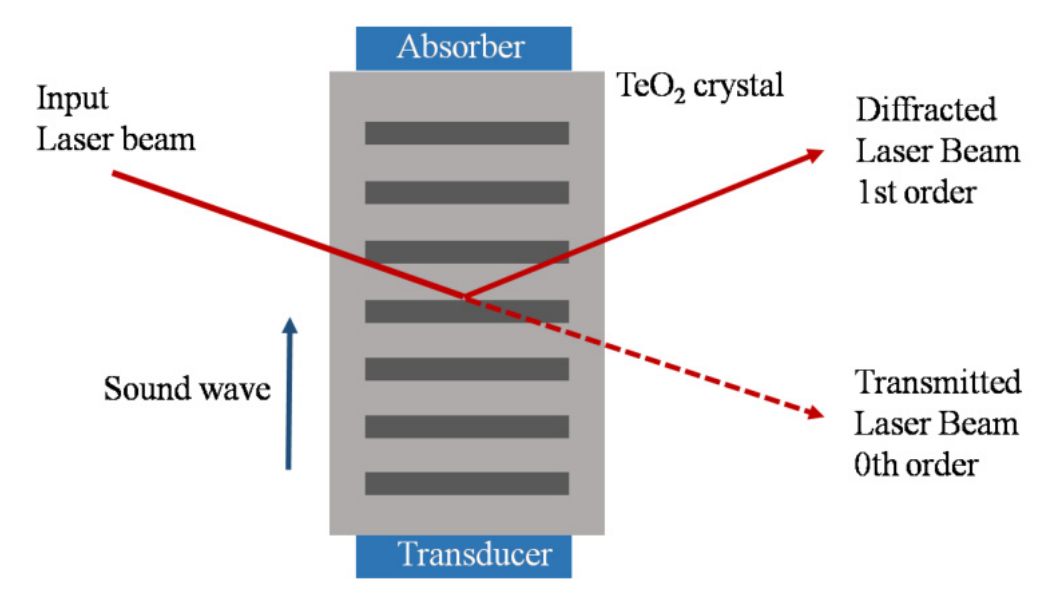


Figure 2.12: Schematic diagram of acousto-optic deflector (AOD)

# 2.5.1 Trapping of particles in isotropic media using optical tweezers

As we mentioned, optical tweezers are used to trap and manipulate particles in range from  $\mu$ m to nm and also to measure the forces acting on these particles [6]. The particles which we use to trap has to be dielectric, for example, atoms, molecules, micron-size beads, bacteria, biological cells etc.

Trapping occurs due to the radiation pressure of laser which results by the momentum change of light. We used the high intensity of tightly focused laser of 1064 nm for tweezer operation. The radiation force arising from the momentum change of the light either pushes the particle from the focus or hold it in the focal plane against the gravitation. Theoretical descriptions of trapping of colloidal particles are categorized into two regimes [7]. The first one is the Rayleigh scattering regime, where the particle size is smaller than the wavelength, i.e.  $r \ll \lambda$  and second one is Mie scattering regime, where  $r \gg \lambda$ . For optical trapping, laser light exerting on the dispersed particles in host medium is majorly divided into two components, scattering force and gradient force. The stability of the particles in the laser focus can be achieved by balancing these two forces along with the gravitational force.

In the Rayleigh regime, the scattering force acts in the laser propagation direction, is given by [8],

$$F_{scatt} = \frac{128\pi^5 r^6}{3\lambda^4} \left(\frac{m^2 - 1}{m^2 + 2}\right)^2 \frac{n_m}{c} I_0 \tag{2.2}$$

where  $I_0$  is the laser beam intensity, r is the particle size and  $m = n_p/n_m$ , where  $n_m$  and  $n_p$  are the refractive index of the medium and particle, respectively. The gradient force, which acts in the normal direction to the high intensity region is given by

$$F_{grad} = \frac{n_m^3 r^3}{2} \left( \frac{m^2 - 1}{m^2 - 2} \right) \nabla E^2 \tag{2.3}$$

A stable trap is possible when the gradient force dominates over the scattering force  $(F_{grad}/F_{scatt} >> 1)$  [9]. And we need a microscope objective with high numerical aperture (water or oil immersion). Also particle refractive index should be larger than that of surrounding medium  $(n_p >> n_m)$ . But mechanism is different in the Mie regime, where  $r >> \lambda$  (see Fig. 2.13). Here colloidal particles act as a lens and can be treated under ray optics picture. Light ray carries momentum and bend when they pass through a spherical particle. The corresponding force acting on the particle is the vector sum of the forces resulting from the ensemble of rays that contain the light beam [11]. A schematic representation of how trapping works in the Mie regime is shown in Fig. 2.13. The rectangular bar on the top designate the gradient profile of the laser beam. The light rays are refracted and pass through the trapped sphere, produce a net momentum (Fig.2.13(a)). The difference in momentum creates an equal and opposite force on the spherical particle indicated by red arrows.  $F_a$  and  $F_b$  are the force imparted to the spherical beads by first and second rays which are denoted by black arrows. The net force acts upward represented by black arrows, which is balanced by downward scattering force. In the second case, the particle is slightly shifted towards left side (Fig.2.13(b)). Here the thickness of the arrows represents their intensity, where brighter light rays (on the right) exert more force on the particle than dimmer ray (left). The resulting force indicates the particle is pulled towards the right side and net force is indicated by a black arrow.

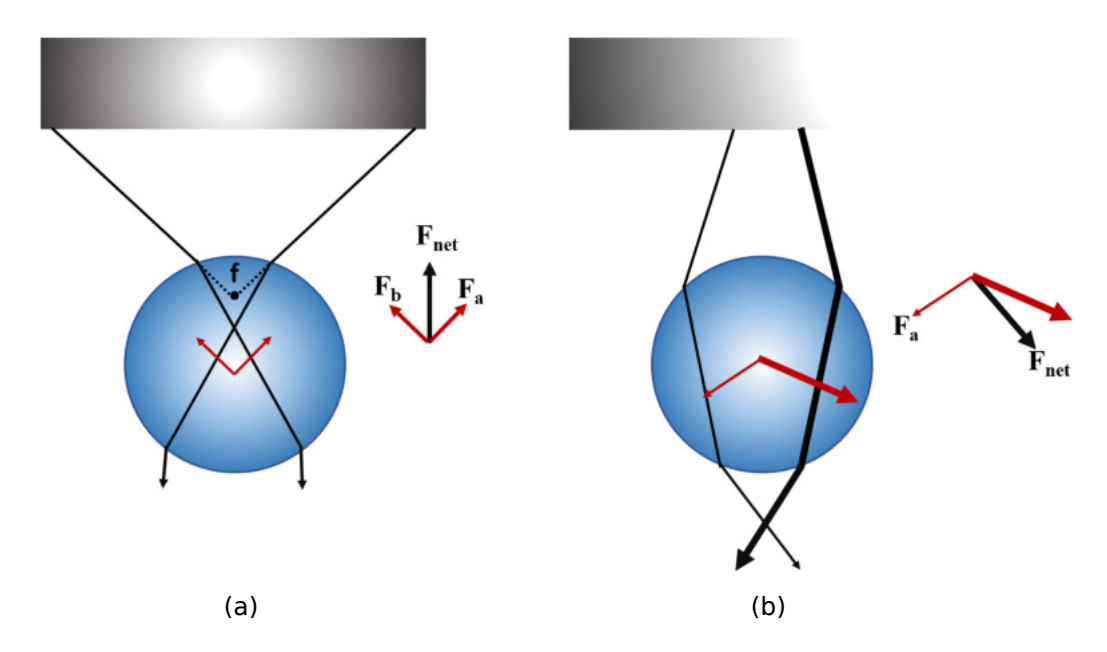


Figure 2.13: (a) The particle is located above the laser focus. The black arrows are refracted and pass through the transparent sphere produce a net momentum. (b) In this case the right ray represents more force than the left ray. The resulting forces shown by grey arrows indicate that the particle is pulled to the rightwards towards the light. The sum of the forces produce a net force indicated with black arrows.

# 2.5.2 Optical trapping and manipulation of microspheres in LCs

The laser trapping is very helpful for the manipulation of small colloidal particles and analysing their anisotropic forces in nematic liquid crystals [10]. As mentioned earlier, for a stable trapping, particle refractive index should be larger than that of host medium. But the silica particles which is used in our experiment has low refractive index (n=1.4) as compared to the average refractive index of the liquid crystals (for example 5CB, n=1.59), where the particle is dispersed. This is contrary to the basic tweezing principle.

#### 2.5.3 Trapping in planar cell

There are many different ways to trap low refractive index spheres in LCs [12–16]. One of the techniques is the creation of local distortion in the birefringent host media with a laser beam of low power. This creates a "ghost" colloid that can interact via structural forces of the LC with the real colloid. We used a time sharing mechanism for the creation of multiple traps using AOD. In nematic liquid crystals, the order difference between locally heated region and the surrounding leads to a fluid flow. The net fluid flow is opposite to the trap movement due to temperature dependent expansion and contraction. This works as a lower order parameter region and thus attracts the colloids.

In our experiments, we have used the ghost colloid method using laser beam and its interaction with a real colloid to manipulate particles (Fig. 2.14). An isotropic region is created using local heating within the LC medium. It can be seen as a dark grey line in Fig. 2.14(a). The isotropic-nematic interface is clearly visible due to the refractive index mismatch. Fig. 2.14(b) shows a  $\lambda$ -plate image, it is used to determine the anchoring of the nematic director around the molten region. Figure 2.14(c) represents the corresponding director distortion [17].

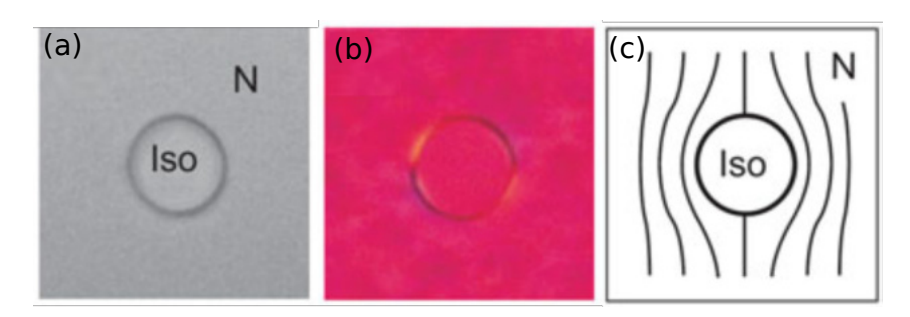


Figure 2.14: Images of a locally heated 5CB. The local heating leads the melting of nematic and an isotropic bubble is created. Images are adapted from Ref. [17].

The isotropic region acts as a trapping site for the particle, attracting the real colloid over several micrometers. A sequence of images showing a trapping event at large laser power in a planar 5CB LC cell is shown in Fig. 2.15. Here the molten region (ghost colloid) interacts with the point defect of the dipole.

Optical tweezers can be utilised to convert dipoles to quadrupoles and vice versa

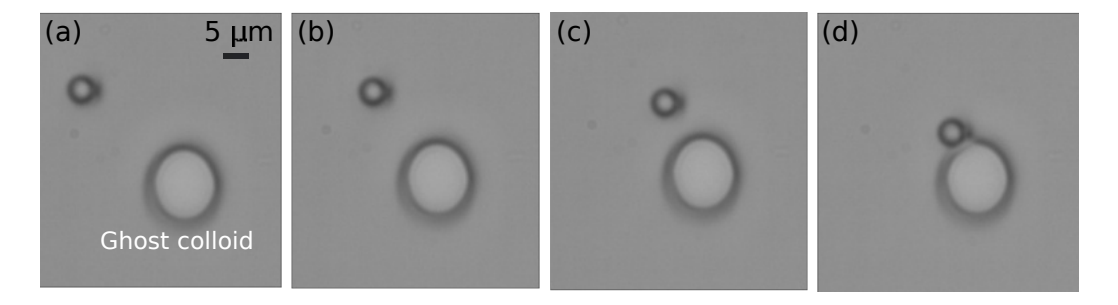


Figure 2.15: Sequence of images showing a trapping event at large laser power in 5CB liquid crystal in planar cell. The size of the colloid is 5.2  $\mu$ m and the cell thickness is 10  $\mu$ m.

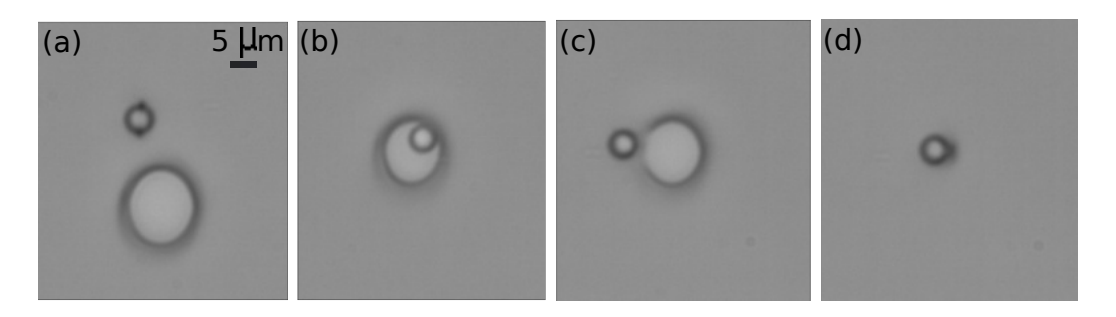


Figure 2.16: Sequence of images showing the conversion of quadrupolar defect structure into dipolar defect structure using the optical trap in a planar cell. The size of the colloid is 5.2  $\mu m$  and the cell thickness is 10  $\mu m$ .

and also to change the position of the point defects, which is the key factor in assembling of complex colloidal structures. Figure 2.16 shows the conversion of Saturn ring defect into a hyperbolic hedgehog defect by using the optical trap. In nematic liquid crystal, colloidal particles have an inherent tendency to self-assemble through long range elastic interaction. Different stages of laser directed assemblies of 2D colloidal crystal [18,19] are shown in figure 2.17. Particles are collected and assembled as up and down (anti-parallel) dipolar chains. By exploiting the particle interaction, it is possible to construct a variety of self-assembled and complex colloidal structures [20].

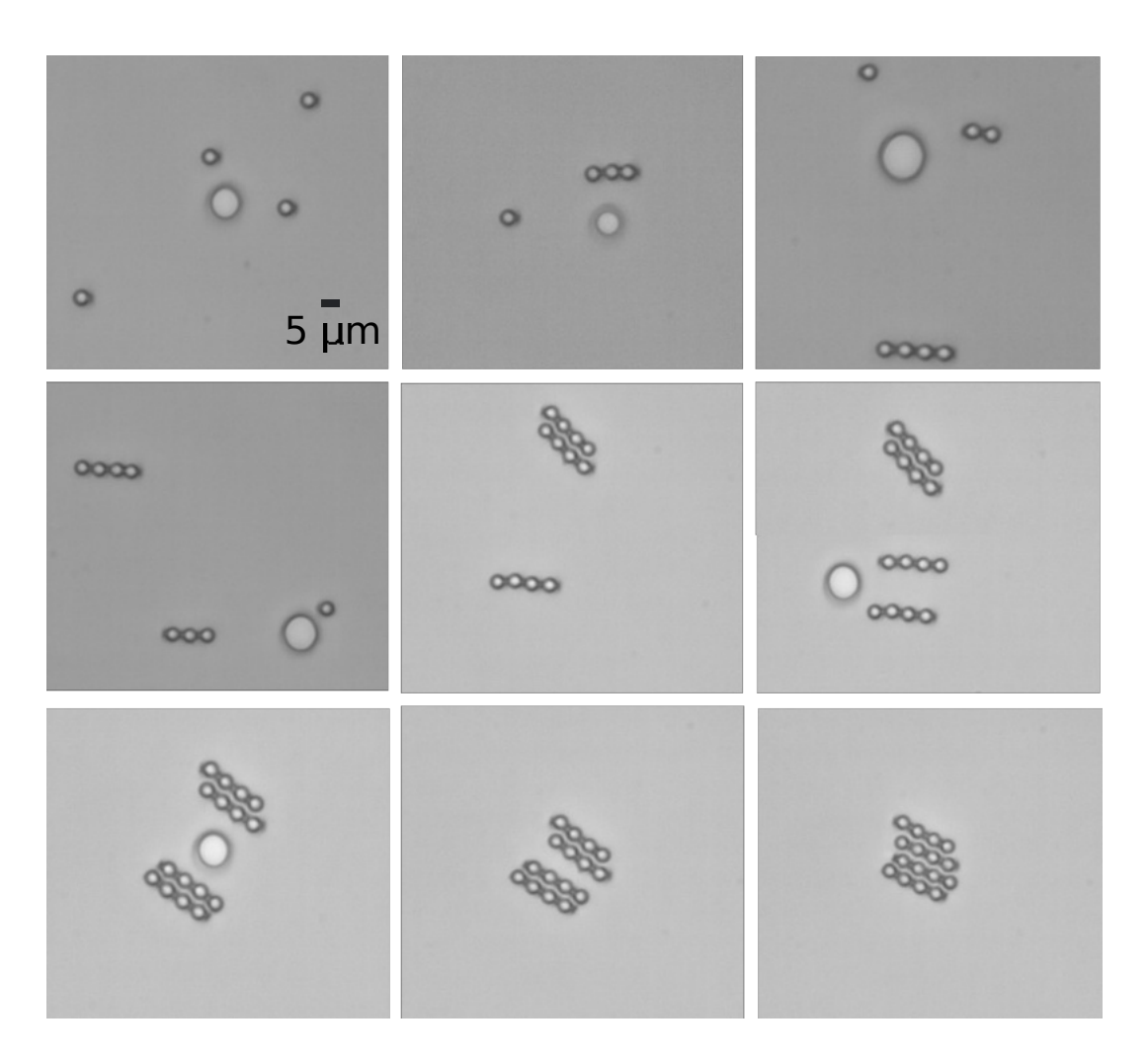


Figure 2.17: Snapshots showing the construction of 2D dipolar colloidal crystal in nematic phase. The laser assisted assembly of colloids is clearly seen from the images. The size of the colloid is 5.2  $\mu$ m and the cell thickness is 10  $\mu$ m.

#### 2.5.4 Video analysis and particle tracking

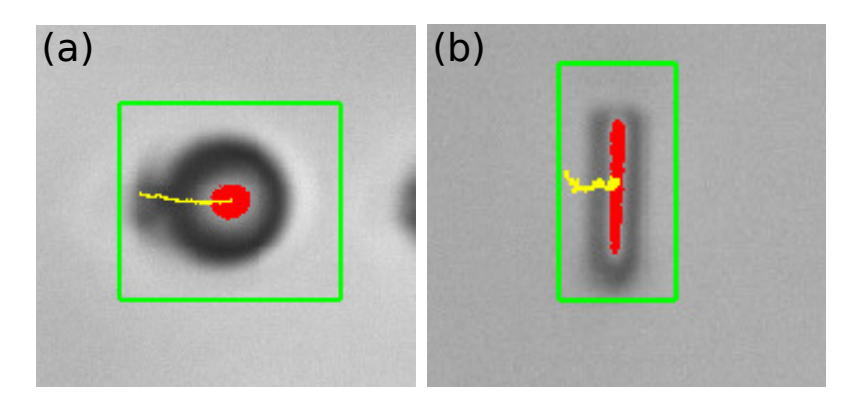


Figure 2.18: Tracking of a (a) microsphere of diameter 5.2  $\mu$ m and (b) micro-rod of length 7.5  $\mu$ m and diameter 800 nm using partTrack program. The centre of the highlighted intensity of the red region is the position of the particle and yellow line indicates the trajectory of the particle.

We used particle tracking program to track the particle. To record the video, an iDS CCD camera is attached to the right port of the inverted microscope (see Fig. 2.11). Video analysis enables us to determine the trajectories of individual particles from the recorded video. We manually select the particles to be tracked and link positions in each image of the particle with corresponding positions in later images which can be used to produce the trajectory. This requires determining which particle in a given image is most likely to correspond to the one in the preceding image. If the particles are indistinguishable, as for monodisperse spherical particles, this likelihood can only be estimated by comparing the proximity in the two images. It is also possible to track the position of anisotropic particles and extract their trajectory. Figure 2.19 shows the snapshots of tracking of the microparticles using a program. The program calculates weighted intensity average (center of gravity of image brightness) of red points. For spherical particle, the accuracy is approximately 10 nm [18]. In the case of rod shaped particles, position reading could be less accurate as compared to the spherical particles.

# References

- [1] A. Kuijk, A. van Blaaderen and A. Imhof, Synthesis of monodisperse, rodlike silica colloids with tunable aspect ratio. J. Am. Chem. Soc., vol. 133, pp. 2346-2349, 2011.
- [2] F. J. Kahn, Orientation of liquid crystals by surface coupling agents. Appl. Phys. Lett., vol. 22, pp. 386–388, 1973.
- [3] K. Kočevar and I. Muševič, Surface-induced nematic and smectic order at a liquid-crystal-silanated-glass interface observed by atomic force spectroscopy and brew-ster angle ellipsometry. Phys. Rev. E, vol. 65, pp. 021703, 2002.
- [4] R. Shah and N. Abbott, Orientational transitions of liquid crystals driven by binding of organoamines to carboxylic acids presented at surfaces with nanometer-scale topography. Langmuir, vol. 19, pp. 275-284, 2003.
- [5] Y. Zou, J. Namkung, Y. Lin, D. Ke and R. Lindquist, Interference colors of nematic liquid crystal films at different applied voltages and surface anchoring conditions. Optics Express, vol. 19, pp. 3297-3303, 2011.
- [6] N. Osterman, TweezPal Optical tweezers analysis and calibration software. Comput. Phys. Commun., vol. 181, pp. 1911-1916, 2010.
- [7] D. G. Grier, Optical tweezers in colloid and interface science. Curr. Opin. Colloid Interface Sci., vol. 2, pp. 264-270, 1997.
- [8] A. Ashkin, J. M. Dziedzic, J. E. Bjorkholm and S. Chu, Observation of a singlebeam gradient force optical trap for dielectric particles. Opt. Lett., vol. 11, pp. 288-290, 1986.

- [9] A. Ashkin, Forces of a single-beam gradient laser trap on a dielectric sphere in the ray optics regime. Biophysical journal, vol. 61, pp. 569-582, 1992.
- [10] R. P. Trivedi D. Engstrom and I. I Smalyukh, Optical manipulation of colloids and defect structures in anisotropic liquid crystal fluids. J. Opt., vol. 13, pp. 044001, 2011.
- [11] K. Svoboda and S. M. Block, Biological applications of optical forces. Annu. Rev. Biophys. Biomol. Struct., vol. 23, pp. 247-285, 1994.
- [12] M. Yada J. Yamamoto and H. Yokoyama, Direct observation of anisotropic interparticle forces in nematic colloids with optical tweezers. Phys. Rev. Lett., vol. 92, pp. 185501, 2004.
- [13] I. Muševič, M. Škarabot, D. Babič, N. Osterman, I. Poberaj, V. Nazarenko and A. Nych, Laser trapping of small colloidal particles in a nematic liquid crystal: clouds and ghosts. Phy. Rev. Lett., vol. 93, pp. 187801, 2004.
- [14] M. Škarabot, M. Ravnik, D. Babič, N. Osterman, I. Poberaj, S. Žumer, I. Muševič, A. Nych, U. Ognysta and V. Nazarenko, Laser trapping of low refractive index colloids in a nematic liquid crystal. Phy. Rev. E, vol. 73, pp. 021705, 2006.
- [15] I. I. Smalyukh, A. N. Kuzmin, A. V. Kachynski, P. N. Prasad and O. D. Lavrentovich, Optical trapping of colloidal particles and measurement of the defect line tension and colloidal forces in a thermotropic nematic liquid crystal. Appl. Phys. Lett., vol. 86, pp. 021913, 2005.
- [16] O. V. Kuksenok, R. W. Ruhwandl, S. V. Shiyanovskii and E. M. Terentjev, Director structure around a colloid particle suspended in a nematic liquid crystal. Phys. Rev. E, vol. 54, pp. 5198-5203, 1996.
- [17] I. Muševič, Liquid Crystal Colloids. Springer International Publishing, 1st edition, 2017.
- [18] I. Muševič, M. Škarabot, U. Tkalec, M. Ravnik and S. Žumer, Two dimensional nematic colloidal crystals self-assembled by topological defects. Science, vol. 313,

#### References

- pp. 954-958, 2006.
- [19] U. Ognysta, A. Nych, V. Nazarenko, M. Škarabot and I. Muševič, Design of 2D binary colloidal crystals in a nematic liquid crystal. Langmuir, vol. 25, pp. 12092–12100, 2009.
- [20] I. Muševič and M. Škarabot, Self-assembly of nematic colloids. Soft Matter, vol. 4, pp. 195-199, 2008.

3

Colloidal analogues of polymer chains, ribbons and 2D crystals employing orientations and interactions of silica nano-rods dispersed in a nematic liquid crystal

# 3.1 Introduction

The interplay of topological defects and elastic interaction between particles dispersed in NLC leads to complex, one to three-dimensional colloidal structures and superstructures [1,2]. The diversity in the structure is introduced by varying the shape, size and genus of the colloidal particles [3–8]. There are several theoretical and experimental studies in recent years, dealing with the orientation and interaction of non-spherical particles such as rod-shaped colloids, patchy colloids, star colloids, cubical colloids, peanut-shaped colloids, Janus beads etc., [9–13]. In this chapter, we present experimental studies on the dispersion of silica nano-rods in a nematic liquid crystal. We discuss the spontaneous orientation, elastic interaction and directed co-assembly of nano-rods with micro-rods and microspheres in a nematic liquid crystal. Using laser tweezers, we designed colloidal analogues of linear polymer chains, ribbons, and two-

dimensional binary colloidal crystals. By designing an appropriate polymer as the base unit, more complex colloidal structures can be developed, which could be useful for photonic applications.

# 3.2 Experimental

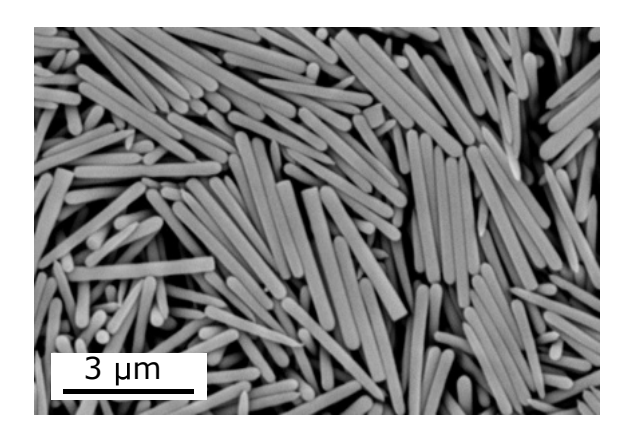


Figure 3.1: Scanning electron microscope (SEM) image of silica nano-rods of average length and diameter are  $l=3~\mu m$  and d=200~nm, respectively.

The silica rods were synthesized by a wet chemical method and prepared following the procedure reported by Kujik et al [14]. 3 gm of PVP (Polyvinylpyrrolidone) was first dissolved in 30 ml of 1-pentanol. 3 ml ethanol (100 percent, Interchema), 0.84 ml Milli Q water, and 0.2 ml aqueous sodium citrate dyhydrate (0.17 M, 99 percent Sigma-Aldrich) were added after full dissolution of PVP. The mixture was thoroughly mixed and bubbles were removed. Finally, 0.3 ml of Tetraethyl orthosilicate (TEOS, 98 percent Sigma-Aldrich) was applied to the reaction mixture, gently shaken, and allowed to proceed for 24 hours. After centrifuging and fractionating the mixture, colloids were obtained with the desired aspect ratio. We prepared silica rods of average length (l) and diameter (d),  $l=3 \mu m$  and d=200 nm, respectively (designated as nano-rods). We also synthesized longer and thicker rods of length and diameter; l=6.5  $\mu$ m and  $d = 0.75 \mu$ m, respectively (designated as micro-rods). It is observed from the image that, one end of the nano-rods is flat and the other end is hemispherical (see Fig. 3.1). These colloids were treated with octadecyldimethyl-3-trimethoxysilylpropylammonium chloride (DMOAP) to obtain homeotropic surface anchoring of liquid crystal molecules. We used 5CB (4-n-pentyl-4-cyanobiphenyl) liquid crystal to disperse

the particles. The colloidal mixture was then dispersed in a planar cell (see Fig. 2.1). The position and orientation of the nano and micro-rods were tracked by using appropriate software. The electric field experiment is performed using a function generator (Tektronix-AFG 3102) and a voltage amplifier (TEGAM-2350).

# 3.3 Results and discussion

Our study begins with the observation of orientation of DMOAP coated silica nanorods dispersed in a planar cell of 5CB liquid crystal. The length to diameter aspect ratio (l/d) of these nano-rods is about 15. Figure 3.2(a) shows a representative CCD image of a few dispersed nano-rods and it is observed that the nano-rods are oriented either parallel or perpendicular to the nematic director  $(\hat{n})$ . Figure 3.2(c,d) shows POM images with cross polarizers and an additional  $\lambda$ -plate, respectively. Owing to strong elastic distortion, the parallel nano-rods are clearly visible, while the perpendicular nano-rods are blurred. The yellowish and bluish colours around the parallel nano-rod in Fig. 3.2(d) represents anticlockwise and clockwise rotation of the nematic director, respectively. In the case of parallel orientation (Fig. 3.2(e)), the point defect is located within the nano-rod, whereas the ring defect along the perpendicular nano-rod (Fig. 3.2(f)) is highly pinned on the surface and thus unresolvable. The cross section of a perpendicular nano-rod in the inset of Fig. 3.2(f) shows that the elastic distortion is very weak.

To find the size effect, we studied the orientation of silica rods with larger length and diameter than the nano-rods. They are designated here as micro-rods, having average length and diameter of about 6.5  $\mu$ m and 0.75  $\mu$ m, respectively. Their aspect ratio is:  $l/d \approx 9$ , which is almost half the value of the nano-rods. A CCD image of a few DMOAP coated micro-rods dispersed in 5CB liquid crystal is shown in Figure 3.3(a). The majority of the micro-rods are oriented parallel to the director, while a small percentage is oriented randomly in all other directions (Fig. 3.3(b)). This is in contrast to the orientation of the nano-rods shown in Fig. 3.2(b).

We looked at the induced defects by the micro-rods in a planar aligned nematic cell. The particle's one end is flat end and other end is hemispherical [15]. Micro-rods

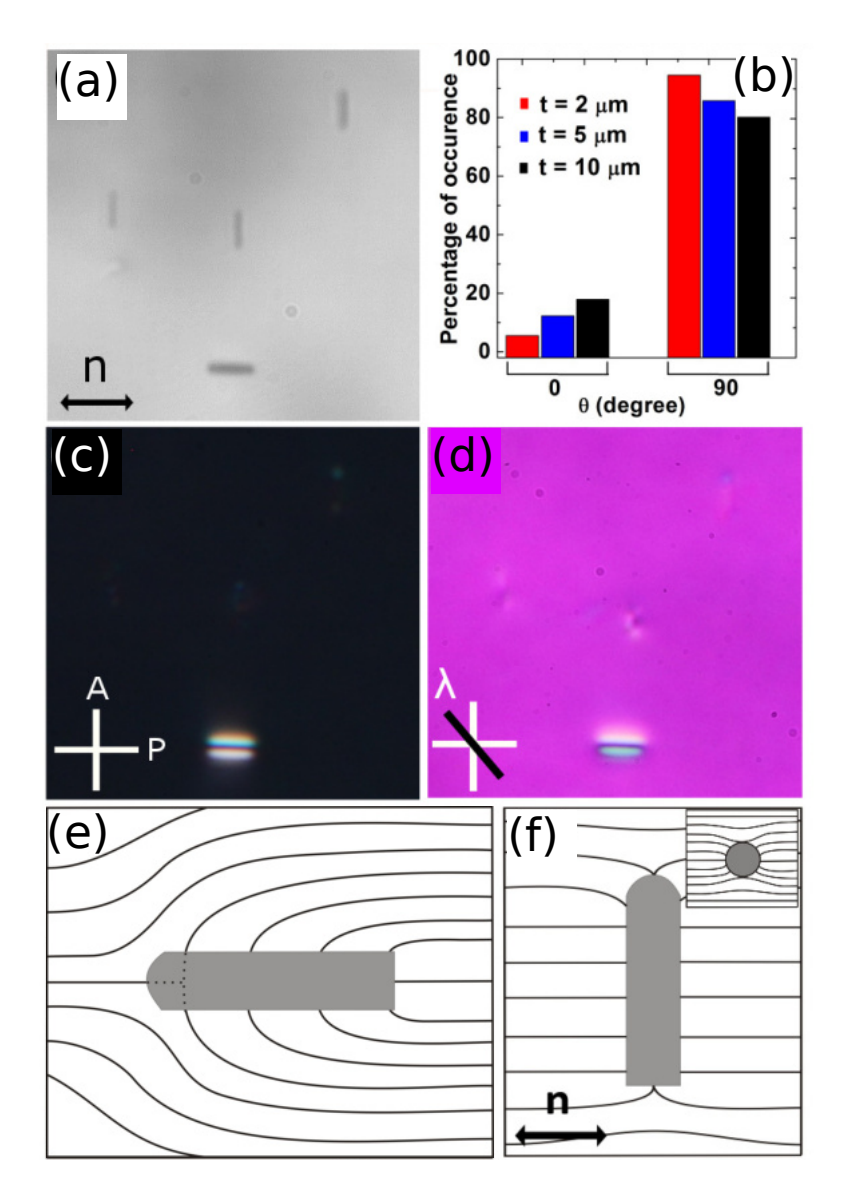


Figure 3.2: (a) CCD image of a few DMOAP coated silica nano-rods dispersed in a planar cell of 5CB liquid crystal, (b) Statistical analysis of orientation of the nano-rods with respect to the nematic director. Different colours correspond to different cell thicknesses namely, 2, 5 and 10  $\mu$ m respectively. Polarizing optical microscopy (POM) images with, (c) crossed polarizers, (d) an additional  $\lambda$ -plate (530 nm) with slow axis oriented as shown, inserted between the polarizers and sample. Schematic representation of director distortions surrounding a nano-rod oriented, (e) parallel to the director, and (f) perpendicular to the director. (Inset) Cross-section of director distortion. Double headed arrow below  $\hat{n}$  denotes the director. White cross denotes the polarizer and analyzer.

with homeotropic surface anchoring form elastic dipoles with a point defect near the curved end that are aligned along the director (Fig. 3.3(c)). Figure 3.3(d) shows a point defect associated with a micro-rod, schematically. We get elastic dipoles for the micro-rod system, but the point defects appear to form either on flat or curved ends, suggesting the impact of edge asymmetry is minimal. We compare the spontaneous orientation of the micro- and nano-rods with respect to the director. It is found that the nano-rods have two distinct orientations with majority (more than 80%) of them are perpendicular to the director and the percentage of occurrence weakly depends on the cell thickness (Fig. 3.2(b)). On the other hand, nearly 50% of the micro-rods are oriented parallel to the director, and remaining 50% shows a wide variation of the orientation angle (Fig. 3.3(b)). For the nano-rods, the point defects are formed within the particles (virtual defect) whereas for the micro-rods, the point defects are formed near the particles. The overall orientation and the elastic deformation of our micro-rods are somewhat identical to that of the glass micro-rods studied by Tkalec et al [9].

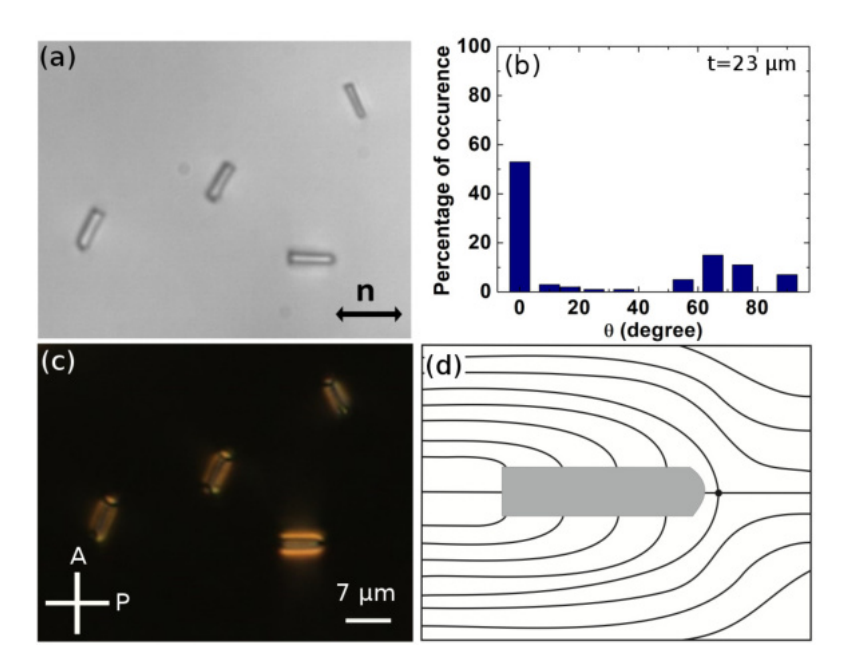


Figure 3.3: Polarizing optical microscope (POM) images of silica micro-rods of average length 6.5  $\mu$ m and diameter 0.75  $\mu$ m dispersed in a planar cell of 5CB, (a) without crossed polarizers, (c) with crossed polarizers. (b) Distribution of orientation angle with respect to the nematic director. (d) Schematic representation of director distortions surrounding a micro-rod oriented parallel to the director. t is the cell thickness.

Following Burylov et al., the difference in the orientation behaviour of the silica nano and micro-rods can be understood based on a dimensionless parameter [16, 17]. Assuming negligibly small contribution of the edges, the elastic and the surface energy of the silica rods can be written as  $E_{el} \approx LK$ , and  $E_{sur} \approx RLW$ , where L is the length of the rod, R the radius, K is the average elastic constant and W is the surface anchoring energy coefficient. The ratio of the elastic and surface energies gives a dimensionless parameter, p = WR/K. If p > 1, the silica rods are oriented parallel and if p < 1, they are oriented perpendicular to the director. For a given W, the orientation of the silica rod is primarily determined by its radius and  $p \propto R$ . Since the diameter of the nano-rods is nearly 4 times smaller than that of the micro-rods, p could be less than one and the majority of nano-rods can have perpendicular orientation.

This can be understood following a simple calculation [18]. We consider a colloidal rod with a cylindrical symmetry axis  $\hat{\omega}$  immersed in a planar nematic cell. In the limit of weak surface anchoring boundary conditions, the equilibrium orientation of such a nano-rod corresponds to a minimum of the surface anchoring energy describing anisotropic molecular interactions at the rod's surface. The surface anchoring energy density per area is written as [19],

$$W = (W_0/2)sin^2\psi (3.1)$$

where  $W_0$  is the surface anchoring coefficient and  $\psi$  is the angle between the nematic director and the easy axis for the director orientation on the rod. From geometric considerations, we express  $\psi$  in terms of the polar and azimuthal angles as  $\cos \psi = \cos \varphi \sin \theta$ . This gives the free energy density:

$$W = W_0(1 - \cos^2 \psi)/2 = W_0(1 - \cos^2 \varphi \sin^2 \theta)/2$$
(3.2)

By neglecting the end faces of the rods due to their high l/d ratios, the total anchoring surface energy per rod can be expressed as [18],

$$F = \int_{\Omega} W d\Omega = \int_{0}^{L} dl \int_{0}^{2\pi} (W_{0}/4)(1 - \cos^{2}\varphi \sin^{2}\theta) D d\varphi = (\pi L D W_{0})(1 + \cos^{2}\theta)/4$$
 (3.3)

where L is the length of the nano-rod, D is the diameter and  $\theta$  is the angle between the nematic director and the long axis of the nano-rod. It is observed from the equation

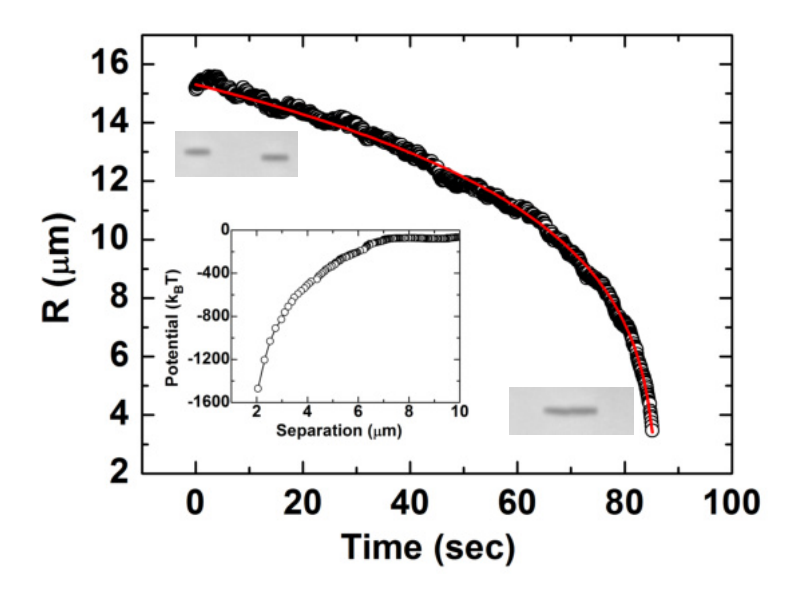


Figure 3.4: Time dependent centre to centre separation (R) between a pair of collinear nano-rods parallel to the director. Red line shows the nonlinear least square fit to  $R(t) = (R_0^5 - 5\alpha t)^{1/5}$  with  $\alpha = 7.3 \times 10^{-3} \ \mu m^5/sec$  corresponding to dipolar interaction. Inset shows the interaction potential as a function of separation.

that, F is minimised when the nano-rods are perpendicular to the director i.e.,  $\theta = \pm \pi/2$ , which is consistent with our experiments.

In what follows, we study elastic pair interaction of nano-rods oriented both parallel and perpendicular to the director. Figure 3.4 presents a pair of interacting nano-rods oriented parallel to the nematic director. With the help of laser tweezers, two nano-rods were kept apart at a certain distance and allowed to interact freely. The centre-to-centre separation (R) was measured as a function of time. The time dependent separation corresponding to dipolar interaction is fitted to the equation  $R(t) = (R_0^5 - 5\alpha t)^{1/5}$ , where  $\alpha = k/\zeta$ ,  $\zeta$  being the drag coefficient and  $R_0$  is the separation at t = 0 s (see Eq. (1.28) in chapter-1). This suggests that the interaction is dipolar type and the corresponding variation of potential energy is shown in the inset of Fig. 3.4. We also studied the interaction of two nano-rods approaching at different angles with respect to the director as shown in Fig. 3.5. The attractive and repulsive interactions of nano-rods are represented by the colour coded trajectories. When two rods have similar

elastic distortions (both have same colour layout on top and bottom) they attracts each other within a narrow angle of about  $\pm 15^{\circ}$ , and repel at all other angles (Fig. 3.5(a)). In this case two elastic dipoles are parallel (see Fig. 1.13(a) in chapter-1). When they have opposite elastic deformation (opposite layout of colour with respect to the previous pair), the interaction is repulsive for collinear pair and attractive for all other angles (Fig. 3.5(b)). In this case the elastic dipoles are oriented antiparallel.

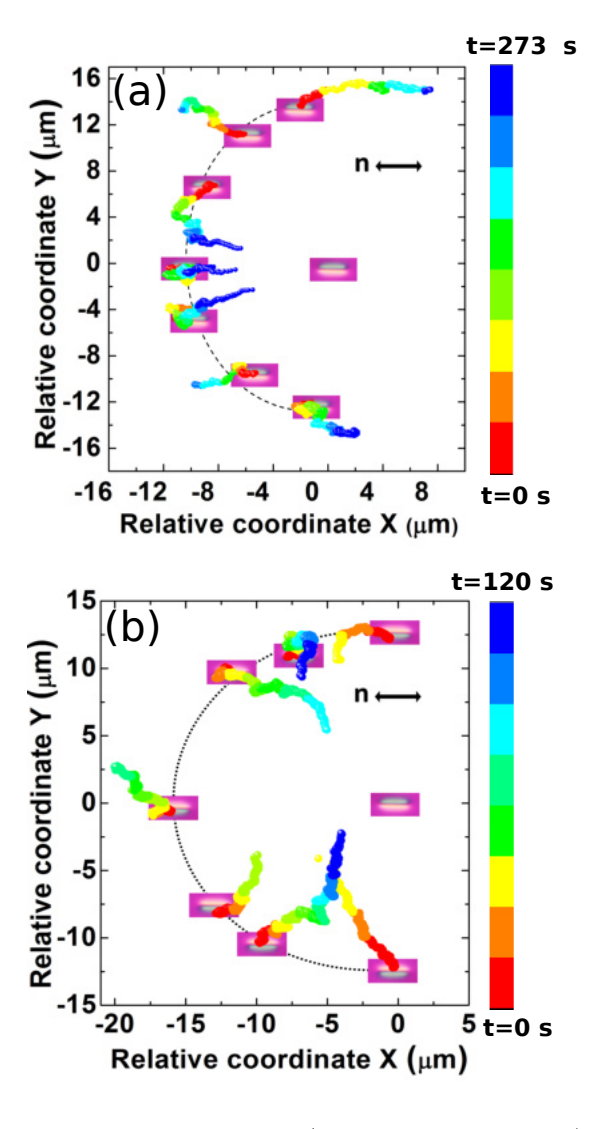


Figure 3.5: Colour coded time trajectories (Relative coordinate) of two nano-rods oriented parallel to the director and situated at different angles with respect to the director when both the nano-rods having, (a) similar director orientation, (b) opposite director orientation (see the yellow and blue colours of the  $\lambda$ -plate images in two cases). By "relative coordinate" we mean relative to the starting point of each trajectory.

We have further studied the elastic pair interaction of nano-rods, oriented orthogonal to the director. A few representative CCD images of two interacting nano-rods at different times are shown in Fig. 3.6(a). It is noted that due to the attractive interaction, one nano-rod goes vertically down, under the other particle (out-of-plane). The time dependence of interparticle separation is shown in Fig. 3.6(b)) and it can be fitted to the equation  $R(t)=(R_0^7-7\alpha t)^{1/7}$ , which suggests that the interaction is quadrupolar [20]. The variation of interaction potential is also shown in the inset. The angle dependence of the interaction is studied by allowing two nano-rods to interacts from different angles as described previously. The relative coordinates of two interacting nano-rods demonstrate that the attractive interaction is short-ranged compared to nano-rod oriented parallel to the director and does not depend on the approaching angle as shown in Fig. 3.6(c). By assembling 14 nano-rods, a vertical ribbon structure is created and shown in Fig. 3.6(d). The structure was tilted by dragging it using the laser tweezers to visualise the ribbon and to check its stability. When the laser is switched off, the ribbon is finally relaxed to the initial configuration.

We construct a variety of stable and linear colloidal structures employing the nanorods. Figure 3.7(a,b) shows a linear chain of nano-rods assembled together along the nematic director and it appears like a continuous string. The linear chain of nano-rods is akin to a linear homopolymer, with each nano-rod resembles a monomer. Figure 3.7(c) shows a schematic director orientation surrounding the chain. Similarly 10 nano-rods were assembled side by side to form a ribbon-like structure, as illustrated in Fig. 3.7(d,e). A schematic director distortion surrounding the ribbon is also shown in Fig. 3.7(f).

To construct co-assembled structures we used DMOAP coated silica microspheres and nano-rods. A dipolar microsphere with a diameter of 1  $\mu$ m and a dipolar nano-rod parallel to the nematic director experience attractive interaction and forms a match-stick like object (Fig. 3.8(a-c)). This also helps to understand in which side of the nano-rod the point defect resides. The  $\lambda$ -plate image ((Fig. 3.8(b)) shows that the point defect is located near the right side of the nano-rod. When a quadrupolar microsphere is brought closer to a nano-rod, the Saturn ring defect of the microsphere becomes unstable when the two particles approach each other, and eventually the

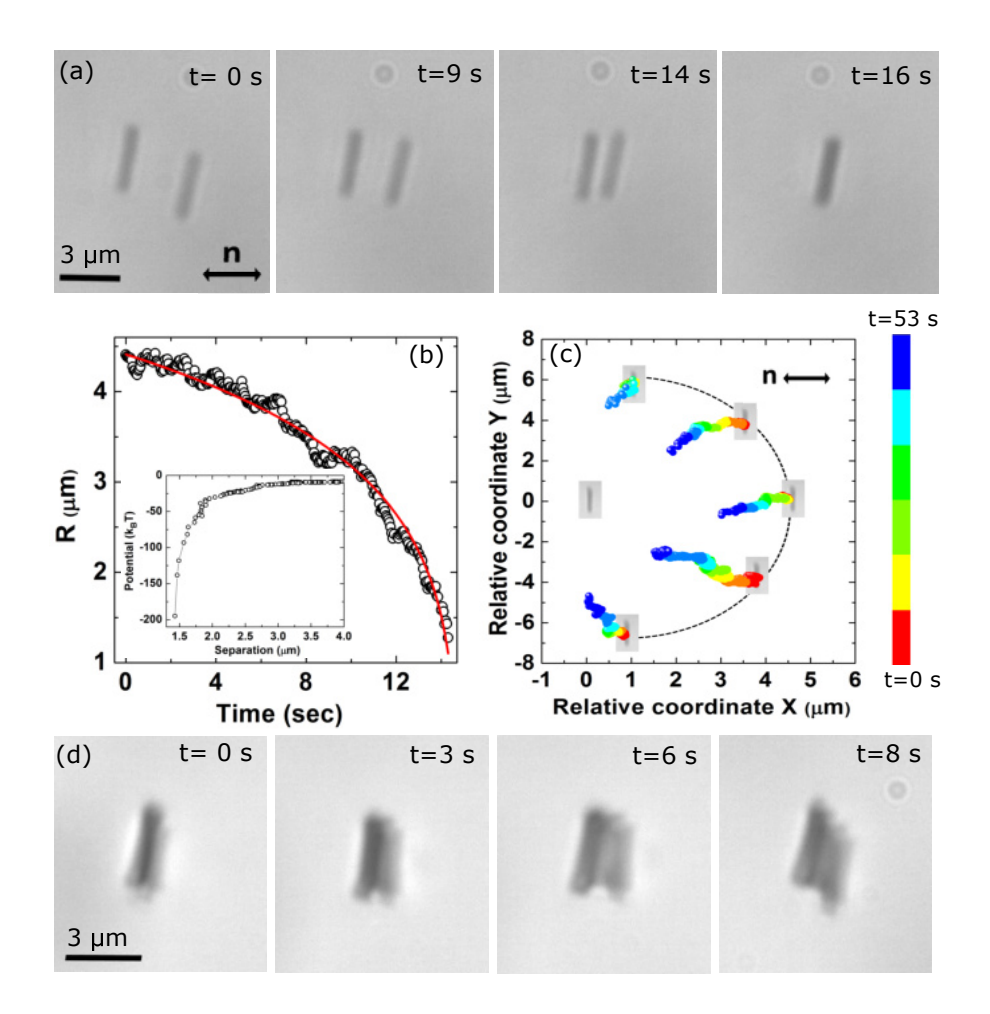


Figure 3.6: (a) Sequence of CCD images of a pair of interacting nano-rods oriented perpendicular to the director. Nano-rods are attracted towards each other and one nano-rod goes below the other. (b) Time dependent centre to centre separation (R) of a pair of nano-rods. The red line shows nonlinear least square fit to  $R(t) = (R_0^7 - 7\alpha t)^{1/7}$  with  $\alpha = 2.4 \times 10^4 \ \mu m^7/\text{sec}$  corresponding to quadrupolar interaction. Inset shows the variation of interaction potential with separation. (c) Colour coded time trajectory (Relative coordinate) of two nano-rods approaching each other at different angles with respect to the director. (d) Vertical ribbon-like structure made of 14 nano-rods and temporal evolution of the structure when a gentle force was applied with the help of the optical tweezers.

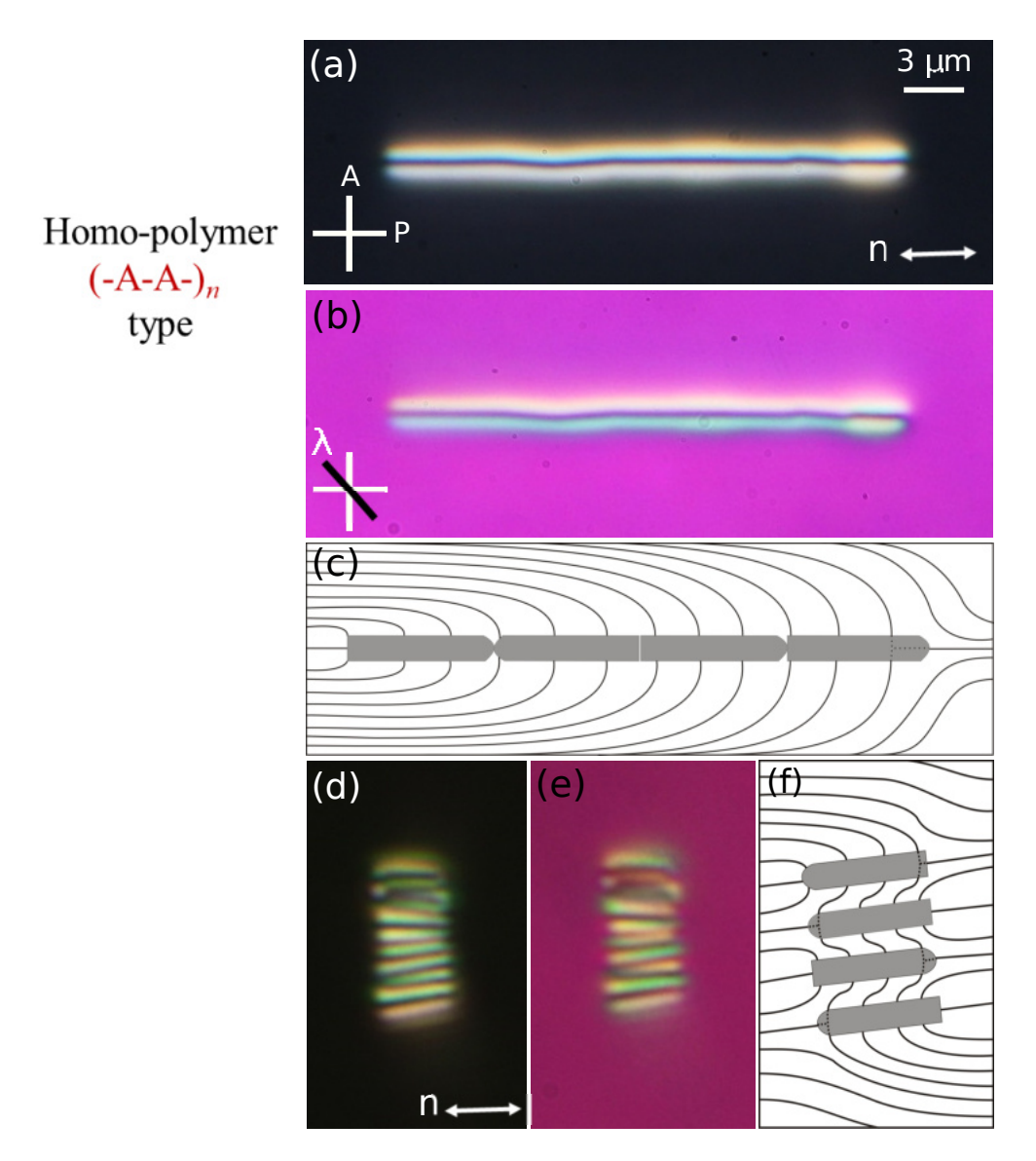


Figure 3.7: POM images of a 1-D linear chain of 10 nano-rods assembled along the nematic director. Images are taken with, (a) crossed polarizers, (b) an additional  $\lambda$ -plate. (c) Schematic representation of the director field surrounding the chain. (d,e) POM and  $\lambda$ -plate images of a ribbon-like structure assembled in the perpendicular direction of the director. (f) Schematic director orientation surrounding the ribbon.

quadrupolar microsphere is transformed in to a dipolar microsphere. CCD snapshots taken at different times of a microsphere (diameter 2.3  $\mu$ m) interacting with a nano-rod are shown in Fig. 3.8(d). Experiments with varying microsphere diameters revealed that beyond about 3.5  $\mu$ m diameter, the quadrupolar structure is stable and no dipolar transformation is observed (Fig. 3.8(e–g)). Here two nano-rods from the opposite directions were allowed to interact in the equatorial plane of a spherical particle of diameter 5.2  $\mu$ m. The interaction is attractive and the assembly as a whole looks like a snake charmer's flute. If they approach from any other plane then they are attracted to the Saturn ring similar to the response of spherical nanoparticles.

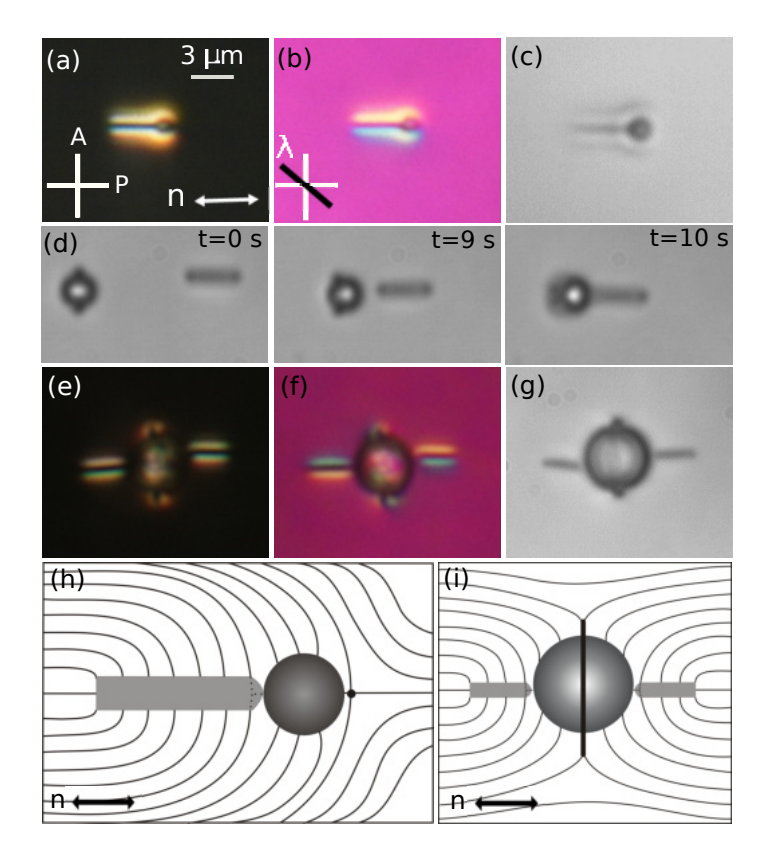


Figure 3.8: Match-stick like shape formed by a dipolar spherical colloid of diameter 1.1  $\mu$ m and a nano-rod. POM images with, (a) cross polarizers, (b) an additional  $\lambda$ -plate, and (c) without polarizers. (h) Schematic representation of director deformation surrounding the assembly of the nano-rod and microsphere. (d) Temporal evolution of conversion of a spherical quadrupolar colloid of diameter 2.3  $\mu$ m into dipolar one when the nano-rod and the microsphere are approaching each other. (e–g) Assembly of a quadrupolar colloid of diameter 5.2  $\mu$ m and two nano-rods oriented opposite sides and (i) schematic director deformation.

Using different combinations of nano-rods, micro-rods and microsphere, we made several linear chains as shown in Fig. 3.9. Figure 3.9(a) shows the optical photomicrograph of a linear chain of several dipolar sphere (diameter 5.2  $\mu m$ ) and nano-rods (diameter 200 nm). The binding energy for such pair interaction is approximately  $4000 \text{ k}_B \text{T}$ . As the induced defects of the nano-rods reside in the rod (near the edge), the surface to surface separation between the two microspheres is nearly equal to the length of the nano-rods. Similarly, we have designed linear chains of alternative micro and nano-rods (Fig. 3.9(e,f)) and micro-rods, followed by nano-rods and microsphere (Fig. 3.9(c,d)). The binding energy for nano and micro-rod interaction is around 3000  $k_BT$ . We also prepared a linear chain of quadrupolar microspheres and nano-rods. In this case, the chain is orientated perpendicular to the director (Fig. 3.9 (g.h)). The pair interaction has a binding energy of approximately 1500  $k_BT$ , which is lower than the previous two cases. These self assembled structures are similar to linear co-polymer chains. The structure shown in Fig. 3.9(a,e) can be thought of as a linear co-polymer of the  $(-A-B-)_n$  type, as they are made of two different types of particles. Similarly, the structure shown in Fig. 3.9(c) can be considered as a co-polymer of  $(-A-B-C-B-)_n$ type. Also the linear chain shown in Fig. 3.7(a) is analogous to a homo-polymer of  $(-A-A-)_n$  type. The polymeric structures are highly stable and reconfigurable by the optical tweezers.

The robustness of the colloidal polymers is tested by applying an ac electric field. An out-of-plane field is applied perpendicular to the linear chain and nematic director. As shown in Fig. 3.10, with the increased electric field, the chain tends to orientate towards the direction of the field. The structure can regain its original state without any structural deformation.

Finally, the colloidal co-polymer chains are assembled using laser tweezers to create a two-dimensional binary crystal. Figure 3.11 shows a two-dimensional binary colloidal crystal assembled in a planar cell from (-A-B-)<sub>n</sub> type chains of microspheres and nanorods. We used 60 dipolar micro spheres and 50 nano-rods to construct the structure and it is found to be highly stable. Thus a stable 2D oblique lattice is formed as a result of long-range elastic interaction. The lattice unit of 2D binary crystal is generally a parallelogram with average lattice parameters,  $a \simeq 7.2 \ \mu\text{m}$ ,  $b \simeq 3.9 \ \mu\text{m}$  and  $\gamma \simeq 48^{\circ}$ .

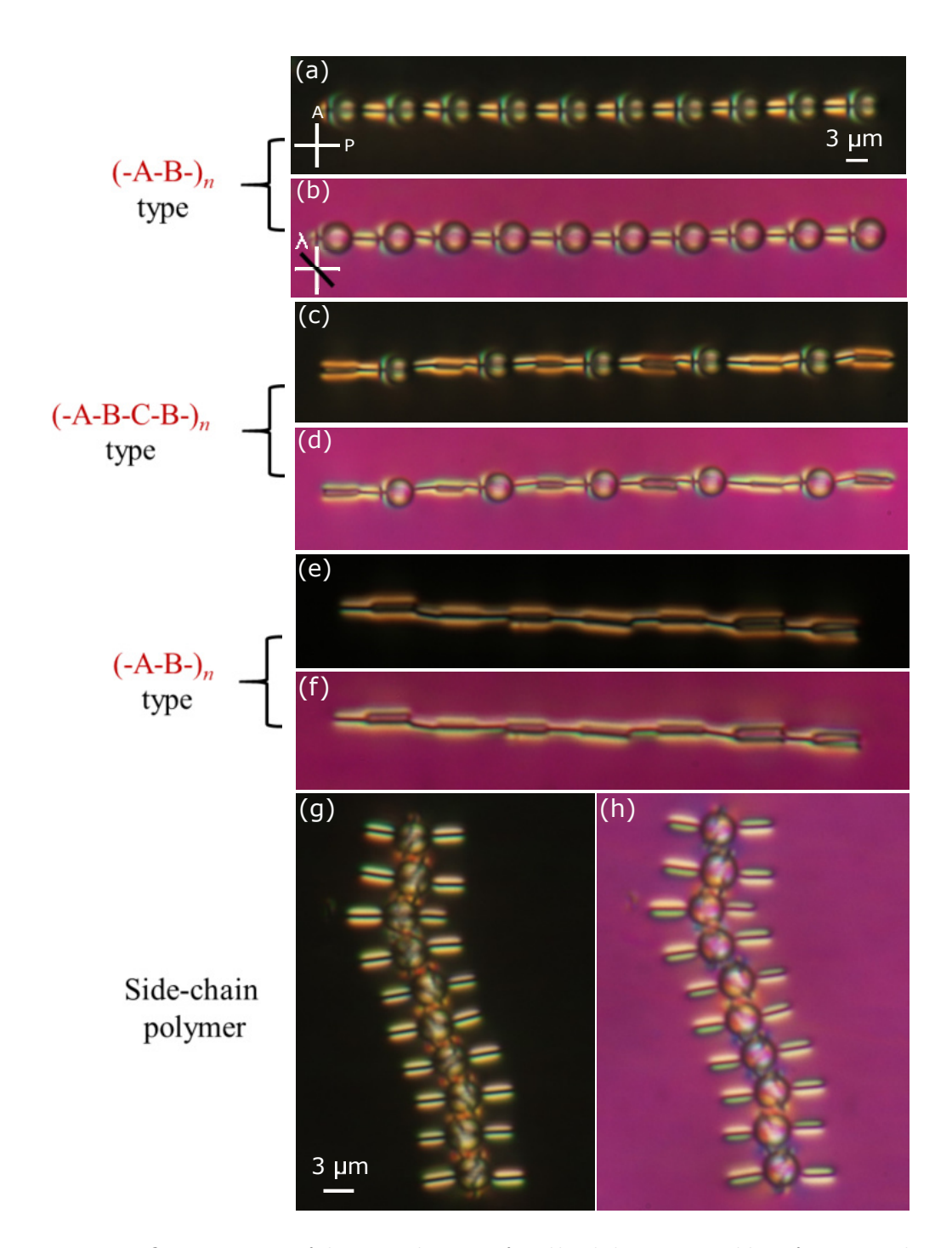


Figure 3.9: POM images of linear chains of colloidal co-assembly of microspheres, micro-rods and nano-rods. Images are taken with (a,c,e,g) crossed polarizers and (b,d,f,h) an additional  $\lambda$ -plate inserted in between sample and analyzer. The diameter of the microsphere is 5.2  $\mu$ m.

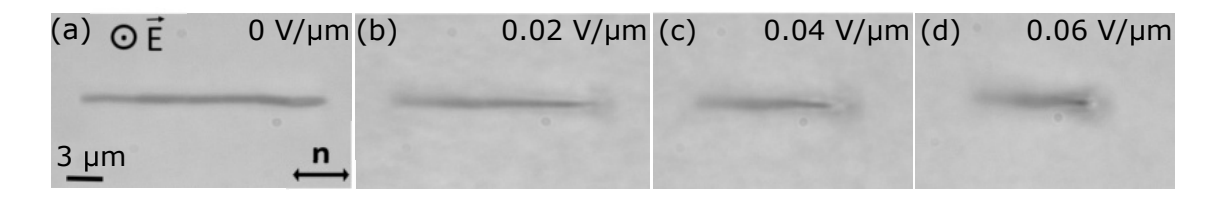


Figure 3.10: CCD images of a linear chain of 7 nano-rods in a planar cell showing the effect of ac electric field. Frequency applied is 20 kHz and cell thickness is 50  $\mu$ m.

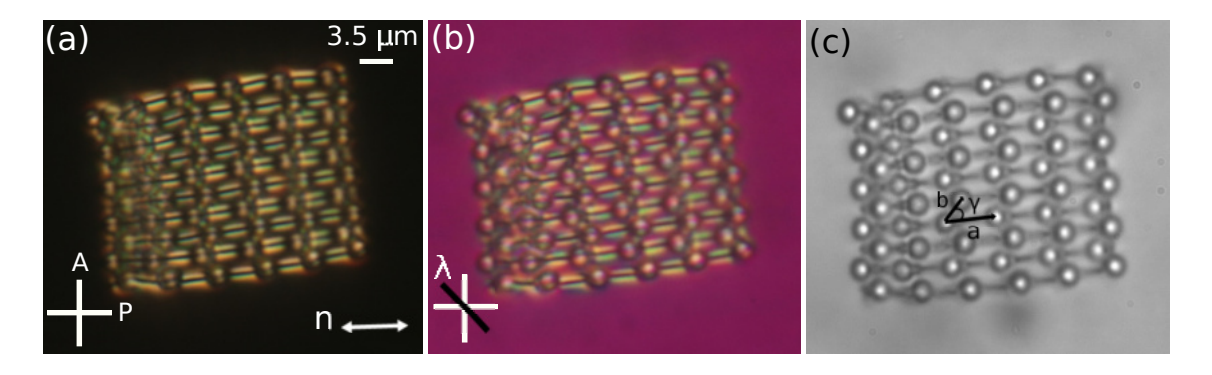


Figure 3.11: Optical photomicrographs of a 2D crystal of binary colloids. POM images taken, (a) with crossed polarizers, (b) with a  $\lambda$ -plate and (c) without crossed polarizers. Oblique lattice with parameters;  $a \simeq 7.2 \ \mu m$ ,  $b \simeq 3.9 \ \mu m$  and  $\gamma \simeq 48^{-0}$ .

More complex colloidal structures can be created by designing appropriate polymers as the base unit.

# 3.4 Conclusion

We studied the orientation, interaction and assembly of silica nano-rods of high aspect ratio in a nematic liquid crystal. The nano-rods exhibit only two specific orientations namely, the parallel or perpendicular with respect to the nematic director. Majority of the nano-rods are oriented perpendicular to the director field. The defects induced on the nano-rods are virtual and unresolvable under optical polarizing microscope. Microrods, on the other hand, exhibit all possible orientations with half of them oriented parallel to the nematic director. They exhibit either elastic dipolar or quadrupolar defects. In contrast to the in-plane anisotropic interaction of nano-rods oriented parallel to the director, nano-rods oriented perpendicular to the nematic director experience

#### 3.4. References

out-of-plane isotropic attractive interaction. In the presence of nano-rods, smaller spherical quadrupolar particles become unstable and transform into dipolar particles. Various types of colloidal particles are chosen for designing colloidal chains similar to the linear co-polymers, such as  $(-A-B-)_n$ ,  $(-A-B-C-B-)_n$ , homo-polymer  $(-A-A-)_n$ , horizontal and vertical ribbons, 2D binary crystals etc. Polymeric structures are robust as they can be oriented along the applied electric field and regain its original state without any permanent deformation when the field is off. Out-of-plane orthogonal orientation of the nano-rods with respect to the director is potential for making hybrid molecular-colloidal liquid crystal systems. The spontaneous vertical assembly of the nano-rods may provide a novel and versatile path toward building blocks for hierarchical materials assembly.

# References

- [1] U. M. Ognysta, A. B. Nych, V. A. Uzunova, V. M. Pergamenschik and V. G. Nazarenko, Square colloidal lattices and pair interaction in a binary system of quadrupolar nematic colloids. Phys. Rev. E, vol. 83, pp. 041709, 2011.
- [2] A. Nych, U. Ognysta, M. Škarabot, M. Ravnik, S. Žumer and I. Muševič, Assembly and control of 3D nematic dipolar colloidal crystals. Nat. Commun., vol. 4, pp. 1489, 2013.
- [3] S. Park, Q. Liu and I. I. Smalyukh, Colloidal surfaces with boundaries, apex boojums, and nested elastic self-assembly of nematic colloids. Phys. Rev. Lett., vol. 117, pp. 277801, 2016.
- [4] C. P. Lapointe, T. G. Mason and I. I. Smalyukh, *Shape-controlled colloidal interactions in nematic liquid crystals*. Science, vol. 326, pp. 1083-1086, 2009.
- [5] A. T. Juhl et al., Ordering of glass rods in nematic and cholesteric liquid crystals.Opt. Exp. Mat., vol. 1, pp. 1536-1547, 2011.
- [6] A. Eremin et al., Optically driven translational and rotational motions of microrod particles in a nematic liquid crystal. Proc. Natl. Acad. Sci., vol. 112, pp. 1716-1720, 2015.
- [7] C. Lapointe et al., Elastic torque and the levitation of metal wires by a nematic liquid crystal. Science, vol. 303, pp. 652-655, 2004.
- [8] B. Senyuk et al., Shape-dependent oriented trapping and scaffolding of plasmonic nanoparticles by topological defects for self-assembly of colloidal dimers in liquid crystals. Nano Lett., vol. 12, pp. 955-963, 2012.

- [9] U. Tkalec, M. Škarabot and I. Muševič, Interactions of micro-rods in a thin layer of a nematic liquid crystal. Soft Matter, vol. 4, pp. 2402-2409, 2008.
- [10] A. Groschel et al., Guided hierarchical co-assembly of soft patchy nanoparticles. Nature, vol. 503, pp. 247-251, 2013.
- [11] C. P. Lapointe, K. Mayoral and T. G. Mason, Star colloids in nematic liquid crystals. Soft Matter, vol. 9, pp. 7843-7854, 2013.
- [12] D. V. Sudhakaran, R. K. Pujala and S Dhara, Orientation dependent interaction and self-assembly of cubic magnetic colloids in a nematic liquid crystal. Adv. Opt. Mater., vol. 8, pp. 1901585, 2020.
- [13] D. K. Sahu, S. Kole, S. Ramaswamy and S. Dhara, Omnidirectional transport and navigation of Janus particles through a nematic liquid crystal film. Phys. Rev. Research, vol. 2, pp. 032009(R), 2020.
- [14] A. Kuijk, A. van Blaaderen and A. Imhof, Synthesis of monodisperse, rodlike silica colloids with tunable aspect ratio. J. Am. Chem. Soc., vol. 133, pp. 2346-2349, 2011.
- [15] M. A. Gharbi et al., Microbullet assembly: interactions of oriented dipoles in confined nematic liquid crystal. Liq. Cryst., vol. 40, pp. 1619-1627, 2013.
- [16] S. V. Burylov and Y. L. Raikher, Orientation of a solid particle embedded in a monodomain nematic liquid crystal. Phys. Rev. E, vol. 50, pp. 358, 1994.
- [17] M. D. Lynch and D. L. Patrick, Controlling the orientation of micron-sized rodshaped SiC particles with nematic liquid crystal solvents. Chem. Mater., vol. 16, pp. 762-767, 2004.
- [18] H. Mundoor, S. Park, B. Senyuk, H. H. Wensink and I. I. Smalyukh, Hybrid molecular-colloidal liquid crystals. Science, vol. 360, pp. 768-771, 2018.
- [19] P. G. de Gennes and J. Prost, The physics of liquid crystals. 2nd Ed, Clarendon Press, Oxford, 1993.

#### References

[20] M. V. Rasna et al., Orientation, interaction and laser assisted self-assembly of organic single-crystal micro-sheets in a nematic liquid crystal. Soft Matter, vol. 11, pp. 7674-7679, 2015.

4

# Interactions of silica micro-rods in chiral nematic liquid crystals

# 4.1 Introduction

**▼**n the preceding chapter, we investigated the spontaneous orientation, elastic interlacktriangle action, and directed self-assembly of nano and micro-rods dispersed in a nematic LC. When the dispersing medium is a twisted nematic or chiral nematic, the director twists in space, and the spherical microparticles exhibit a number of interesting defect structures wherein a single defect loop wraps around the microsphere, with the winding layout being more complex in cells with a higher twist. The interaction of such defect loop decorated microspheres often leads to metastable and reconfigurable states due to the screening of elastic interaction by the periodic structure of the chiral nematics [1]. The nontrivial shapes of the particles also greatly influence the elastic distortion and the ensuing interaction. In chiral nematics, the defects and elastic interaction of anisotropic particles are obviously going to be more complex and such studies are largely unexplored. Apart from the elastic interaction, electrostatic (for charged particles) and hydrodynamic interaction of microparticles in liquid crystals play an important role in their assembly. Recently some interesting aspects of electrostatic interaction of particles in nematic LCs have been experimentally demonstrated [2,3]. Theoretically, hydrodynamic effects in LC colloids have been studied [4–6] but not directly explored experimentally. The hydrodynamic interaction has been studied in aqueous colloidal systems by optically trapping two Brownian particles using laser tweezers [7,8]. However, the particles in LCs cannot be directly trapped by laser

tweezers in the conventional ways [9], thus making the direct measurement of hydrodynamic interaction problematic.

In this chapter, we present experimental results on silica micro-rods with homeotropic anchoring conditions in chiral NLCs. We show that a pair of micro-rods are self-trapped for a specific orientation due to the competing effect of electrostatic and elastic pair interaction, resulting in a bound state in which they are separated by a certain distance. One of the interesting finding of our experiments is that, two micro-rods interact through hydrodynamic forces in the bound state. Our experiments reveal unexplored aspects of liquid-crystal dispersions which are important for understanding the assembly and dynamics of nano and microparticles in chiral nematic liquid crystals.

# 4.2 Experimental

The synthesis of silica micro-rods is carried out using a wet chemical method following the procedure described in the previous chapter. The average length and diameter of the micro-rods are 6  $\mu$ m and 800 nm, respectively. They were coated with DMOAP for obtaining homeotropic anchoring of the director  $\hat{n}$ .

The chiral NLCs were prepared by doping a chiral agent called 4 - cyano - 40 - (2-methylbutyl)- biphenylene (CB15) in 4-n-pentyl-4-cyanobiphenyl (5CB) nematic liquid crystal. The concentration of CB15 was adjusted to vary the helical pitch, which was measured using a wedge cell. We use Grandjean-Cano wedge method to calculate the pitch of a chiral NLC cell, as shown in Fig. 4.1(a). A pair of glass plates are assembled to form a wedge cell with an opening angle ( $\alpha$ ). The value of the pitch can be calculated as [10]

$$p = 2L\alpha \tag{4.1}$$

where  $\alpha = (t_2 - t_1)/T$ . Here L is the distance between the disclination lines. Figure 4.1(b) shows the polarizing optical microscope image with disclination lines of the sample studied.

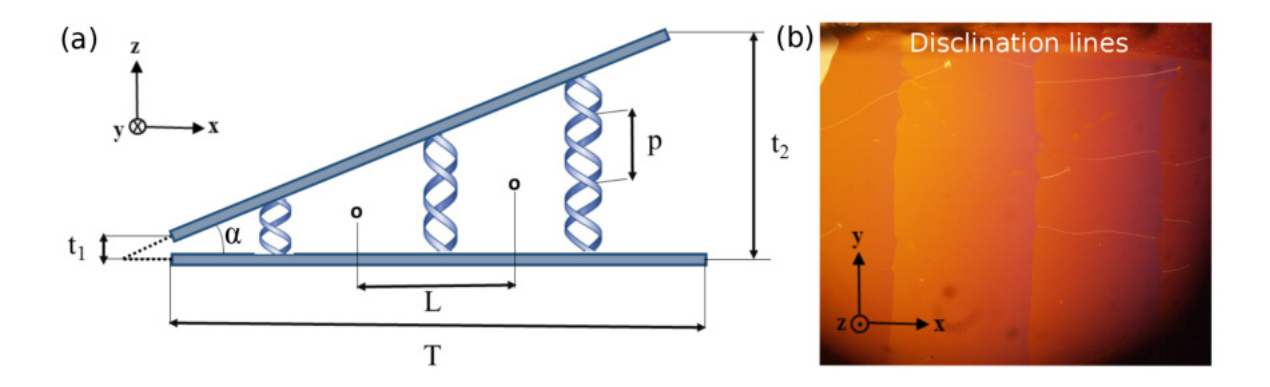


Figure 4.1: (a) Schematic representation of Cano wedge cell. (b) Grandjean-Cano wedge lines in a wedge cell. Vertical lines are the disclination lines.

The micro-rod-chiral NLC dispersions were studied in planar cells. The helix axis of the chiral mixture is perpendicular to the plane of the substrate, as illustrated in Fig. 4.3(b). The pitch of the sample was adjusted in a cell gap of d such that the nematic director is twisted by multiples of half-pitch i.e., d = N(p/2), which is denoted here as  $N\pi$  twisted cell (Fig. 4.3(b)). We used  $d = 4 \mu m$  and  $p = 8 \mu m$  for  $\pi$ -twisted and  $d = 5 \mu m$  and  $p = 5 \mu m$  for  $2\pi$ -twisted cells. The centers of the micro-rods were tracked by using video microscopy technique with a resolution of  $\pm 20$  nm. The autocorrelation and cross-correlation functions of the position fluctuations of the micro-rods were calculated using the Mathematica program.

### 4.3 Results and discussion

The chirality creates complexity in the achiral nematic director by creating helical rotation. When spherical particles are dispersed in chiral NLCs, disclination loops of 1/2 defects are observed in the helix direction around the particle's surface (see section 1.5.5). It has been reported that the spherical microparticles in chiral NLCs exhibit metastable states due to the screening of chiral interaction in which two micro-spheres are temporarily held at a certain separation for a short duration and eventually they are attracted and joined together [1]. We performed some preliminary experiments on spherical microparticles and demonstrated the formation of metastable state in  $\pi$  and

 $2\pi$ -twisted cells. Figure 4.2 shows a metastable state in which the particle surface-to-surface separation remains nearly constant for some time. The duration of metastable state in  $2\pi$ -twisted cell is roughly 260 seconds, while the duration in  $\pi$ -twisted cell is substantially less (38 s).

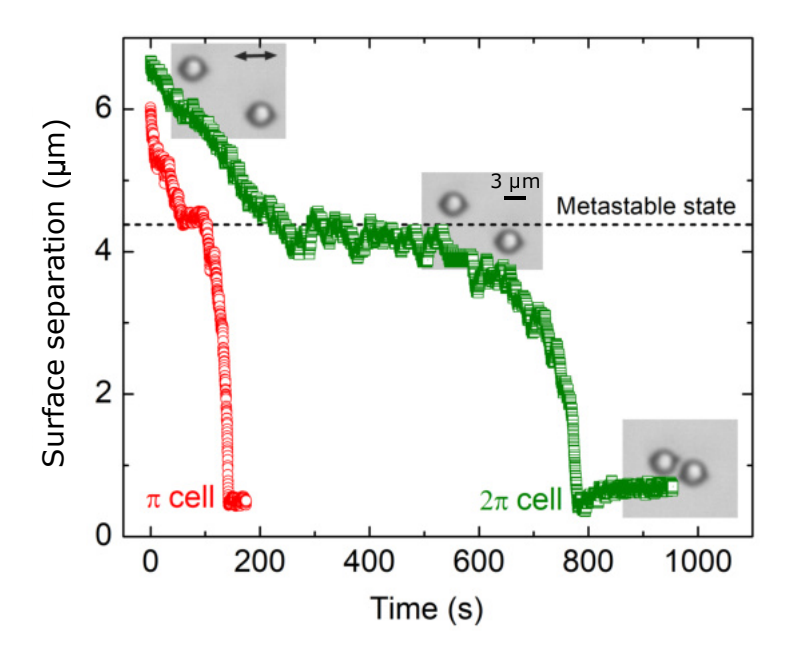


Figure 4.2: Surface-to-surface separation of two DMOAP coated silica microspheres of diameter 3  $\mu$ m in  $\pi$  (red circles) and  $2\pi$ -twisted (green squares) cells. The ratios of the diameter to pitch are D/p = 1/2 and 1 for  $\pi$  and  $2\pi$ -twisted cells, respectively. Note that eventually the particles are attracted to join.

In this chapter we work on micro-rods dispersed in chiral NLC. We work in the dilute concentration regime where most of the micro-rods are dispersed singly throughout the cell. To begin with, we study the LC-micro-rod dispersions in a  $2\pi$ -twisted cell and observe that majority of the micro-rods are orientated perpendicular to the rubbing direction (Fig. 4.3(c)). Although the surrounding elastic distortion of the micro-rod is clearly visible, the structure of the defect is unclear unlike the case of a microsphere dispersed in a planar, nonchiral nematic LC [1]. For a spherical particle, a single defect loop winds around it when the diameter (D) of the particle is comparable to the cell thickness and the twisting strength, D/p is integral multiple of 1/2 where p is the pitch of the chiral liquid crystal. For micro-rods in a  $2\pi$  twisted cell,  $D/p \simeq 0.16$  which is substantially less than 1/2 and they have dipolar configuration.

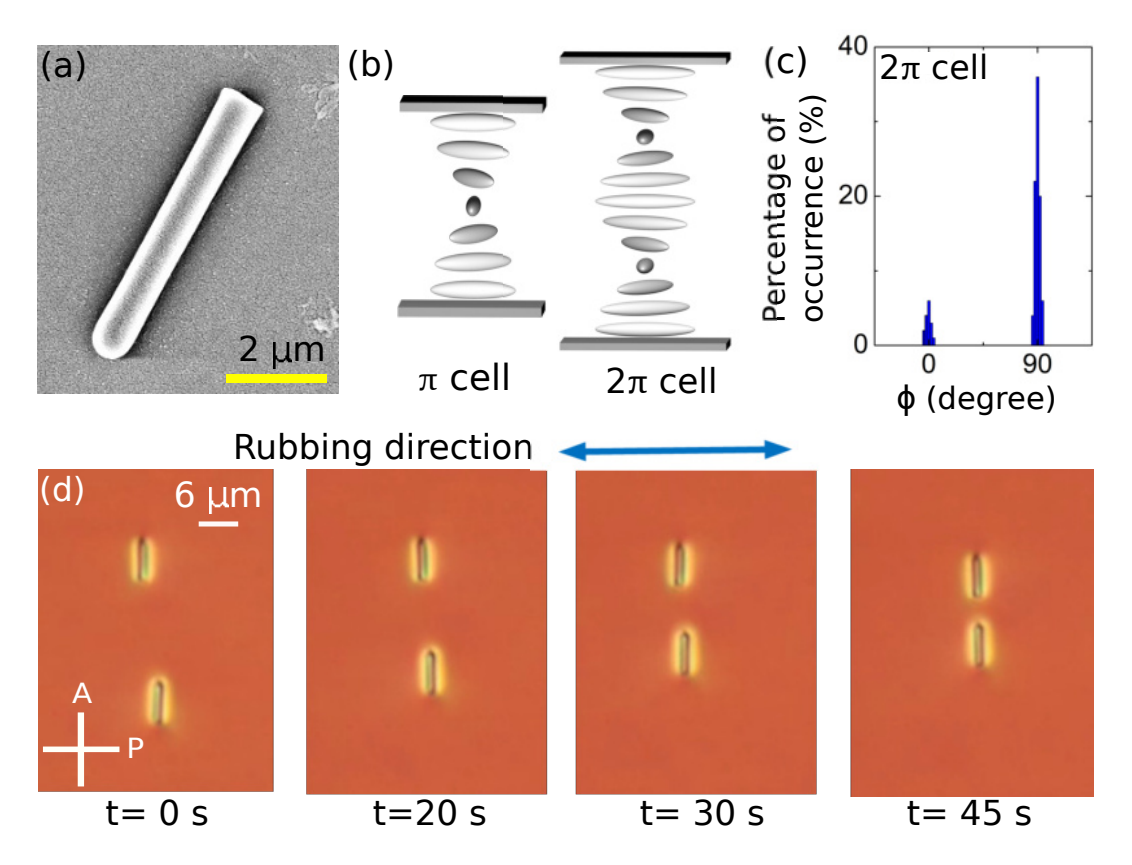


Figure 4.3: (a) Field emission scanning electron microscope (FESEM) image of a silica micro-rod. (b) Director twist in  $\pi$  and  $2\pi$ -twisted nematic cells. (c) Percentage of micro-rods oriented parallel ( $\phi = 0^{\circ}$ ) and perpendicular ( $\phi = 90^{\circ}$ ) to the rubbing direction in a  $2\pi$ -twisted cell. (d) Polarizing optical microscope images of two interacting micro-rods with elapsed time. Horizontal arrow indicates the rubbing direction. P, A indicates polarizer and analyzer.

We study the pair interaction of micro-rods oriented perpendicular to the rubbing direction in a  $2\pi$ -twisted cell. Two coaxial micro-rods were positioned at a certain distance with the help of the laser tweezers and allowed them to interact freely after switching off the laser. Figure 4.3(d) shows a few snapshots at different times while they are approaching to each other. Figure 4.4(a) shows that the tip-to-tip separation decreases with increasing time and eventually they are self-trapped at a certain separation forming a bound state. The mean tip-to-tip separation between the micro-rods in the bound state (see after 130 s) is 1.65  $\mu$ m and remains fixed forever (see Fig. 4.5(a) which is taken for longer time). It appears as if the micro-rods are trapped in the global energy minimum. Similar behaviour is also observed in cells with different chiralities and the tip-to-tip separation decreases moderately with increasing chirality as shown in the inset of Fig. 4.5(b). It is observed that the equilibrium separation in the bound state is lower in  $4\pi$ -twisted cell than that in the  $\pi$ -twisted cell. We also studied the interaction of two micro-rods in a planar 5CB without any chiral dopant. In this case, the separation decreases with increasing time and finally one micro-rod goes under the other hence, the separation appears to be zero (see Fig. 4.4(b)). Thus the equilibrium configuration of the micro-rods in chiral NLCs is distinctly different than those in a planar non-chiral NLCs.

The micro-rods in  $2\pi$ -twisted cell show a dipolar interaction which is evidenced from the fitting of the time dependence of the particle separation (Fig. 4.4(a)) and given by  $R(t) = (R_0^5 - 5\alpha_d t)^{1/5}$ , where  $\alpha_d$  is a constant and  $R_0$  is the separation at t = 0 s (see Eq. (1.28) in chapter-1). On the other hand in planar 5CB cell (without chirality), they show quadrupolar type interaction which is confirmed from the fitting of the time dependent separation to  $R(t) = (R_0^7 - 7\alpha_q t)^{1/7}$  as shown in (Fig. 4.4(b)). It is observed that in both cases R(t) fits the data well with the adjustable fit parameters  $\alpha_d = 1.0 \times 10^3 \ \mu\text{m}^5/\text{s}$  and  $\alpha_q = 3.2 \times 10^6 \ \mu\text{m}^7/\text{s}$  for dipolar and quadrupolar interactions, respectively. We are unable to fit the trajectory, shown in Fig. 4.4(a) to a quadrupolar and the trajectory, shown in Fig. 4.4(b) to a dipolar interactions, which are displayed by dashed curves. The interaction potentials shown in the insets are calculated from R(t). Since the system is highly over-damped (Reynolds number << 1) the Stokes drag force  $F_S = 6\pi L_{eff} \eta \partial R_t/\partial t = -F_{el}$ , where  $L_{eff}$  is the effective length and  $F_{el}$  is the elastic force. The interaction potential U is obtained by integrating  $F_{el}$  over

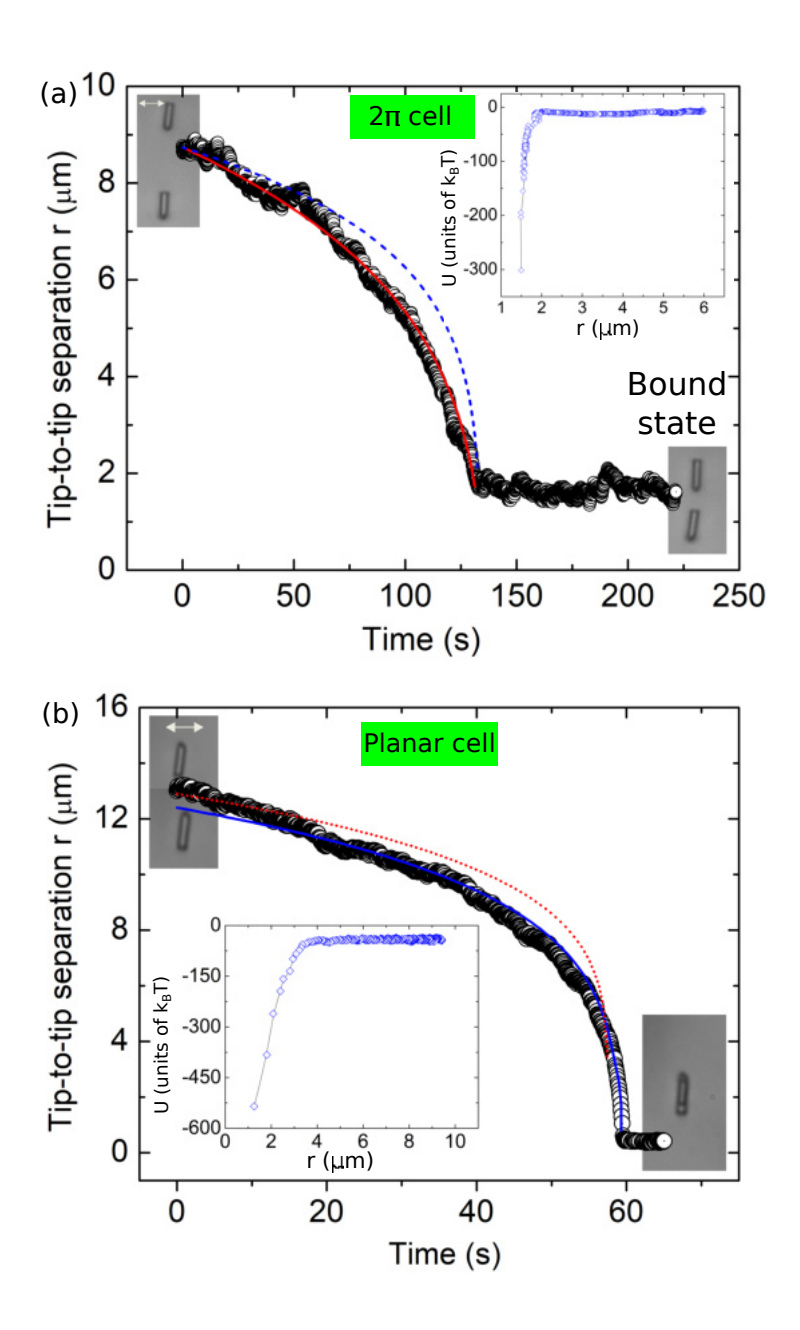


Figure 4.4: (a) Time dependence of tip-to-tip separation of two interacting microrods in a  $2\pi$ -twisted cell. Solid red curve display the least square fit to the equation  $R(t) = (R_0^5 - 5\alpha_d t)^{1/5}$  for dipolar type interaction. (b) Time dependence of tip-to-tip separation in a planar 5CB cell (without chiral dopant). Solid blue curve display the least square fit to the equation  $R(t) = (R_0^7 - 7\alpha_q t)^{1/7}$  for quadrupolar interaction. The insets show respective interaction potentials. The dashed blue curve in (a) and dotted red curve in (b) display fits to a quadrupolar and dipolar interactions, respectively.

the distance moved by the particle,  $U = \int F_{el} dR$ . For this purpose we have measured independently the drag coefficients  $\zeta_x$  and  $\zeta_y$ , parallel and perpendicular to the rubbing direction from the measurement of the diffusion coefficients (see Fig. 4.8(a)) and used an average value  $\zeta_a = 2.2 \times 10^{-6}$  Kg/s for potential calculations. The minimum of the dipolar potential energy in  $2\pi$ -twisted cell (inset Fig. 4.4(a)) is 300 k<sub>B</sub>T which is slightly lesser than that of the quadrupolar interaction energy (540 k<sub>B</sub>T) in the planar 5CB cell (inset Fig. 4.4(b)).

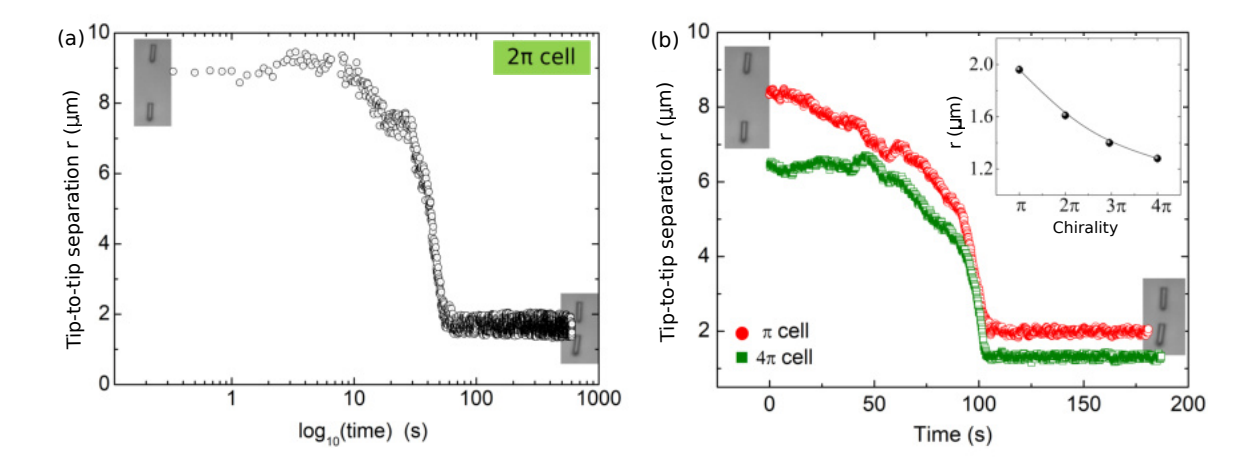


Figure 4.5: (a) Tip-to-tip separation between a pair of micro-rods in  $2\pi$ -twisted cell with time (in semi-log scale). The data is presented here for about 10 minutes but the observation was made for 3 to 4 hrs to confirm that the bound state is stable. (b) Tip-to-tip separation in  $\pi$  (red circles) and  $4\pi$ -twisted (green squares) cells. Inset shows the tip-to-tip separation with chirality.

We also studied the interaction of micro-rods in a side-to-side configuration as shown in Fig. 4.6(a). In this case the dipolar micro-rods have an antiparallel orientation. They are attracted and finally settled at a small surface-to-surface separation (600 nm). Figure 4.6(b) exhibits the time dependency of center-to-center separation. It is well fitted to  $R(t) = (R_0^5 - 5\alpha_d t)^{1/5}$  for a dipolar type interaction with fit parameter  $\alpha_q = 6.4 \times 10^3 \ \mu \text{m}^5/\text{s}$ . As indicated by the dashed line, the trajectory does not fit into a quadrupolar interaction. The interaction potential associated with this configuration is shown as inset to Fig. 4.6(b). The potential energy minimum is approximately 1300 k<sub>B</sub>T, which is significantly higher than the tip-to-tip configuration. The overall anisotropy of the pair interaction was studied by examining the relative trajectories of

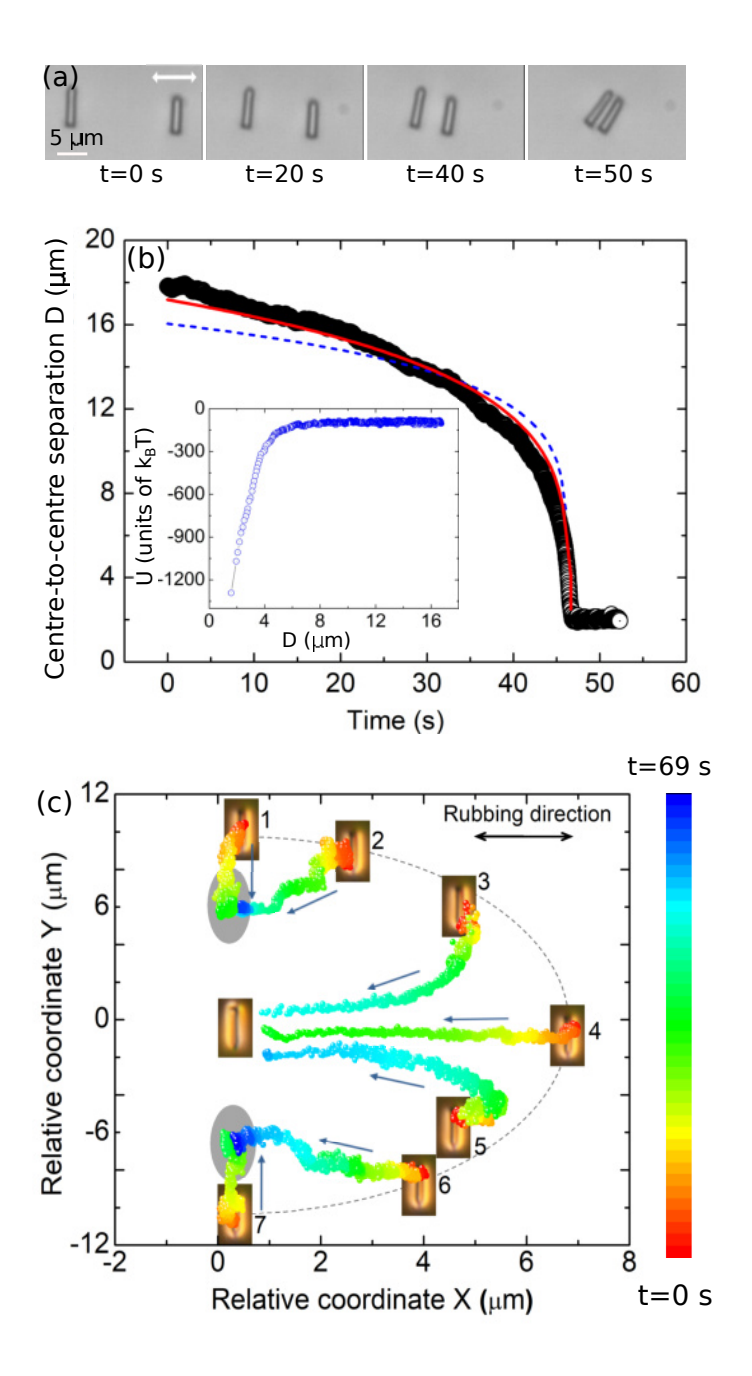


Figure 4.6: (a) CCD images with elapsed time showing interacting micro-rods in a side-to-side configuration. (b) Time dependence of the micro-rod-separation in side-to-side configuration. Solid red curve display the best fit to equation:  $R(t) = (R_0^5 - 5\alpha_d t)^{1/5}$  for dipolar interaction. Inset shows the interaction potential. The dashed blue curve display fits to a quadrupolar interaction. (c) Time coded trajectories (relative coordinates) of micro-rods approaching from different starting positions in a  $2\pi$ -twisted cell. By "relative coordinate" we mean relative to the starting point of each trajectory. Grey shaded elliptical regions indicate where the approaching particle is bound with the central particle.

two micro-rods interacting from different starting positions, as shown in Fig. 4.6(c). Micro-rods released from locations 1, 2, 6, and 7 form a bound state with a greater separation than micro-rods released from locations 3, 4, and 5.

The striking result of our experiment is that the micro-rods are self-trapped at a certain separation forming a stable bound state. The origin of the bound state can be understood from the competing effect of the electrostatic and elastic interactions. The surface of the silica micro-rods are negatively charged [11]. To demonstrate the effect of the surface charge, we heated the sample to the isotropic phase where the elastic interaction between them is not present and pushed the rods towards each other using laser tweezers. The micro-rods stay away from each other against the impelling force, demonstrating an electrostatic repulsion between them due to the surface charge. We measured the total charge Q of individual micro-rods from the electrophoretic motion of the particles in a chiral NLC under a dc electric field E. A schematic diagram of the planar cell used in this experiment is shown in Fig. 4.7(a). On a glass plate, two copper tapes (Cu) of thickness 35  $\mu$ m and width 5 mm are separated by d=1mm. A thin glass plate covers the top side, and the cell is sealed with a UV curable adhesive (NOA-81, Norland). The colloidal mixture is then introduced into the cell. The electrodes are attached to an external dc power supply (TD3202M, Aplab). The micro-rod moves from the negative to the positive electrode, when a dc electrical field of magnitude U = 10 V is applied and the direction of motion is reverted by altering the field polarity. It means the micro-rods are negatively charged. Fig. 4.7(c) shows a few CCD images of the moving particle with elapsed time. The velocity of the micro-rod v under the dc field is calculated from the time-dependent position, as shown in Fig. 4.7(b). Since the Reynold's number  $R_{\rm e} \ll 1$ , the total charge Q can be determined by balancing the viscous drag force  $F_S = \zeta_a v$  with the electrostatic force  $F_Q = QE$  acting on the micro-rods, where the average friction coefficient  $\zeta_a = k_B T/D$ , D being the diffusion coefficient. The total charge,  $Q = \zeta_a v d/U$  can be obtained by equating these two forces. The average friction coefficient is given by  $\zeta_a = 2.2 \times 10^{-6}$ Kg/s (see later). The velocity of the particles is calculated from the displacement-time graph is given by  $v = 0.76 \pm 0.1 \mu \text{m}$ . The total charge of a micro-rod is calculated to be  $Q \simeq -(1045\pm24)e$ , where  $e = 1.6\times10^{-19}$  C. The surface charge density  $\sigma = Q/\text{surface}$ area =  $1.3 \times 10^{-5}$  C/m<sup>2</sup>. The approximate charge at the round tip of the micro-rod is estimated to be -82 e. Considering the electrostatic repulsion is mainly due to the charges at the tip, the Coulomb energy between the two tips at a separation of 1.65  $\mu$ m is 227 k<sub>B</sub>T. Thus, the electrostatic potential energy is comparable to the elastic energy (300 k<sub>B</sub>T) of the micro-rods [see inset of Fig. 4.4(a)]. Hence, the metastable state turns out to be a bound state.

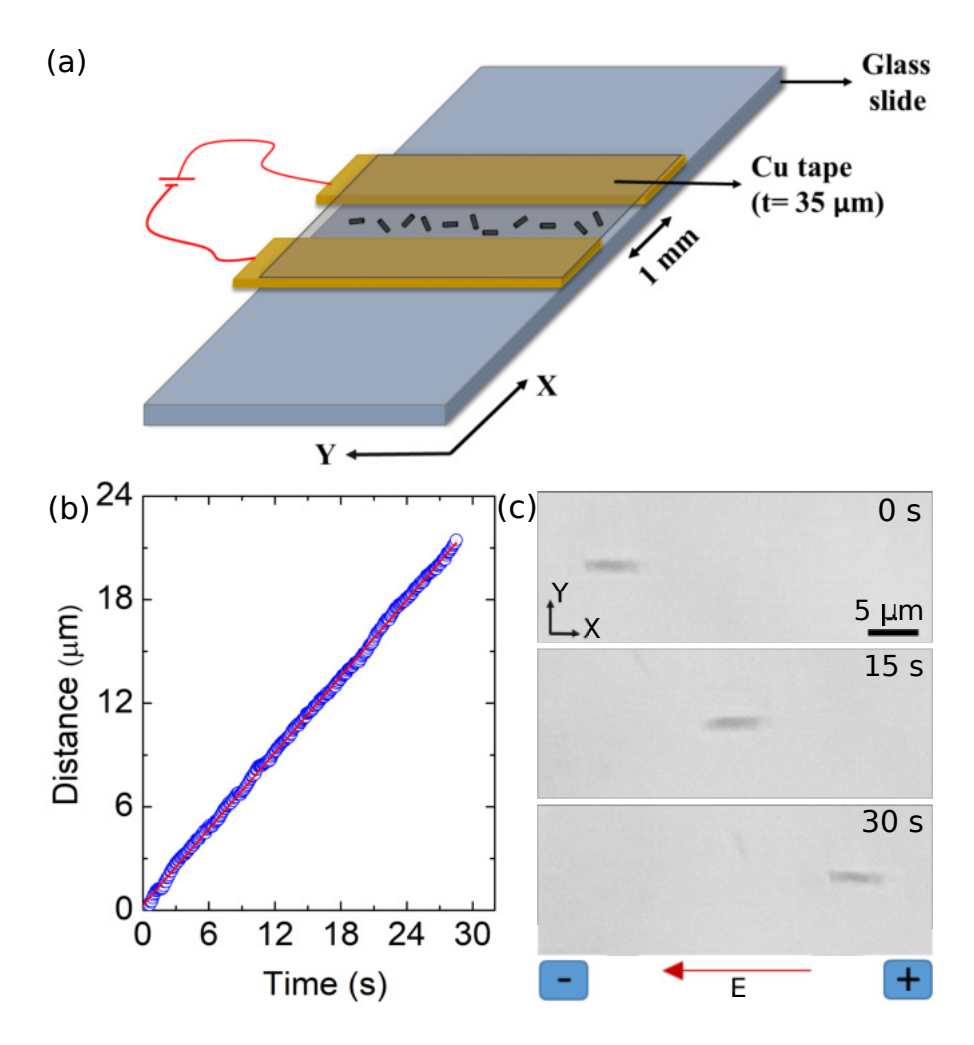


Figure 4.7: Measurement of total charge Q of DMOAP coated micro-rods in a chiral NLC. (a) Schematic diagram of the cell used in the experiment. (b) Variation of displacement of the particle position with time when a dc field of 10 V is applied between the copper (Cu) tapes, separated by 1.0 mm distance. The solid red line is a linear fit to the data. (c) CCD images showing the motion of a micro-rod under the field. Note that the micro-rod moves from the negative to the positive electrode, indicating it is negatively charged.

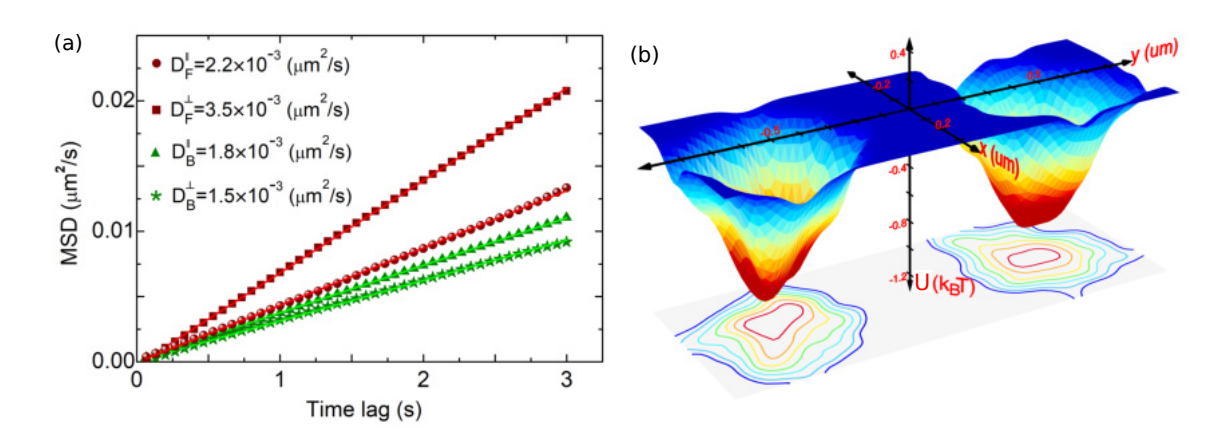


Figure 4.8: (a) Mean squared displacements (MSDs) of a free micro-rod (red squares and circles) and a bound micro-rod (green triangles and stars) in a  $2\pi$ -twisted cell. The subscripts F and B stands for free and bound micro-rods, respectively and the superscripts || and  $\bot$  indicate motions parallel and perpendicular to the rubbing direction. (b) Confining potentials of the bound micro-rods. Separation along the y-direction is normalized.

In the bound state, the Brownian motions due to thermal agitation of the micro-rods are observed. The self-diffusion coefficients  $D_B^{\parallel,\perp}$  of a micro-rod in the bound state and  $D_F^{\parallel,\perp}$  of a micro-rod in free or isolated state (where  $\parallel$  and  $\perp$  denotes components with respect to the rubbing direction) were measured from the mean squared displacement. Figure 4.8(a) shows that  $D_B^{\perp} \simeq 0.4 D_F^{\perp}$  and  $D_B^{\parallel} \simeq 0.8 D_F^{\parallel}$  i.e., the diffusion coefficients in the bound state are reduced considerably than that of a free micro-rod as expected. In an isotropic solvent, the proximity of the surface due to sedimentation often alters the Brownian motion and thus the friction coefficients [12]. However, in NLCs, sedimentation of microparticles is prevented by thermal fluctuations and the elasticity of the medium as the gradients of the director field push the particles away from the bottom [13]. Hence, the Brownian motion and the estimated friction coefficients of the micro-rods are not influenced by the substrates. It may be mentioned that the anisotropic particles in an isotropic solvent like, water have both positional and orientational degrees of freedom [14]. However, in our system the orientational fluctuations of the micro-rods are reduced compared to that in water due to the nematic order.

We have measured the effective confining potentials from the study of the Brownian statistics of the micro-rods in the region accessible by thermal agitations. In equilibrium, the probability density of the particle position is given by  $p(x) = C \exp[-U(x)/k_BT]$ , where U(x) is the confining potential and C is the normalisation constant [15]. U(x) = -ln[p(x)] is the potential calculated from the normalised histogram of the confined particle's positions. The confining potentials of the micro-rods at a normalized center-to-center separation are shown in Fig. 4.8(b). The depth of the potential energy is in the order of few  $k_BT$  and the shape is asymmetric as expected. Assuming the potentials are harmonic, the effective stiffness constants  $k_x$  (along rubbing direction) and  $k_y$  (perpendicular to the rubbing direction) are given by  $k_x = 4.3 \pm 0.1 \times 10^{-6} \text{ N/m}$  and  $k_y = 4.8 \pm 0.1 \times 10^{-6} \text{ N/m}$ , respectively. The stiffness constants of the confining potentials are comparable to that of the low power optical traps [7,16].

To test the robustness of the bound state we applied an external ac electric field that perturbs the position and orientation of the micro-rods. An ac field is applied between the two ITO (indium-tin-oxide) glass plates and the direction of field is perpendicular to the director as shown in Fig. 4.9(a). Figure. 4.9(b) shows some snapshots at various field strengths. The maximum field strength applied (0.18 V/ $\mu$ m) is below the Freederickzs threshold field (0.2 V/ $\mu$ m) so that there is no director reorientation. Above the field of  $0.12 \text{ V/}\mu\text{m}$ , the micro-rods also tilt both in the plane and out of the plane simultaneously. The initial state is recovered when the field is reduced to zero. The tilting of the micro-rods along the field direction beyond a particular field is due to the competing effect of electric field-induced torque and hydrodynamic torque [17,18]. We further checked the stability of the bound state by applying a mild mechanical force with the help of the laser tweezers as shown in Fig. 4.10(a). As shown in Fig. 4.10(b), we assembled several micro-rods into a linear chain using the laser tweezers. Here, each rod is connected through successive bound states. The chain is a little zigzag, which could be due to a slight variation in the length and diameter of the micro-rods. Nevertheless, the chain is highly stable against thermal fluctuations and mild perturbing force applied by the laser tweezers and remains unchanged even after a few days. It may be mentioned that although one end of the micro-rods is round-shaped, the bound state formation does not depend on the shape of the facing ends.

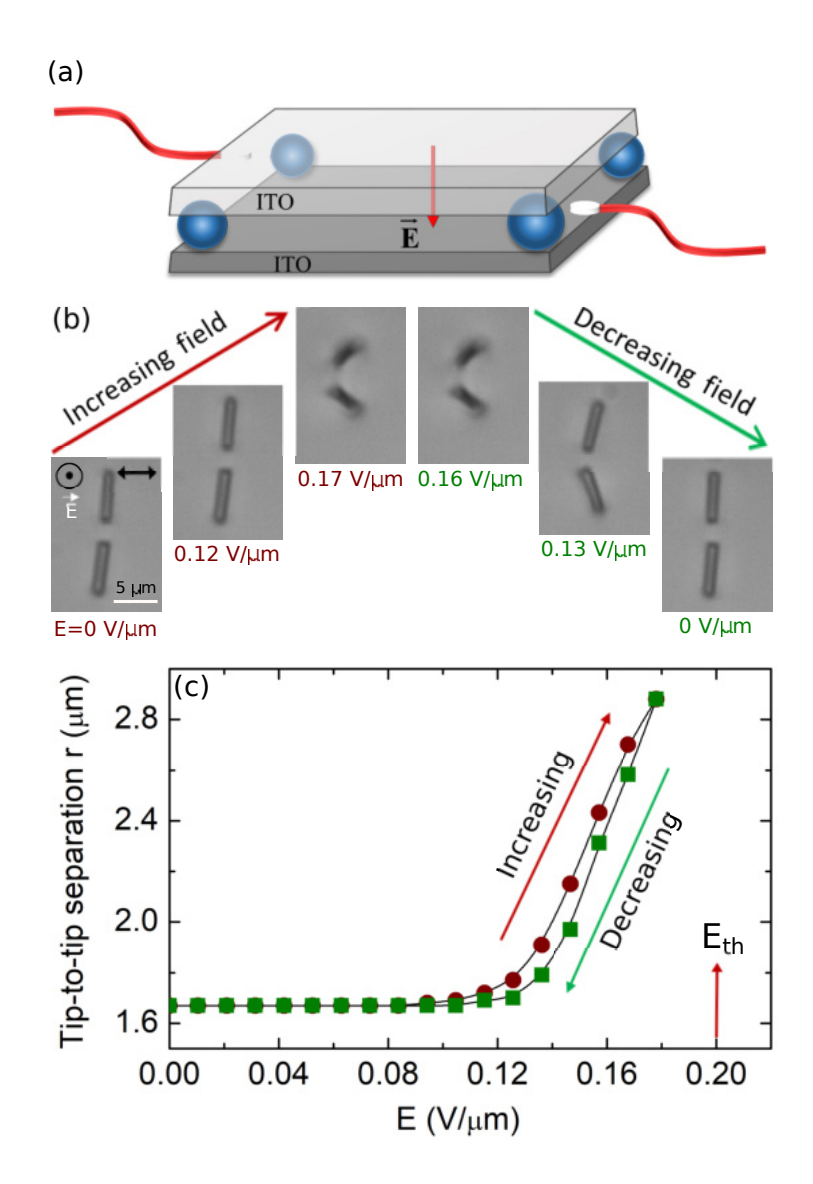


Figure 4.9: (a) Diagram of the cell for the electric field experiments. The direction of the electric field between the ITO plates is perpendicular to the director. (b) CCD images with elapsed time showing the effect of ac electric field (f = 1 kHz) on the bound state in a  $2\pi$ -twisted cell. (c) Variation of tip-to-tip separation with increasing (circles) and decreasing (squares) electric field. The vertical arrow indicates the Freedericksz threshold field  $(E_{th})$ .

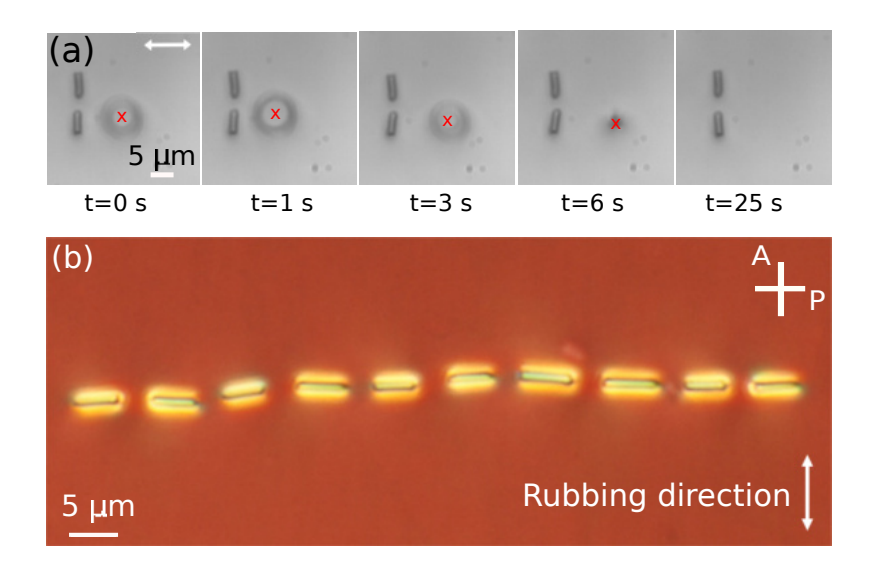


Figure 4.10: (a) CCD images with elapsed time showing the effect of elastic distortion created by the laser tweezers on the bound state in a  $2\pi$ -twisted cell. (b) A linear chain of ten micro-rods forming successive bound states. They were guided to assemble with the help of the laser tweezers setup.

In what follows, we study the correlated thermal fluctuations of micro-rods in the bound state. We have measured the position of the particles and calculated the autocorrelation and cross-correlation functions. Figure 4.11 shows that the autocorrelation function decays exponentially as expected whereas a strong time delayed-anticorrelation is observed with a pronounced minimum. Similar anti-correlation of a pair of optically trapped microspheres in aqueous solution have been reported and it was explained on account of their hydrodynamic interactions [7,8]. In order to explore possible hydrodynamic coupling between the two micro-rods, we have analysed our results following the method discussed in Refs [7,8]. Also see chapter-1 for details. In the framework of Langevin dynamics for a low Reynolds number system, the autocorrelation and the cross-correlation functions of position vectors of the two particles along the y-direction (perpendicular to the rubbing direction) can be expressed as [7]

$$\langle R_1(t)R_1(0)\rangle = \langle R_2(t)R_2(0)\rangle$$

$$= \frac{k_B T}{2k_y} \left(e^{-t(1+\epsilon)/\tau} + e^{-t(1-\epsilon)/\tau}\right)$$
(4.2)

and

$$\langle R_1(t)R_2(0)\rangle = \langle R_2(t)R_1(0)\rangle$$

$$= \frac{k_B T}{2k_u} \left(e^{-t(1+\epsilon)/\tau} - e^{-t(1-\epsilon)/\tau}\right)$$
(4.3)

where  $\tau$  is the relaxation time and  $\epsilon$  is a dimensionless parameter. The autocorrelation and cross-correlation functions in  $\pi$  and  $2\pi$ -twisted cells were measured and the theoretical fits to Eq. (4.2) and Eq. (4.3) are shown in Fig. 4.11. The parameters obtained from the fittings are given by  $\tau = 0.64 \pm 0.01$  s and  $\epsilon = 0.10 \pm 0.01$ . This means that the hydrodynamic interaction is asymmetric: as one micro-rod moves, it tends to drag its pair particle and the correlated fluctuations relax faster than the anticorrelated fluctuations. We calculate  $\epsilon$  directly from the particle separation and  $\tau$ from the effective confining potentials.  $\tau$  is given by the ratio of the friction coefficient  $\zeta_y$  and the stiffness constant  $k_y$  of the potential i.e.,  $\tau = \zeta_y/k_y$ . The parameter  $\epsilon$  describes the ratio of the mobility of the particle and the strength of the hydrodynamic coupling and is expressed as  $\epsilon \approx 3a/2r$ , where a is the radius of the particle and r is the mean separation [7]. Using the Stokes-Einstein relation and measured diffusion coefficient (Fig. 4.8(a)), we obtain  $\zeta_y = 2.8 \times 10^{-6}$  Kg/s. Taking  $k_y = 4.8 \times 10^{-6}$  N/m from the confining potentials (Fig. 4.8(b)), the radius of the micro-rod  $a=0.4~\mu m$ and the centre-to-centre separation  $r \simeq 7 \mu \text{m}$ , the calculated parameters are  $\tau = 0.58$ s and  $\epsilon \simeq 0.09$ . These parameters are in good agreement with those obtained from the fitting of the autocorrelation and cross-correlation functions. It is also evident in Fig. 4.11 that the depth of the minimum in the  $2\pi$ -twisted cell is higher than that of the  $\pi$ -twisted cell. Since the colloidal pair in the  $2\pi$ -twisted cell are closer than in the  $\pi$ -twisted cell (inset of Fig. 4.5(b)), the result confirms that the strength of the hydrodynamic interaction is inversely proportional to the separation [7]. The above model for spherical particles dispersed in an isotropic solvent is adapted for NLCs, assuming that the nematic director remains uniform over the length scale of interparticle separation, and thus the hydrodynamic contribution to the director mode is negligible. This could be reasonable as the NLC is aligned by confining surfaces and the director is fairly uniform in the gap between the two tips of the two micro-rods (Fig. 4.3(d)). Hydrodynamic interaction has been considered in two-point particle tracking microrheology in NLCs [19]. Theoretically it could be interesting to investigate the contribution of the director mode on the two-particle auto- and cross-correlation functions.

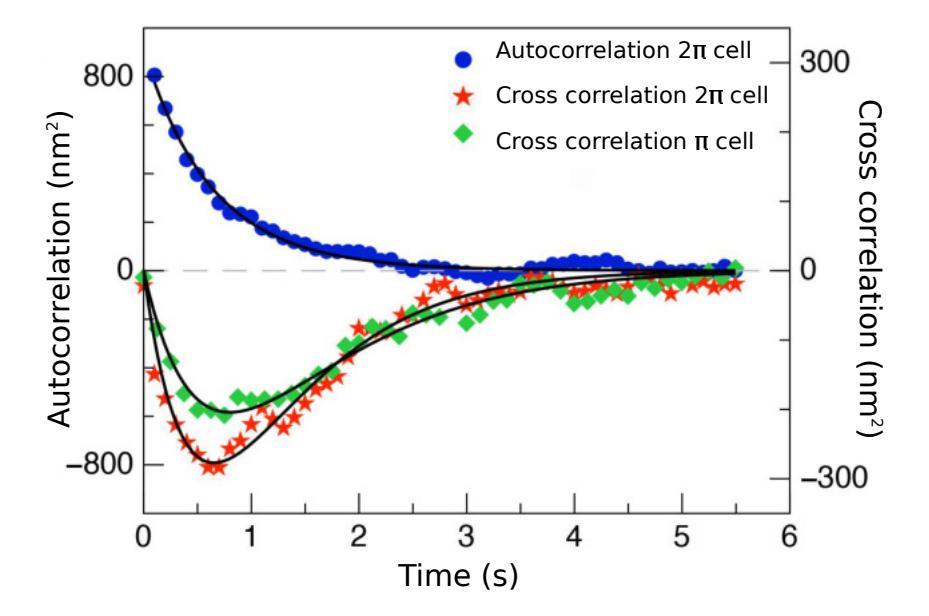


Figure 4.11: Longitudinal autocorrelation  $\langle R_1(t)R_1(0)\rangle$  (blue circles) and cross-correlation  $\langle R_1(t)R_2(0)\rangle$  (green diamonds and red stars) functions of the micro-rods in  $\pi$  and  $2\pi$ -twisted cells. Solid lines represent the least square fits to Eq. (4.2) and Eq. (4.3) for auto and cross correlation functions.

Along with the position fluctuations, the orientational fluctuations of the microrods are also observable in the bound state. The orientational fluctuations  $\theta_1(t)$  and  $\theta_2(t)$  of the long axes of the micro-rods are measured with respect to their mean orientations. As shown in the inset of Fig. 4.12, the histogram of the orientational fluctuations of a bounded micro-rod is a Gaussian. We measured the autocorrelation  $\langle \theta_1(t)\theta_1(0)\rangle$  and cross-correlation  $\langle \theta_1(t)\theta_2(0)\rangle$  of the orientational fluctuations. The autocorrelation function decays exponentially as shown in Fig. 4.12 and it can be well fitted to  $\langle \theta_1(t)\theta_1(0)\rangle \sim e^{-t/\tau_o}$  with a decay constant  $\tau_o$ =56 ms. The value of decay constant is comparable to the director relaxation time of 5CB liquid crystal. We

measured the director relaxation time of 5CB LC  $\tau_o \simeq 50$  ms, using an electro-optic technique (dynamic Freedericksz transition) in a planar cell of thickness 5  $\mu$ m at room temperature.

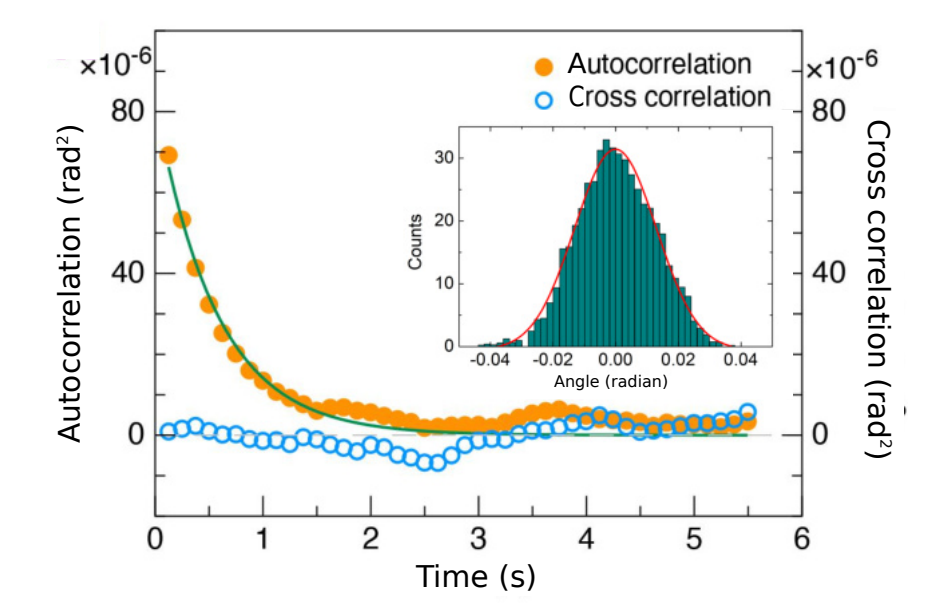


Figure 4.12: Autocorrelation function  $\langle \theta_1(t)\theta_1(0)\rangle$  (solid circles) and cross-correlation function  $\langle \theta_1(t)\theta_2(0)\rangle$  of orientational fluctuations (open circles) of two micro-rods in  $2\pi$ -twisted cell. Solid line indicates the least square fit to  $\langle \theta_1(t)\theta_1(0)\rangle$ . Only every third of the experimental data points is shown. The inset shows the histogram of orientational deviation.

The correlation relaxation time of hydrodynamic interaction obtained from the fitting in our chiral NLCs is  $\tau = 0.64$  s, which is 15 times larger than that of a microsphere in water (43 ms) [7]. This is expected due to the larger viscosity of the liquid crystal  $(\eta_{||}^{5CB} \simeq 20 \text{ mPas})$  in comparison to water  $(\eta_W \simeq 1 \text{ mPas})$  [20]. Although the theoretical technique adapted here is for hydrodynamic interactions in low Reynolds number  $(R_e)$  fluid systems, we expect it to be valid as  $R_e$  of NLCs is much smaller than 1  $(R_e \sim 10^{-4} - 10^{-5})$  [21, 22].

We also studied a pair of nano-rods whose diameter is much smaller. Figure 4.13(a) shows a few snapshots of two nano-rods approaching each other. The separation between the two particles remains fixed during the time interval 40–65 s. i.e. particles stay in a metastable state for a short period of time. These two particles exert Brow-

nian motion with an average constant separation as if they were temporarily trapped in two neighbouring potential wells. Eventually both the particles are attracted to assemble side by side as shown in Fig. 4.13(b). Experiments are also performed for different chirality ( $\pi$ ,  $2\pi$ ,  $4\pi$  cells represented as different colours). It is found that metastable state forms at a fixed separation (centre-to-centre separation  $\approx 5\mu$ m) irrespective of the pitch of the sample. Also the duration of the metastable state ( $\approx 25$  s) is almost independent of chirality.

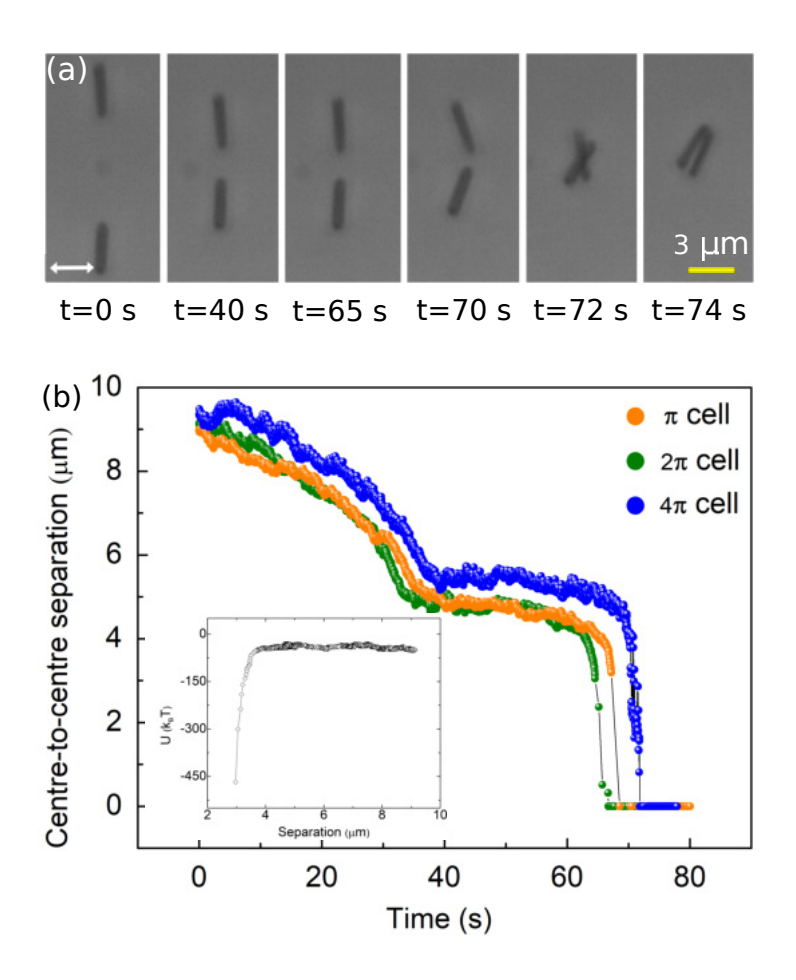


Figure 4.13: (a) Snapshots of a pair of nano-rods interacting at different times taken using polarizing optical microscope. (b) The time evolution of separation between two vertically oriented nano-rods in chiral NLC. Different colours represents different pitch of the sample.

To understand the origin of metastable state, we calculated the total charge of a nano-rod and found to be  $Q \simeq -(280)e$ ,  $e = 1.6 \times 10^{-19}$  C. The surface charge density  $\sigma = Q/A = 0.9 \times 10^{-5}$  C/m<sup>2</sup>. The approximate charge at the round tip of the nano-

#### 4.4. Conclusion

rod is estimated to be -55 e. Considering the electrostatic repulsion is mainly due to the charges at the tip, the Coulomb energy between the two tips at a separation of 1.6  $\mu$ m is 105 k<sub>B</sub>T. The minimum of the elastic potential energy ( $\approx 450 \text{ k}_B\text{T}$ ) is four times higher than the electrostatic energy of the nano-rods (see inset of Fig. 4.13(b)). Hence, particles attracts each other after staying in metastable state for a short interval of time.

### 4.4 Conclusion

We studied a pair of charged silica micro-rods with homeotropic anchoring conditions in chiral NLCs. When two micro-rods aligned perpendicular to the rubbing direction are brought in a closer separation, they are self-trapped due to the competing effect of elastic attraction and Coulomb repulsion, forming a colloidal bound state. The bound state is highly stable and robust against the influence of external electrical and mechanical perturbations. In the bound state the positional fluctuations of the micro-rods are hydrodynamically coupled whereas their orientational fluctuations are uncoupled. The correlation relaxation time of hydrodynamic interaction in chiral nematic liquid crystals is more than one order of magnitude larger than that in aqueous suspensions. We also studied the interaction of nano-rods and found that they form a metastable state. Apart from the interplay of elasticity and defects, the hydrodynamic interaction in chiral NLCs plays an important role in colloidal self-assembly. The abundance of new shape anisotropic particles and their unusual topological properties in chiral NLCs widen the scope of further studies.

# References

- [1] V. S. R. Jampani, M. Škarabot, S. Čopar, S. Žumer and I. Muševič, *Chirality screening and metastable states in chiral nematic colloids*. Phys. Rev. Lett., vol. 110, pp. 177801, 2013.
- [2] H. Mundoor, S. Park, B. Senyuk, H. H. Wensink and I. I. Smalyukh, Hybrid molecular-colloidal liquid crystals. Science, vol. 360, pp. 768-771, 2018.
- [3] H. Mundoor, B. Senyuk and I. I. Smalyukh, *Triclinic nematic colloidal crystals from competing elastic and electrostatic interactions*. Science, vol. 352, pp. 69-73, 2016.
- [4] K. Stratford, A. Gray and J. S. Lintuvuori, *Large colloids in cholesteric liquid crystals*. J. Stat. Phys., vol. 161, pp. 1496-1507, 2015.
- [5] G. Foffano, J. S. Lintuvuori, A. Tiribocchi and D. Marenduzzo, The dynamics of colloidal intrusions in liquid crystals: a simulation perspective. Liq. Cryst. Rev., vol. 2, pp. 1-27, 2014.
- [6] J. S. Lintuvuori, K. Stratford, M. E. Cates and D. Marenduzzo, Colloids in cholesterics: size-dependent defects and non-stokesian microrheology. Phys. Rev. Lett., vol. 105, pp. 178302, 2010.
- [7] J. C. Meiners and S. R. Quake, Direct measurement of hydrodynamic cross correlations between two particles in an external potential. Phys. Rev. Lett., vol. 82, pp. 2211, 1999.
- [8] P. Bartlett, S. I. Hendersons and S. J. Mitchell, Measurement of the hydrodynamic forces between two polymer-coated spheres. Philos. Trans. R. Soc. London A, vol. 359, pp. 883, 2001.

- [9] M. Škarabot et al., Laser trapping of low refractive index colloids in a nematic liquid crystal. Phys. Rev. E, vol. 73, pp. 021705, 2006.
- [10] D. Podolskyy, O. Banji and P. Rudquist, Simple method for accurate measurements of the cholesteric pitch using a "stripe-wedge" Grandjean-Cano cell. Liq. Crys., vol. 35, pp. 789-791, 2008.
- [11] H. E. Bakker, T. H. Hesseling, J. E. G. J. Winjnhoven, P. H. Helfferich, A. van Blaaderen and A. Imhof, *Microelectrophoresis of silica rods using confocal microscopy*. Langmuir, vol. 33, pp. 881-890, 2017.
- [12] L. P. Faucheux and A. J. Libchaber, Confined Brownian motion. Phys. Rev. E, vol. 49, pp. 5158, 1994.
- [13] O. P. Pishnyak, S. Tang, J. R. Kelly, S. V. Shiyanovskii and O. D. Lavrentovich, Levitation, lift, and bidirectional motion of colloidal particles in an electrically driven nematic liquid crystal. Phys. Rev. Lett., vol. 99, pp. 127802, 2007.
- [14] Y. Han, A. M. Alsayed, M. Nobili, J. Zhang, T. C. Lubensky and A. G. Yodh, Brownian motion of an ellipsoid. Science, vol. 314, pp. 626-630, 2006.
- [15] N. Osterman, TweezPal Optical tweezers analysis and calibration software. Comput. Phys. Commun., vol. 181, pp. 1911-1916, 2010.
- [16] A. Kuijk, A. van Blaaderen and A. Imhof, Synthesis of monodisperse, rodlike silica colloids with tunable aspect ratio. J. Am. Chem. Soc., vol. 133, pp. 2346-2349, 2011.
- [17] T. B. Jones, Electromechanics of Particles Cambridge University Press, Cambridge, UK, 1995.
- [18] M. V. Rasna, K. P. Zuhail, U. V. Ramudu, R. Chandrasekar and S. Dhara, Dynamics of electro-orientation of birefringent microsheets in isotropic and nematic liquid crystals. Phys. Rev. E, vol. 94, pp. 032701, 2016.
- [19] M. G. Gonzalez and J. C. del Alamo, Two-point particle tracking microrheology of nematic complex fluids. Soft Matter, vol. 12, pp. 5758-5779, 2016.

- [20] A. G. Chimielewski, Viscosity coefficients of some nematic liquid crystals. Mol. Cryst. Liq. Cryst., vol. 132, pp. 339-352, 1986.
- [21] D. K. Sahu, T. G. Anjali, M. G. Basavaraj, J. Aplinc, S. Čopar and S. Dhara, Orientation, elastic interaction and magnetic response of asymmetric colloids in a nematic liquid crystal. Sci. Rep., vol. 9, pp. 81, 2019.
- [22] O. D. Lavrentovich, *Active colloids in liquid crystals*. Curr. Opin. Colloid & Interface Sci., vol. 21, pp. 97-109, 2016.

5

# Electrophoretic mobility of silica micro and nano-rods in nematic liquid crystals

### 5.1 Introduction

In the last two chapters, we studied the orientation, interaction and assembly of rod-shaped silica particles in nematic and chiral NLCs. There are a huge variety of applications in soft matter physics, to move and orient solid particles within a fluid medium. Isotropic liquids like water, are the most common medium used to disperse solid particles, and electric field is the common driving force for the dynamic response of the particles. Recently, some interesting electrokinetic phenomena with spherically symmetric microparticles have been reported in an anisotropic medium such as liquid crystals (LCs) [1–3]. The observed effects are richer and more intricate in LC medium than in their isotropic equivalents.

A nonlinear induced electrophoretic motion of colloidal particles was explained based on the asymmetric flow of the NLC around the particle. The motility of the particles can be understood based on the surrounding electrokinetic flows of the fluid. Fig. 5.1 shows the director configuration and field induced flow of the fluid around a microsphere with a quadrupolar ring defect, boojum defect and dipolar point defect. An in-plane field is applied along the nematic director. Particles with quadrupolar configuration (Fig. 5.1(a) & 5.1(b)) is immobile under the applied field due to the fore-aft symmetry of the fluid flow along x and y axis, which results in zero electrophoretic

mobility. But for a particle with dipolar configuration (Fig. 5.1(c)), the symmetry is broken. The field dependence of the velocity of the propelling microsphere is given by [4],

$$v = \alpha \frac{\varepsilon_0 \bar{\varepsilon}}{\eta} \left| \frac{\Delta \sigma}{\bar{\sigma}} - \frac{\Delta \varepsilon}{\bar{\varepsilon}} \right| a E_x^2$$
 (5.1)

where  $\alpha$  is a numerical coefficient of order 1 and  $\eta$  is the anisotropic viscosity of the LC.  $\Delta \sigma$  and  $\Delta \varepsilon$  are the conductivity and dielectric anisotropy, respectively.

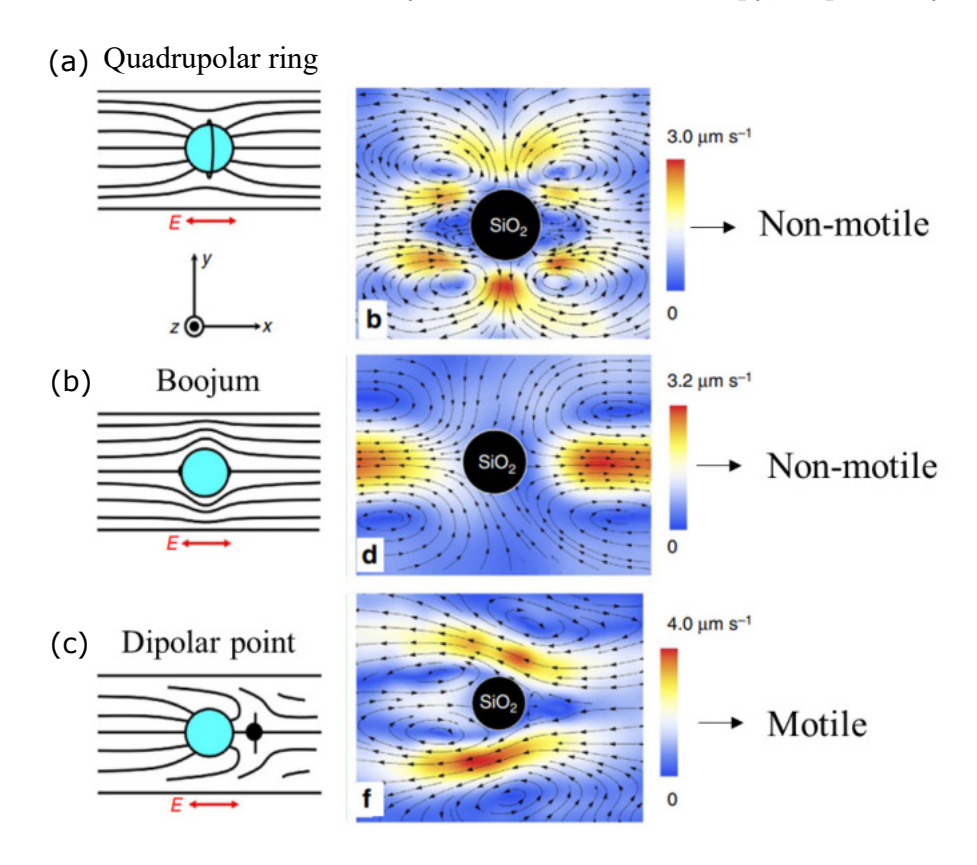


Figure 5.1: Liquid crystal director flow around a microsphere with (a) quadrupolar ring defect, (b) boojum defect and (c) dipolar point defect, dispersed in a uniformly aligned NLC under the effect of ac electric field. Images are adapted from Ref. [4].

In this chapter, we focus on the electric field driven motility of silica micro and nano-rods in a NLC. We show that the nano and micro-rods propel along the nematic director and simultaneously tilt in the direction of the applied electric field. We also demonstrate the light-induced rotation and translation of the micro and nano-rods in the nematic LC.

# 5.2 Experimental

We used the same silica micro and nano-rods as described in the previous chapters. The particles (DMOAP coated) are dispersed in a negative dielectric anisotropy nematic liquid crystal (MLC-6608,  $\Delta \epsilon = -4.2$ ) [5]. For light-induced studies, we used photoactive azo-dendrimers mixed with MLC-6608.

# 5.3 Results and discussion

We have shown in chapter-3 that, nano-rods orient mostly either parallel or perpendicular to the nematic director  $\hat{n}$  when dispersed in a NLC. In our experiment, we have considered particles oriented along  $\hat{n}$ . Figure 5.2(c & d) shows the cross polarized images of a nano and micro-rod oriented along  $\hat{n}$ , with a dipolar configuration. The defect structure of the particles in LCs have already been discussed in chapter-3. Schematic director distortion around a nano and micro-rod in a planar cell is shown in Fig. 5.3(a) and 5.3(b), respectively.

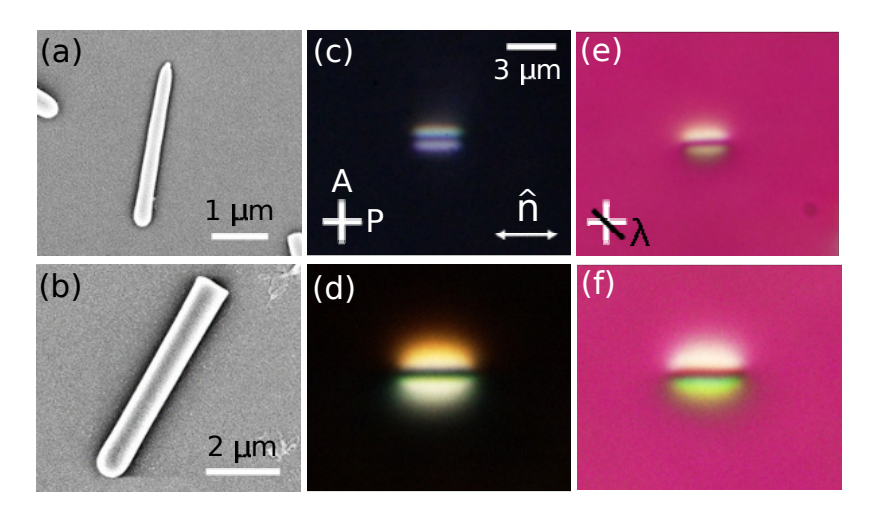


Figure 5.2: SEM images of a (a) silica nano-rod of  $l=3~\mu m$  and d=150~nm and a (b) micro-rod of  $l=6~\mu m$  and d=750~nm. (c,d) Optical polarizing photomicrographs of a DMOAP coated nano and micro-rod in a NLC. (e,f) Images are taken with crossed polarizers and a  $\lambda$ -plate.

A planar cell was chosen in our experiment, with the applied field perpendicular to the planar cell (Fig. 5.3(c)). A series of snapshots shows the transport of a nano and

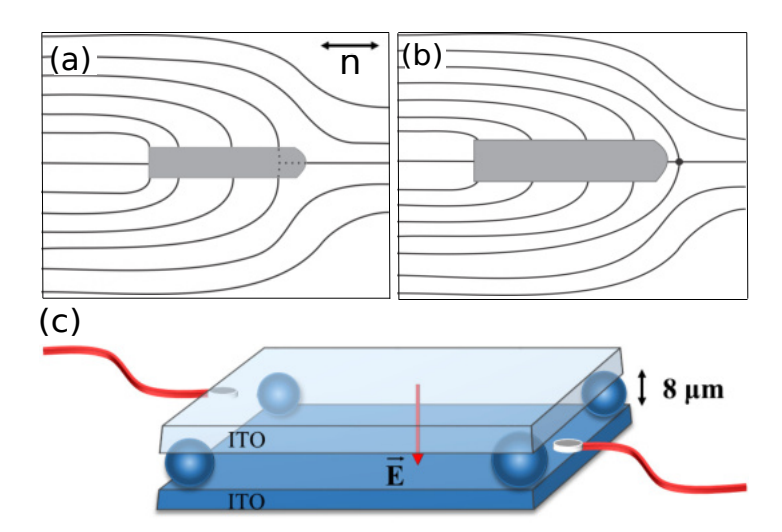


Figure 5.3: Schematic representation of the director distortions surrounding (a) the nano-rod and (b) micro-rod oriented parallel to the director. (c) Schematic diagram of the nematic cell. The direction of the electric field between the ITO glass plates is perpendicular to the director.

micro-rod. At zero field, the long axis of the rod is parallel to the nematic director field (Fig. 5.4(a) & Fig. 5.4(e)). When the field is increased, beyond a field amplitude of 1.36 V/ $\mu$ m, the nano-rod tilts towards the field direction (Fig. 5.4(b)) and starts to move along the director. In a similar way, a micro-rod also tilts and moves along the director when the field strength is beyond 1.43 V/ $\mu$ m (Fig. 5.4(f)). The dipolar particles move facing the point defect and this is expected. It should be noted that for the particles oriented perpendicular to the namatic director, the configuration is quadrupolar, and therefore they do not move as expected. This is similar to the results described by Lazo et al. for spherical particles [4].

We characterize the transport properties of the particles by measuring the velocity as a function of applied field at a constant frequency. Figure 5.5(a) shows the field dependence of velocity of a nano (blue circles) and micro-rod (red squares). Experiments are performed at a constant frequency (f=50 Hz). Below a field (E0 < 1.36 V/ $\mu$ m), nano-rods are non-motile. But beyond this field, the velocity increases with increasing field in a non-linear way. Similarly, a micro-rod also shows a non-linear dependency of velocity on the applied field beyond a field strength of E0 = 1.43 V/ $\mu$ m. For a given

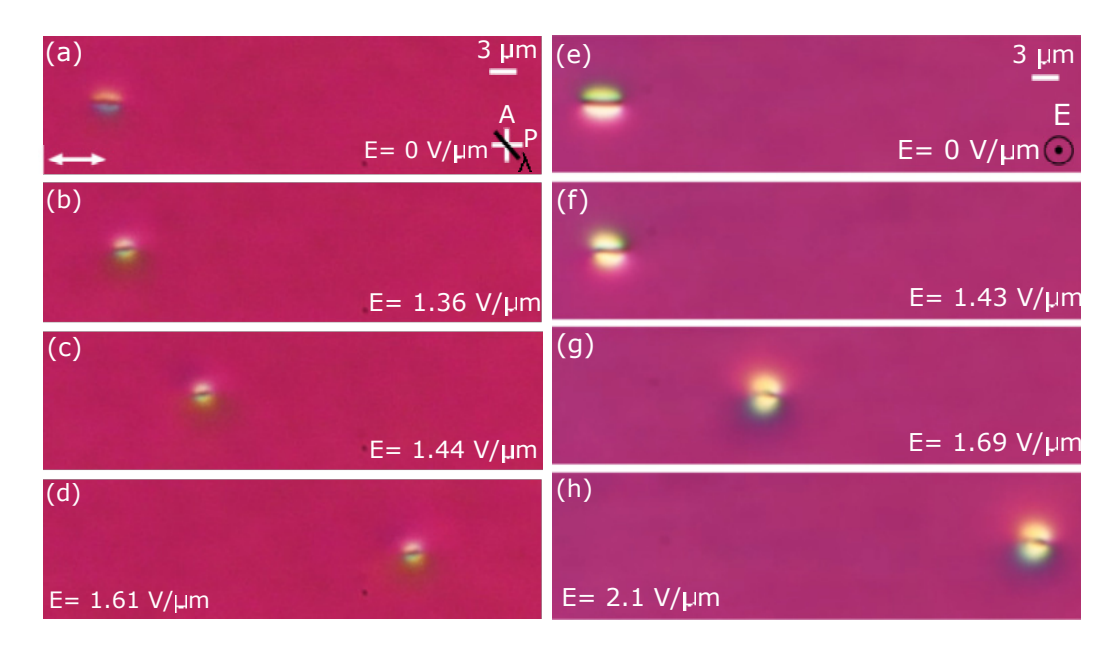


Figure 5.4: Electric-field-driven motility of a silica nano and micro-rod in a planar nematic cell (MLC 6608). Snapshots of cross polarized images with an additional  $\lambda$  plate of a moving (a-d) nano-rod and (e-h) micro-rod taken at varying electric field and a constant frequency, f = 50 Hz. Cell thickness,  $d = 10 \mu m$ . Field direction is perpendicular to the plane of the nematic cell.

field, the velocity of the nano-rod is larger than the micro-rod. The experimental data can be fitted to a non-linear equation given by

$$v = \mu_1(E - E_0) + \mu_3(E - E_0)^3$$
(5.2)

where  $E_0$  is the threshold field required to move the particles and  $\mu_1$  and  $\mu_3$  are the linear and 3rd order mobilities, respectively. The fit parameters are summarized in Table 5.1. This type of non-linear behaviour is a clear signature that the particles are charged. In case of non-charged spherical particles,  $v \propto E^2$ .

It is also observed that, the tilt angle increases with the electric field. We measured the tilt angle  $(\theta)$ , it is the angle between the nematic director and the long axis of the rod from the projection length with varying electric field (see Fig. 5.5(b)). When the field increases, we see an increase in tilt angle of the particle. It is observed that the rods starts tilting beyond a threshold voltage. The maximum tilt for a nano-rod is

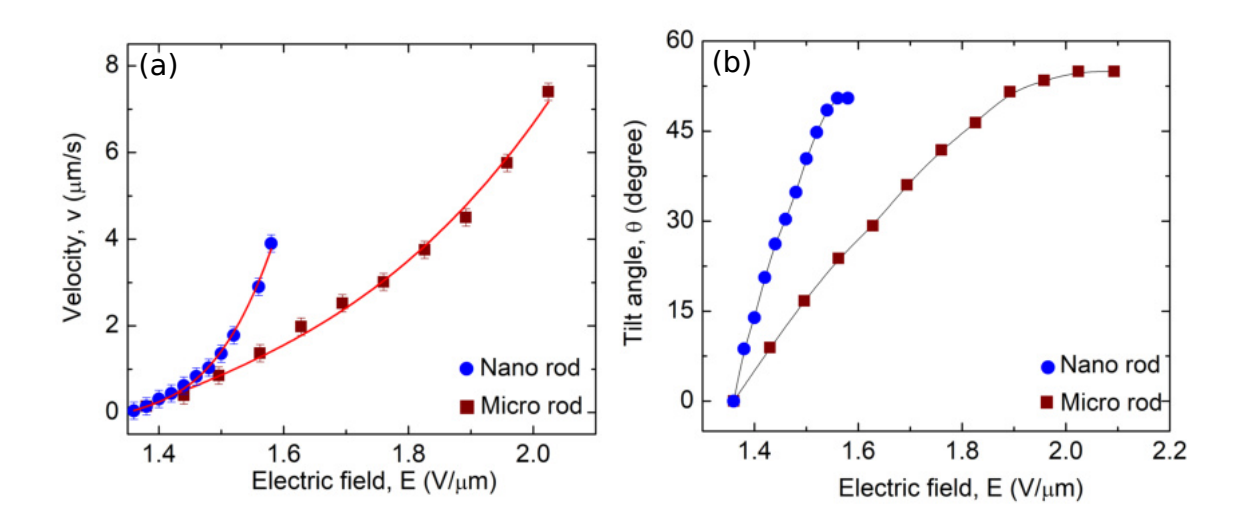


Figure 5.5: (a) Electrophoretic velocity v and (b) tilt angle variation with applied electric field in case of a nano-rod (blue circles) and micro-rod (red squares) in a planar cell of MLC-6608. The experiment was held at a fixed frequency, f = 50 Hz. Cell thickness,  $d = 10 \ \mu m$ . The red line is the least square fit to  $v = \mu_1 \ (E-E_0) + \mu_3 \ (E-E_0)^3$ . For nano-rod,  $E_0 = 1.34 \ V/\mu m$  and for micro-rod,  $E_0 = 1.38 \ V/\mu m$  are the threshold fields.

Particles	$\mu_1$	$\mu_3$
	$(\mu \mathrm{m}^2/\mathrm{V.s})$	$(\mu \mathrm{m}^2/\mathrm{V.s})$
Nano-rod	4.1	27.7
Micro-rod	5.5	11.2

Table 5.1: Summary of the fit parameters obtained from the fitting,  $v = \mu_1$  (E-E<sub>0</sub>) +  $\mu_3$  (E-E<sub>0</sub>)<sup>3</sup>.

48°. Similar behavior is observed for a micro-rod with a maximum tilt upto 53°. For a given field, nano-rods tilt more as compared to micro-rods.

Here the applied electric field has two contributions. Firstly, it creates a non-linear electrophoresis and secondly, it provides an electric torque; consequently the particle tilts along the electric field direction. Fig. 5.6 shows the simultaneous motility and tilt of nano and micro-rods with the field. The electric-field-induced torque can be

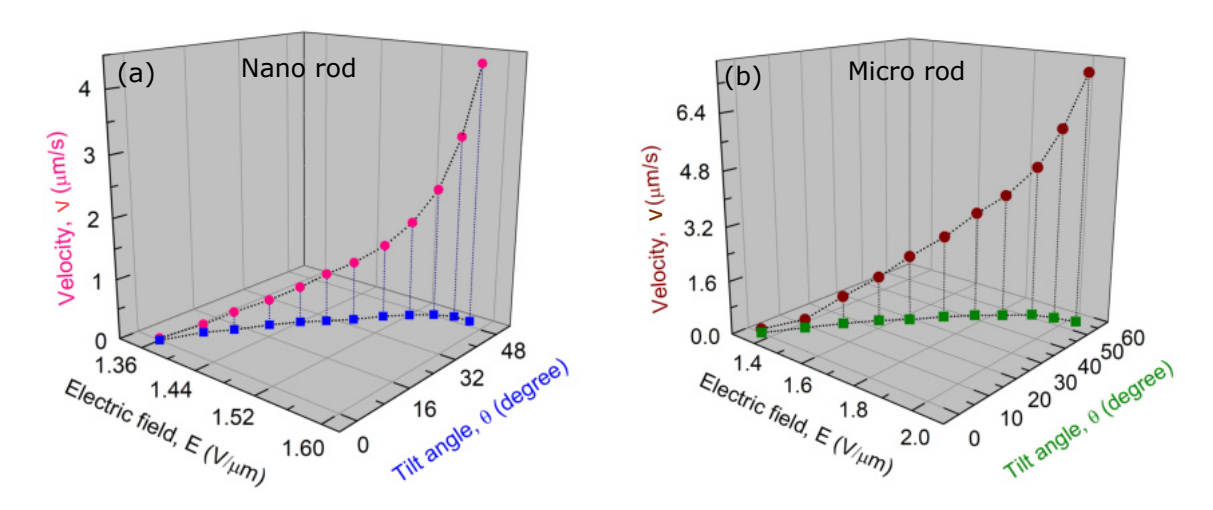


Figure 5.6: Field dependence of velocity (circles) and out of plane tilt (squares) of a (a) nano-rod and a (b) micro-rod in a planar nematic cell.

written as [6], 
$$\tau_{el} = \frac{1}{2} \triangle \lambda E^2 cos\theta sin\theta$$
 (5.3)

where  $\theta$  is the angle between the nematic director and the long axis of the particle.  $\Delta \lambda$  is the polarizability anisotropy of the particle.

The elastic energy of rod-like particles in a NLC is given by [7],

$$F = 2\pi C K \theta^2 \tag{5.4}$$

where  $C = \frac{L}{2} \log(L/d)$ . L and d being the length and the diameter of the particle.

The elastic torque can be written as,

$$\tau_{elas} = -\frac{\partial F}{\partial \theta} = -4\pi CK\theta \tag{5.5}$$

At equilibrium, the electric torque is balanced with the elastic torque as  $\tau_{el} + \tau_{elas}$ = 0 and we can write

$$\frac{\theta}{\cos\theta\sin\theta} = \left(\frac{\Delta\lambda}{8\pi CK}\right)E^2\tag{5.6}$$

Figure 5.7 shows the variation  $\theta/\cos\theta\sin\theta$  with  $E^2$ . The slope gives the constant in the first bracket of Eq. (5.6). Considering average Frank elastic constant of MLC-6608

sample is  $K = 13.9 \times 10^{-12}$  N and C is calculated to be  $C_{nano} = 2.1 \,\mu\text{m}$  and  $C_{micro} = 2.8 \,\mu\text{m}$ , respectively. By knowing the value of C and K, we calculate the polarizability anisotropy  $\Delta\lambda_{nano} = 1.17 \times 10^{-21} \,\text{C}^2\text{m/N}$  and  $\Delta\lambda_{micro} = 0.52 \times 10^{-21} \,\text{C}^2\text{m/N}$ . The polarizability anisotropy of the nano-rod is almost double as compared to the microrod. The L/d aspect ratio of the nano and micro-rod is 15 and 8 respectively, i.e., the aspect ratio is almost double. Hence the polarizability anisotropy is related to the aspect ratio of the rods as expected.

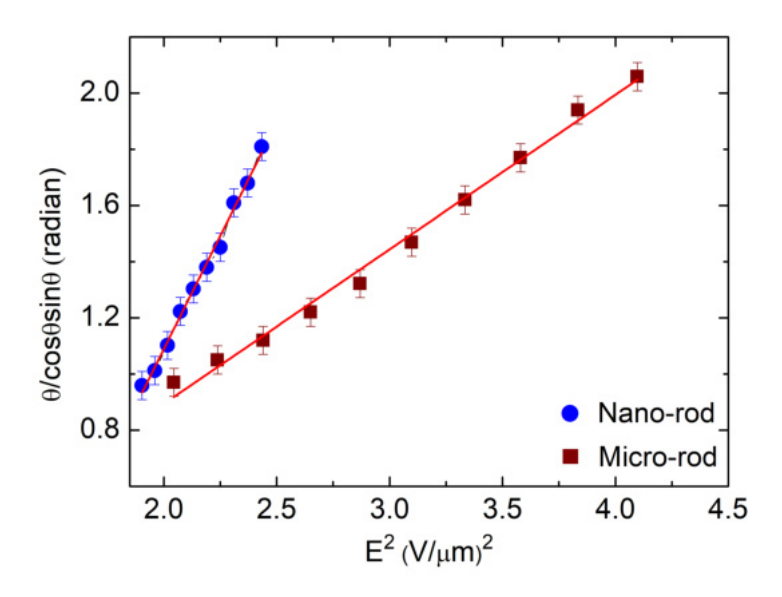


Figure 5.7: Variation of  $\theta/\cos\theta\sin\theta$  with  $E^2$  from the torque balance equation. Red lines are the best fit to Eq. (5.6). Cell thickness,  $d=8~\mu m$ .

Figure 5.8 shows the frequency dependence of transport velocities for both nano and micro-rods. According to the induced charge electrophoresis, the frequency dependence on velocity is given by [3,8]

$$V_{i}(\omega) = V_{i}^{o} \frac{\omega^{2} \tau_{e}^{2}}{(1 + \omega^{2} \tau_{p}^{2})(1 + \omega^{2} \tau_{e}^{2})}$$
(5.7)

where  $\omega = 2\pi f$ ,  $\tau_p = \lambda_D L/2D$  is the particle charging time and  $\tau_e = \lambda_D d/2D$  is the electrode charging time. The experimental data is fitted with Eq. (5.7), and the continuous red lines in Fig. 5.8 show the best fits to the data. The fit parameters are  $\tau_p$ =0.051 s and  $\tau_e$ =0.021 s for a nano-rod and  $\tau_p$ =0.049 s and  $\tau_e$ =0.017 s for a micro-rod. Frequency dependence of silica rods shows a general behaviour similar to

the spherical particles.

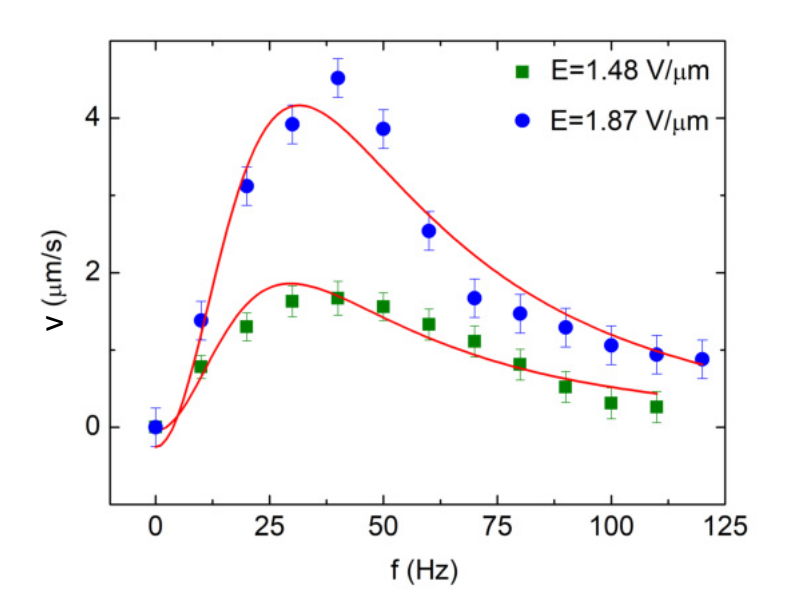


Figure 5.8: Variation of velocity as a function of frequency for a nano-rod at fixed field strengths,  $E = 1.48 \text{ V/}\mu\text{m}$  (green squares), and a micro-rod at  $E = 1.87 \text{ V/}\mu\text{m}$  (blue circles), respectively. Cell thickness,  $d = 10 \mu\text{m}$ . The continuous red lines are the best fits to Eq. (5.7).

#### 5.3.1 Optical control on the particle motility

We discuss the light-driven dynamics of rod-shaped silica particles in a NLC of negative dielectric anisotropy. We use dendrimers with azo component in their peripherals (azodendrimers), which act as a photoactive interface for liquid crystals. We obtain photo active surfaces without any surface pretreatment, only by mixing a small amount of azodendrimers in LC colloids. By UV irradiation, the orientation of the LC mesogens transform from homeotropic to planar (Fig. 5.9) [9,10]. Photo-driven anchoring transition via light-sensitive azodendrimers is shown in Fig. 5.9 (a). This leads to a change of a dipolar particle to boojum as shown in Fig. 5.9(b). We study the optical control on the motility of the silica nano-rods in nematic liquid crystal by irradiating UV light.

As we discussed in chapter-3, nano-rods have two types of orientation. We select a parallel nano-rod with dipolar defect configuration. When irradiated with the

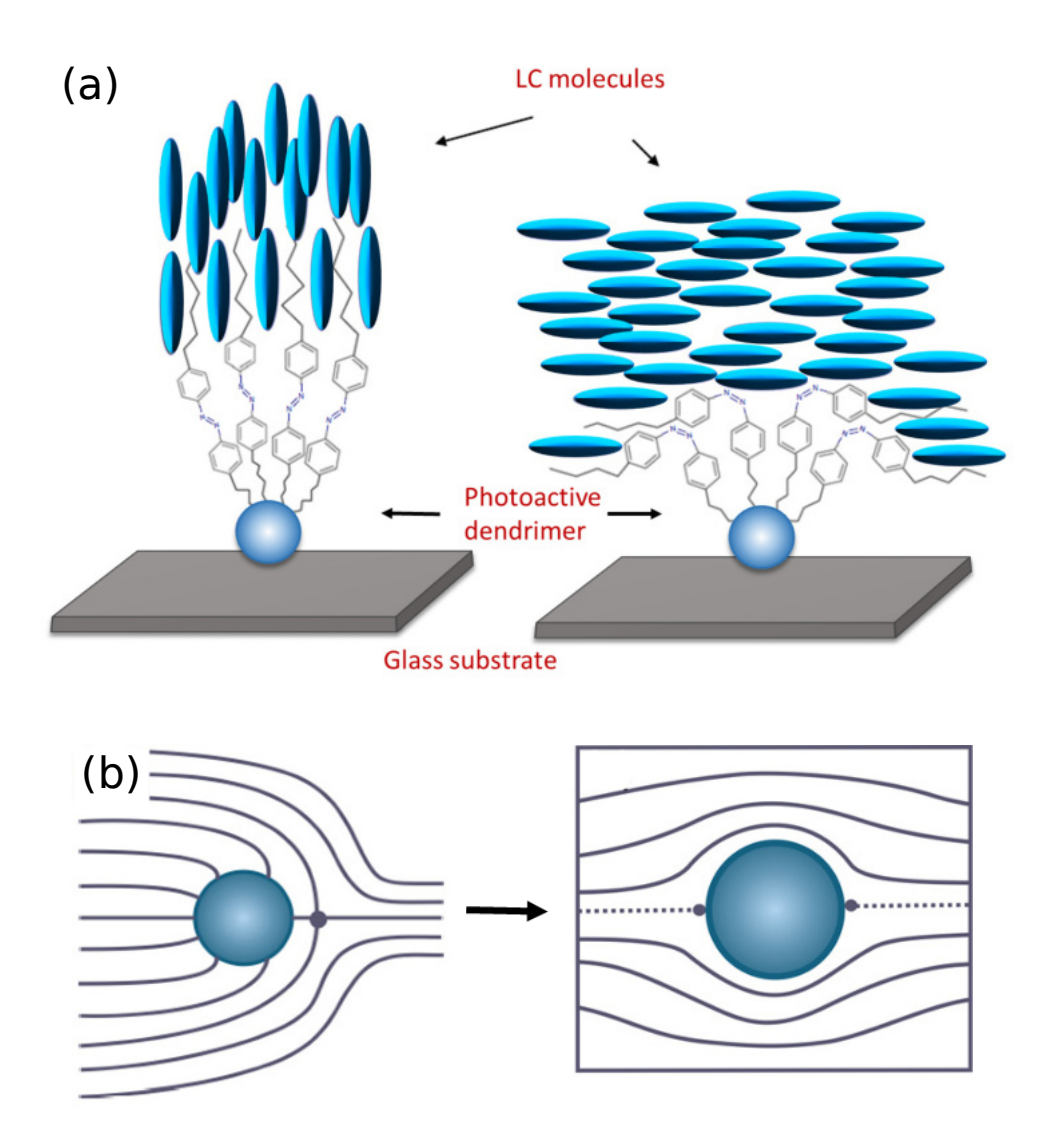


Figure 5.9: Surface action of photoactive azo-dendrimer: (a) Homeotropic to planar anchoring transition of LC molecules in planar nematic cell by irradiating UV light.

(b) Dipolar point defect associated with the spherical particle transforms into a boojum defect.

UV light, the director configuration on the surface of the nano-rod changes, namely homeotropic surface anchoring changes into a planar one. As a result, the nano-rod tilts vertically down, which is perpendicular to the nematic director as shown in Fig. 5.10(a-d). Because of its small size, the vertical orientation of the particle is not seen in POM. In such configuration, we expect a planar boojum defect associated with the nano-rod.

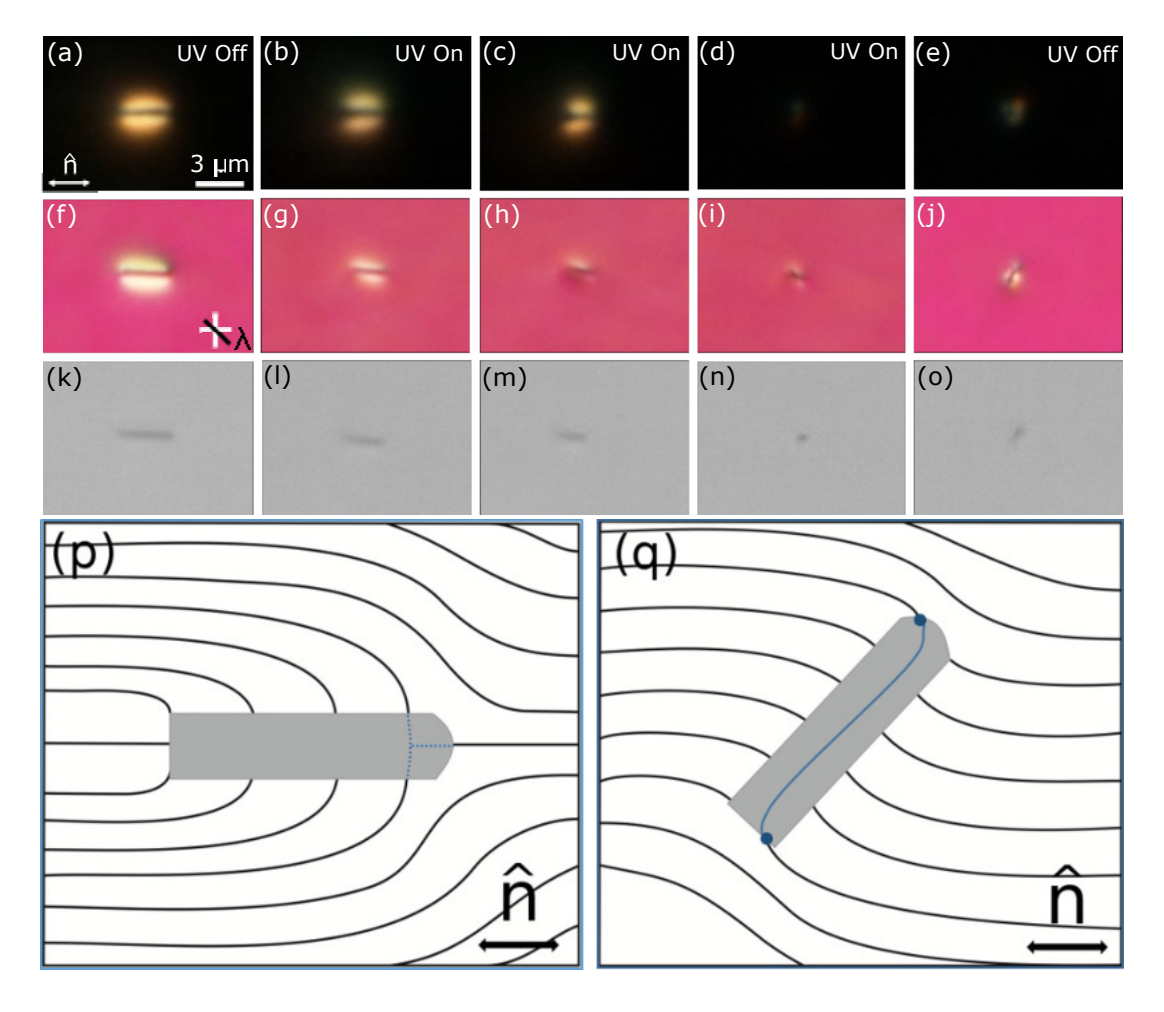


Figure 5.10: Initial and intermediate stages of a dipolar nano-rod during UV irradiation. The rod tilt out of plane under UV irradiation. Images were taken with (a-e) crossed polarizers, (f-j) an additional  $\lambda$ -plate and (k-o) without polarizers. Cell thickness is 12  $\mu$ m.

To understand the director reorientation, images were taken with an additional lambda-plate as shown in Fig. 5.10(f-j). The out-of-plane tilt of the nano-rod can be clearly seen in CCD images as shown in Fig. 5.10(n). When the UV light is

switched off, the planar anchoring on the particle transformed back into homeotropic, which results a quadrupolar configuration with a ring defect as shown schematically in Fig. 5.10(q). Fig. 5.10 (p & q) shows schematic representation of initial and final configuration of the nematic director before and after the UV irradiation.

Further, we studied the effect of UV light on moving nano-rods with applied ac electric field. The rods with dipolar configuration propels along the director transducing the energy of the field. Figure 5.11(a-d) shows a few snapshots of a propelling nano-rod and its reaction to UV light. As shown in Fig. 5.11(e), nano-rod tilts almost perpendicular to the cell when the UV light is switched on. Here, under UV irradiation, the dendrimer constituents cause the anchoring transition from homeotropic to planar. The nano-rods do not return to their original dipolar configuration when the UV light and the electric field are switched off. Here, the nano-rod is expected to have a Saturn ring configuration due to the reorientation of the director field, as discussed previously. When a field of strength 2 V/ $\mu$ m is applied, the nano-rod moves vertically down (perpendicular to the nematic director) as shown in Fig. 5.11(f-h). Thus, it is possible to change the direction of motion of a nano-rod by the electric as well as optical fields. We measure the velocity of a propelling nano-rod (perpendicular to the nematic director) with electric field strength, which is plotted in Fig. 5.12. It can be fitted to  $v = \mu_1 (E-E_0) + \mu_3 (E-E_0)^3$  given in Eq. (5.2), where the solid red curve is the best fit to the equation. Velocity increases non linearly when the field increases as expected, but the threshold field required to propel a tilted nano-rod is slightly higher  $(E_0 = 2 \text{ V}/\mu\text{m})$  than that of a parallel nano-rod (1.36 V/ $\mu$ m). The electrophoretic mobilities obtained from the non-linear fitting are  $\mu_1 = 0.72~\mu\text{m}^2/\text{ V.s}, \, \mu_3 = 0.51~\mu\text{m}^2/\text{ V.s}$ V.s and the threshold field,  $E_0 = 1.8 \text{ V}/\mu\text{m}$ . These mobilities are smaller than the mobilities of the parallel nano-rods (see Table 5.1). This could be due to change of the surface charge density of the particles and also the electrical properties of the LC due to the addition of azodendrimer.

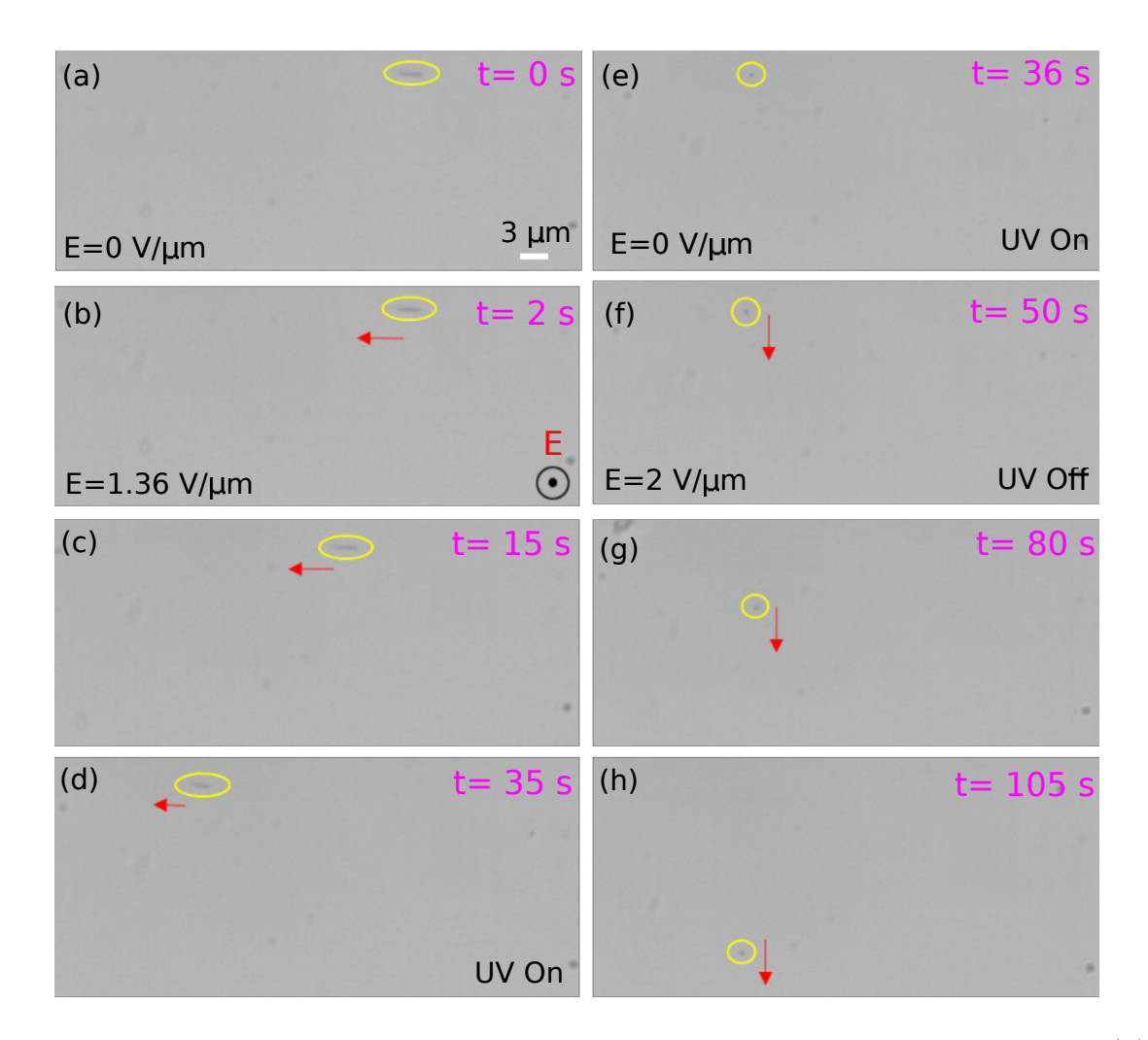


Figure 5.11: Motion of a nano-rod under ac electric field and UV irradiation. (a) CCD image of the nano-rod when the applied field is zero. The particles are encircled by yellow ellipses for clarity. (b-c) Snapshots of the nano-rod at different times at an applied field, E=1.36 V/ $\mu$ m and frequency, f=30 Hz. The electric field is directed out of the plane. (d-e) The effect of UV light switched on while the nano-rod is in motion. The nano-rod tilts out of plane and comes to a halt. (f-h) Sequence of images of the tilted nano-rod at applied field, E=2 V// $\mu$ m and frequency, f=30 Hz, when UV light is switched off.

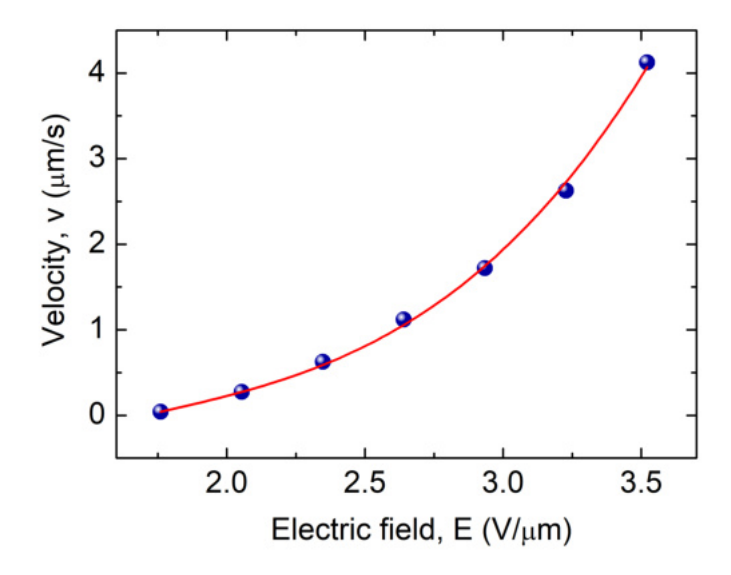


Figure 5.12: Field dependence of velocity of a nano-rod moves vertically down to the nematic director. The continuous red lines are the non-linear least square fitting to  $v = \mu_1 \ (E-E_0) + \mu_3 \ (E-E_0)^3$ . Fit parameters are  $\mu_1 = 0.72 \ \mu m^2 / V.s$ ,  $\mu_3 = 0.51 \ \mu m^2 / V.s$  and  $E_0 = 1.8 \ V/\mu m$ . Cell thickness is 12  $\mu m$ .

## 5.4 Conclusion

In conclusion, we studied the electrophoresis of charged silica rods in NLC. In planar aligned NLC cell with negative dielectric anisotropy, the electric field doesn't reorient the director, however the elongated rods propel along the director. The electrophoresis governing the motion is nonlinear due to the induced charges. Field dependent velocity has a linear and non-linear dependency. Our experiment shows that the applied electric field has two contributions. Firstly, it creates non-linear electrophoresis and secondly, it provides an electric torque; consequently the micro-rod tilts along the applied field direction. At a fixed electric field strength and frequency, we compare the velocity of a micro and a nano-rod and found that, a nano-rod propels faster as compared to a micro-rod. It is found that, polarizability anisotropy of the nano-rod is almost double as compared to a micro-rod, which can be related to the aspect ratio of the two particles. We further studied the optical control on colloidal nano-rods by introducing azodendrimers in nematic sample, which act as a photoactive interface for LC. It

#### 5.4. References

is observed that the nano-rods tilt about an axis perpendicular to the plane of the nematic cell under UV light irradiation. Such nano-rods further undergo a nonlinear electrophoresis when the UV light is switched off, but in a direction normal to the nematic director. Thus, we are able to change the direction of motion of the nano-rods using both electric and optical fields.

# References

- N. V. Solodkov, A. Saxena and J. Cliff Jones, Electrically driven rotation and nonreciprocal motion of microparticles in nematic liquid crystals. small, vol. 16, pp. 2003352, 2020.
- [2] O. D. Lavrentovich, *Transport of particles in liquid crystals*. Soft Matter. 10, pp. 1264-1283, 2014.
- [3] I. Lazo and O. D. Lavrentovich, Liquid-crystal-enabled electrophoresis of spheres in a nematic medium with negative dielectric anisotropy. Philos. Trans. R. Soc. A, vol. 371, pp. 20120255, 2013.
- [4] I. Lazo, C. Peng, J. Xiang, S. V. Shiyanovskii and O. D. Lavrentovich, Liquid crystal-enabled electro-osmosis through spatial charge separation in distorted regions as a novel mechanism of electrokinetics. Nat. Commun., vol. 5, pp. 5033, 2014.
- [5] M. V. Rasna, U. V. Ramudu, R. Chandrasekar and S. Dhara, Propelling and spinning of microsheets in nematic liquid crystals driven by ac electric field. Phys. Rev. E, vol. 95, pp. 012710, 2017.
- [6] M. V. Rasna, K. P. Zuhail, U. V. Ramudu, R. Chandrasekar and S. Dhara, Dynamics of electro-orientation of birefringent microsheets in isotropic and nematic liquid crystals. Phys. Rev. E, vol. 94, pp. 032701, 2016.
- [7] F. Brochard and P. G. de Gennes, Theory of magnetic suspensions in liquid crystals. J. Physics (Paris), vol. 31, pp. 691, 1970.
- [8] D. K. Sahu, S. Kole, S. Ramaswamy and S. Dhara, Omnidirectional transport and navigation of Janus particles through a nematic liquid crystal film. Phys.

#### References

- Rev. Res., vol. 2, pp. 032009(R), 2020.
- [9] A. Eremin et al., Optically driven translational and rotational motions of microrod particles in a nematic liquid crystal. PNAS, vol. 112, pp. 1716-1720, 2015.
- [10] A. Eremin et al., Azodendrimers as a photoactive interface for liquid crystals. Liq. Cryst., vol. 45, pp. 2121–2131, 2018.

6

# N-SmA-SmC phase transitions probed by a pair of elastically bound colloids

#### 6.1 Introduction

o far, we have studied the interaction and assembly of silica rods in nematic and chiral NLCs. When the particles are dispersed in a smectic liquid crystal, the situation is very different than when they are in nematic LC [1–5]. The SmA phase of the liquid crystal has translational order in addition to the orientational order of the molecules. The surface anchoring of the SmA layers at the colloid's surface is not well defined, and understanding the structure of the induced defects and interaction among the particles is incomplete. Recently Zuhail et al. have shown that the topological defects and anchoring in the SmA phase can be studied by dispersing the colloidal particles in the nematic phase of a liquid crystal that exhibits N-SmA phase transition [6-8]. In the nematic phase, the well-defined anchoring of the molecules on the surface of the particle guides the layer orientation and elastic deformation in the SmA phase around the colloids when cooled across the N-SmA phase transition. They also reported that, in the SmA phase the point defects in the nematic phase are transformed to focal conic line defects, and the elasticity of the medium controls the equilibrium separation between the particles. In the Smectic-C (SmC) phase, the molecules are tilted with respect to the layer normal, and due to the anisotropic fluctuations of the orientation of the long axes, it becomes weakly biaxial. Some theoretical and experimental studies of spherical particles in SmC/SmC\* liquid crystals have been reported, but mostly in free-standing films [9–13]. In this chapter, we present experimental studies on a pair of microsphere with planar and homeotropic surface anchoring across the N-SmA-SmC phase transitions. We shows that the temperature dependence of the equilibrium separation and the angle of the colloidal pair with respect to the far field director depend on the type of surface anchoring and are coupled to the elasticity and SmC order parameter.

## 6.2 Experimental

We used DMOAP coated silica spheres of diameter 5.2  $\mu$ m that provides homeotropic surface anchoring to the liquid crystal molecules. These microspheres were dispersed in a liquid crystal that exhibits the following phase transition temperature (Fig. 6.1): Cr 33.2  $^{0}$ C SmC 57.7  $^{0}$ C SmA 65.5  $^{0}$ C N 68  $^{0}$ C I. Also experiments were performed on microspheres coated with N-methyl-3 aminopropyl trimethoxy-silane (MAP) to induce planar anchoring of the molecules. Colloidal mixture was dispersed into a planar cell of thickness in the range of 11–14  $\mu$ m.

$$C_5H_{11}$$
  $OC_{10}H_{21}$ 

Cr 33.2°C SmC 57.7°C SmA 65.5°C N 68°C I

Figure 6.1: Molecular structure and phase transition temperatures of the compound.

We use a PID controller (Instec Inc.) with an accuracy of  $\pm 0.1$   $^{0}$ C. The trajectories of the particles as a function of temperature were video recorded using a 60X air objective (Nikon NIR Apo) with a CCD camera at 25 frames per second while the sample was cooled at the rate of 0.2  $^{0}$ C/min. The x-ray diffraction studies were carried out on unoriented samples by using Cu-K $\alpha$  radiation from a PANalytical instrument (DY 1042-Empyrean) and a linear detector (PIXcel 3D). The sample temperature

was controlled with a precision of 0.1  $^{0}$ C using a Linkam heater and a temperature controller. The molecular tilt angle ( $\theta$ ) was calculated from the temperature-dependent layer spacing across the SmA-SmC phase transition.

We used a fully automated adiabatic scanning calorimeter for heat capacity  $(C_p)$  measurements. The almost real thermal equilibrium state of the sample was achieved due to the high-temperature stability (50 mK) and the slow scanning rates. To get actual  $C_p$  of the sample, the heat capacity of the empty cell was measured in a separate experiment and subtracted from the measured data.

### 6.3 Results and discussion

To obtain the phase transition temperatures, we performed the heat capacity measurements by using a high-resolution ac calorimeter. Figure 6.2 shows the variation of specific heat as a function of temperature. It shows a first order N-SmA and second order SmA-SmC phase transitions.

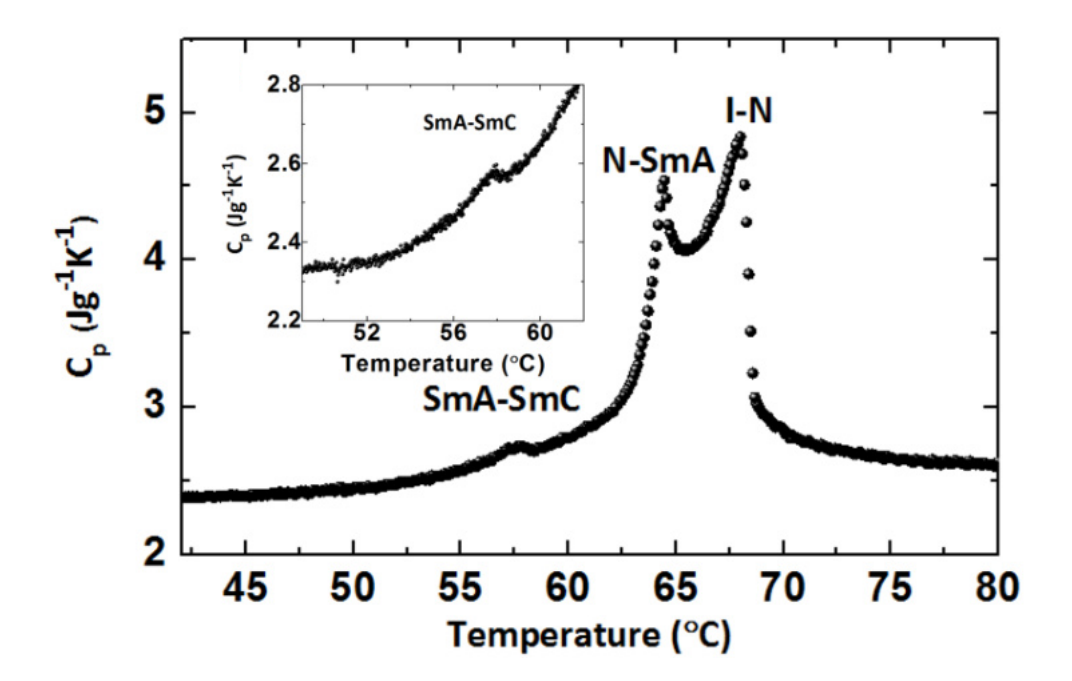


Figure 6.2: The specific heat capacity  $(C_p)$  measurement with fast cooling (0.7 K/h). (Inset) Slow cooling (0.12 K/h) across the SmA-SmC phase transition.

First we looked at the DMOAP coated spherical particles in the nematic phase. We

found that the colloids induce a Saturn ring defect (i.e., quadrupolar defect) irrespective of the cell thickness. This is in contrast with the observation in conventional liquid crystals such as 5CB or 8CB, where the defect usually depends on the cell confinement. As we already discussed in chapter-2, by using optical tweezers, it is possible to manipulate the particles and the defect associated with it. We converted a couple of particles to dipolar structure from quadrupolar and assembled a pair of elastic dipoles which are collinear (see Fig. 6.3(a)). We studied a pair of dipolar particles across the N-SmA-SmC phase transitions with the help of the temperature controller at a cooling rate of 0.2 °C/min. Figure 6.3 shows the defect transformation of a pair of dipoles across N-SmA-SmC phases. When the sample is cooled from the nematic to the SmA phase, the point defects are transformed into smectic focal line defects. Similar results were reported in 8CB liquid crystal by Zuhail et al [6]. It was shown that the transformation took place through the formation of a splay soliton at the expense of energy cost associated with elastic bend deformation. It is clear from the Fig. 6.3(b) that, the length of the defect line is extended up to several times the diameter of the particles. The homeotropic surface anchoring of the LC molecules in the SmA phase is retained only on the left-half part of the first particle (on the left side), and the anchoring is broken in the remaining part creating a strong layer distortion around the particle. Images were taken with a  $\lambda$ -plate to understand the molecular orientation around defect (Figs. 6.3(d-f)). The yellow and blue colours on the upper and lower sides of the line defect indicate that LC molecules are rotated clockwise below and anti-clockwise above the spherical particles.

As shown in Fig. 6.3(f), there is strong layer distortion surrounding the microspheres in the SmC phase. This could arise due to the random variation of tilt angle direction of the LC molecules and the weak biaxiality of SmC phase [14]. The length of the defect line in the SmC phase has reduced compared to that of the SmA phase, also the separation between the centre of microspheres is changed in three different phases [Figs. 6.3(g-i)]. To have better understanding, we define an extrapolation length l = W/B, where W and B are the surface anchoring energy and elastic layer compressional modulus of the smectics, respectively. In the SmA phase [15,16],  $W \sim 10^{-2}-10^{-3} \text{ J/m}^3$  and  $B \sim 10^5-10^6 \text{ J/m}^3$  and estimated  $l \sim 0.1 \ \mu\text{m}$ , which is much smaller than the size of the colloids. Thus strong surface anchoring guides the transformation of the defect

across the phase transition.

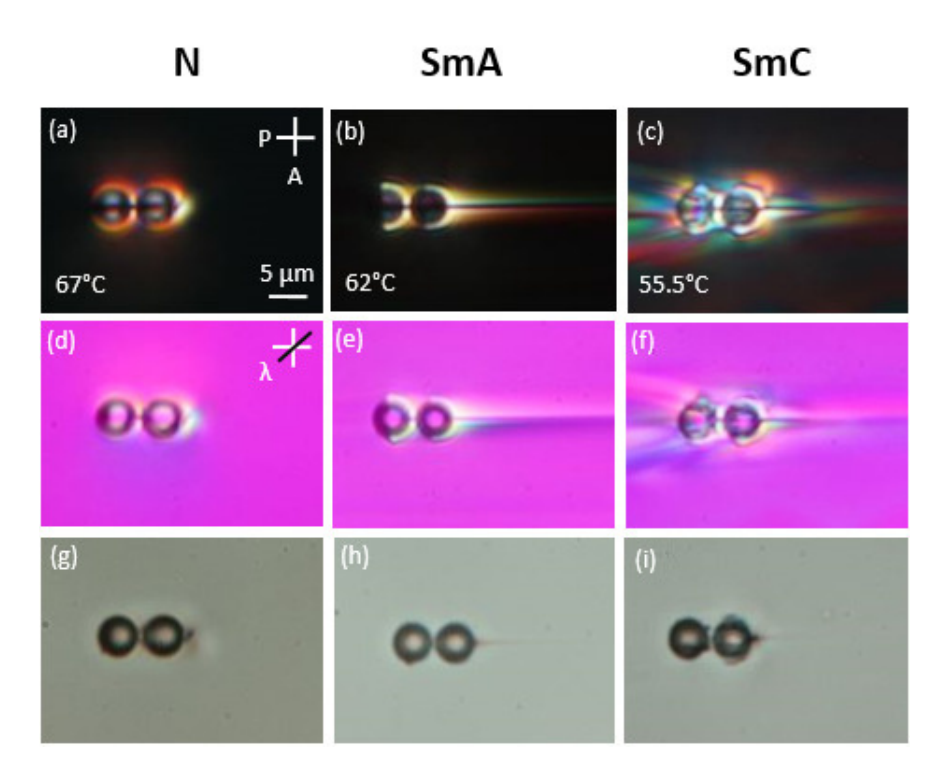


Figure 6.3: Experimental optical photomicrographs of a pair of microspheres with homeotropic surface anchoring at different temperatures in a planar cell. Images are taken (a-c) with crossed polarizers, (d-f) with an additional  $\lambda$ -plate, and (g-i) without polarizers. Diameters of the particles and cell thickness are 5.2  $\mu$ m and 14  $\mu$ m, respectively.

We measured the interparticle separation (D) across the N-SmA-SmC phase transitions as a function of temperature while cooling the sample at the rate of 0.2  $^{0}$ C/min as shown in Fig. 6.4(a). In the nematic phase, D increases linearly followed by almost a discontinuous change at the N-SmA phase transition. The increase in the ratio of the bend to splay elastic constant has recently been used to describe the pretransitional behaviour of D. It has been shown that D can be written as [6],

$$D/D_0 \simeq 2.439 + 0.0878(1 - K_{11}/K_{33}) \tag{6.1}$$

where  $D_0$  is the separation at  $T=T_{NA}$  and  $(1 - K_{11}/K_{33})$  is the elastic anisotropy. Thus the pre-smectic separation increases due to rapid increase in  $K_{33}$  compared to  $K_{11}$ . Since the equilibrium separation is governed by the elasticity of the medium, the discontinuity in D marks the discontinuity of the elastic constants of the respective

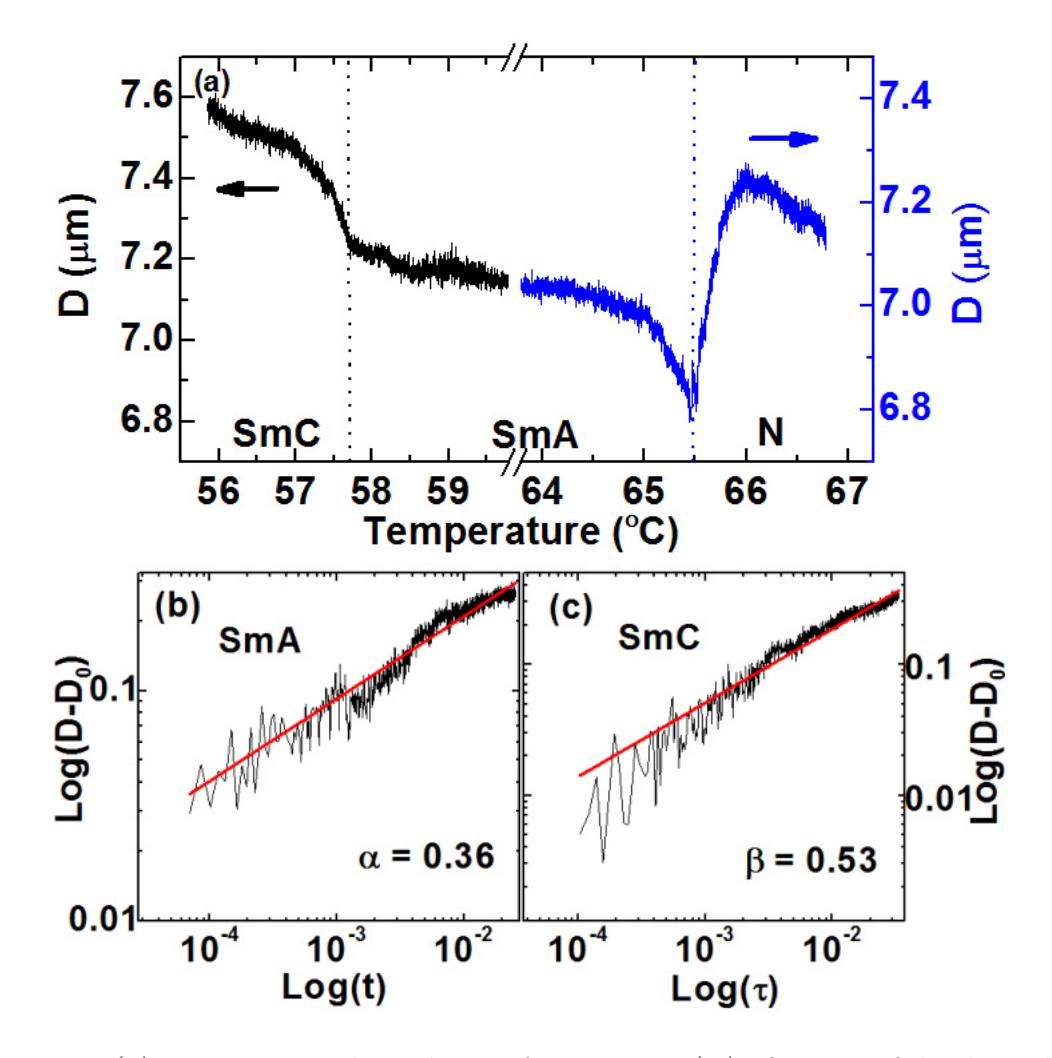


Figure 6.4: (a) Temperature dependence of separation (D) of a pair of dipolar colloids across the N-SmA-SmC phase transitions. Temperature variation of D below (b) the N-SmA and (c) the SmA-SmC phase transition in logarithmic scale. The red lines are the best fits to the power laws:  $(D-D_0) \sim t^{\alpha}$ , with an exponent  $\alpha = 0.36$ , where  $t=(1-T/T_{NA})$  and  $(D-D_0) \sim \tau^{\beta}$ , with an exponent  $\beta = 0.53$ , where  $\tau = (1-T/T_{AC})$ . Cell thickness is 14  $\mu$ m and the diameter of the microsphere is 5.2  $\mu$ m. The sample was cooled at a rate of 0.2  $^{0}$ C/min.

phases. At the N-SmA transition  $(T_{NA})$ , the distance of closest approach between the particles is  $D_0 = 6.8 \mu \text{m}$ , which is around 1.6  $\mu \text{m}$  larger than the center-to-center distance between the two particles (5.2  $\mu$ m). This means that there are about 800 layers present between them at the transition, assuming the length of a molecule is about 2 nm. D continues to increase below the N-SmA transition. The temperature dependence of D -  $D_0$ , just below the N-SmA transition is shown in Fig. 6.4(b) using a logarithmic scale. It shows a power law dependence,  $(D - D_0) \sim t^{\alpha}$ , with an exponent of  $\alpha$ =0.36, where  $t=(1-T/T_{NA})$ . In the case of 8CB liquid crystal, a similar exponent was also obtained. The opposite tilting of the molecules causes an angle discontinuity across the focal line in the SmA phase. A schematic diagram of the focal conic line is presented (see Fig. 6.5(b)). A schematic diagram of a colloidal pair in the nematic phase is also shown in Fig. 6.5(a) for comparison. In Fig. 6.5(b), the blue region around the particles denotes the area where the homeotropic anchoring is broken to reconcile with the far field director. The layer dilation caused by the angle discontinuity is given by  $d_d$  -  $d_0$ , where  $d_d$  and  $d_0$  are the thickness of the dilated and undilated layers, respectively [2, 17]. As a result, the elastic energy  $B(1-d_d/d_0)^2$  increases where B is the SmA elastic compression or dilation modulus. Below the N-SmA transition, the elastic modulus varies as  $B \sim t^{0.38}$  [6]. If the discontinuity angle exceeds a critical value, it may further create edge dislocations in the confined region [18]. In the present system the length of the defect line increases and the colloidal particles are pushed apart, thereby increasing the center-to-center separation.

As the temperature is decreased in the SmA phase (nearly 5  $^{0}$ C below the N-SmA transition temperature) D increases slowly till the SmA-SmC transition temperature is reached (Fig. 6.4(a)). For example, the slope between 60  $^{0}$ C and 57.7  $^{0}$ C is very small. At the transition point ( $T_{AC} = 57.7 \,^{0}$ C), D sharply changes slope and increases continuously as the temperature is decreased. For example, at the SmA-SmC transition temperature,  $D = 7.2 \,\mu\text{m}$ , and when the temperature is reduced to 56  $^{0}$ C, it increases to 7.6  $\mu$ m. The calorimetry study shows that the N-SmA and SmA-SmC phase transitions are weakly first order and second order, respectively. The temperature dependence of D appears to be a pointer to the discontinuous and continuous phase transitions. Using a logarithmic scale, we display the temperature variance of D -  $D_0$  in the SmC phase in Fig. 6.4(c). We could fit to a power law, (D- $D_0) \sim \tau^{\beta}$ ,

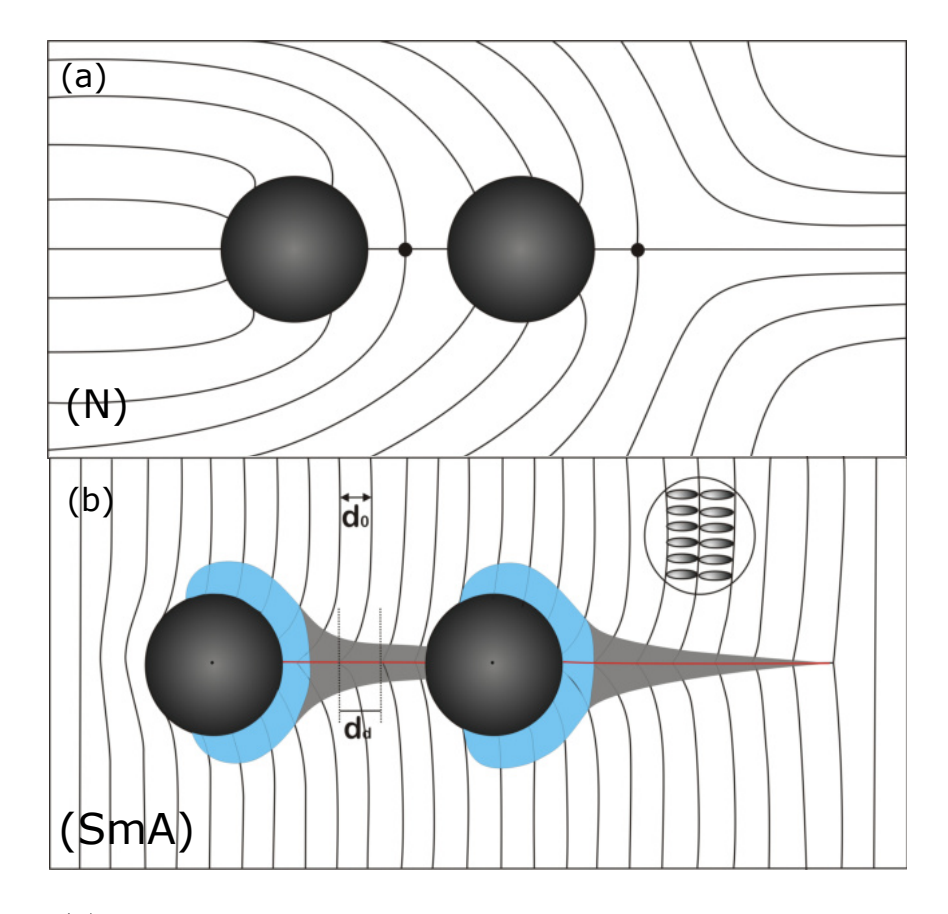


Figure 6.5: (a) Schematic diagrams of two collinear colloids in the nematic phase with homeotropic surface anchoring. The continuous lines represent the director field. (b) Schematic diagram showing the layer distortion and focal conic line around the colloid pair in the SmA phase. The continuous lines represent SmA layers. Orientation of a few molecules within the layers is shown inside the circle in the upper right-hand corner. The blue regions indicate the breaking of homeotropic anchoring. The red line represents the focal conic line. The gray regions represent the deviation (or distortion) of the layers from the uniform orientation.  $d_d$  and  $d_0$  are the thickness of the dilated and undilated layers, respectively.

with an exponent  $\beta = 0.53$ , where  $\tau = (1-T/T_{AC})$ . The de Gennes theory suggests that the SmA-SmC phase transition belongs to the 3D XY universality class, but several experiments revealed a classic mean-field behaviour with the tilt angle  $\theta$  is an order parameter which is given by  $\theta = \theta_0 |\tau|^{\eta}$ , where  $\eta = 0.5$ . We used X-ray diffraction studies to test the temperature dependence of  $\theta$ , and the data is shown in Fig. 6.6(a). The exponent of the temperature dependent order parameter obtained from the fitting [Fig. 6.6(b)] is  $\eta = 0.48$ , and it is very close to the exponent  $\beta = 0.53$  of the temperature dependence of D (Fig. 6.4(c)). We hypothesise that the interparticle separation D is related to the order parameter ( $\theta$ ) of the SmA-SmC phase transition. It is worth noting that a number of physical properties, such as the birefringence and elastic modulus of SmA phase also show the strong pretransitional behaviour across the SmA to SmC (or SmC\*) phase transition [19–22].

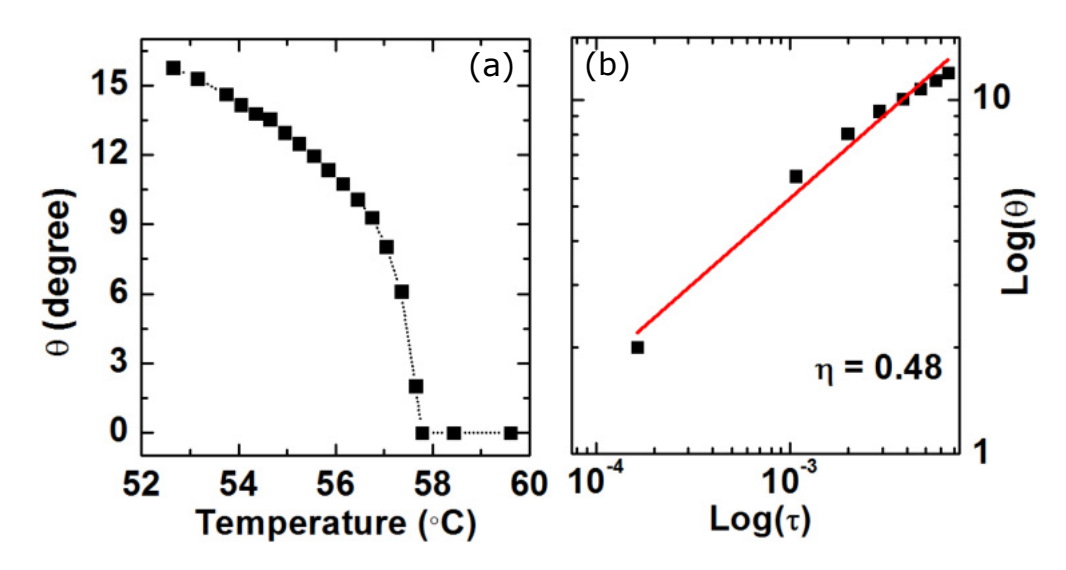


Figure 6.6: (a) Temperature variation of tilt angle ( $\theta$ ) below the SmA-SmC phase transition. (b) Variation of  $\theta$  with reduced temperature below the SmA-SmC transition (logarithmic scale) and the best fit to the equation  $\theta = \theta_0 |\tau|^{\eta}$  with an exponent  $\eta = 0.48$ .

When colloidal particles with planar anchoring (MAP caoted) are introduced in a planar cell, each particle creates a pair of antipodal surface defects known as boojums. Figure 6.7 shows representative optical images of a pair of particles with boojums, and the transformation of the boojums across the N-SmA-SmC phase transitions. The

transformation of boojums across the N-SmA phase has been studied by Zuhail et al. recently [8]. In the SmA phase, the boojums are transformed into two line defects which are extended on the opposite sides of the pair along the rubbing direction up to several micrometers. Images captured using  $\lambda$ -plate [Figs. 6.7(d-f)] clearly indicate that the SmA layers are tilted in the opposite direction of the defect lines. Figs. 6.7(j) and 6.7(k) display schematic representation of the director distortion around the colloidal pair in N as well as SmA phases. It is observed from the images that, in both the SmA and SmC phases, with homeotropic surface anchoring, the focal conic lines are collinear along a particular side (Fig.6.3 (b,c)). While in planar anchoring, they are formed along both sides but collinear. The nonuniform coloured regions around the particles in the SmC phase suggest that the layers are skewed randomly (Fig. 6.7(c)). This may be due to the weak biaxiality of the SmC phase, which we mentioned previously (Fig. 6.3(c)). Furthermore, compared to the SmA phase, the defect lines have become shorter and less distinct [Fig. 6.7(i)]. This indicates that the angle discontinuity in the SmC phase has decreased in comparison to the SmA phase.

To see the effect of phase transition on the interparticle separation, we measured separation D across the N-SmA-SmC phase transitions as a function of temperature (Fig. 6.8(a)). At the N-SmA phase transition ( $T_{NA} = 65.5$   $^{\circ}$ C), the interparticle separation D decreases very sharply, followed by a slope change. It becomes temperature independent in the SmA phase and across the SmA-SmC transition. There is no discernible change in D across the SmA-SmC phase transition, in comparison to the particles with homeotropic anchoring (see Fig. 6.4(a)). Since the line defects in the SmA and SmC phases between the two particles are not collinear, the colloids are not pushed apart unlike in the previous case [see Figs. 6.3(b) and 6.3(c)], hence D remains constant. This suggests that the temperature dependence of D depends on how two particles are bound by defects. The line connecting the center-to-center separation of the microsphere forms an angle  $\phi$  with respect to the far field director. We calculated  $\phi$  as a function of temperature to see the effect of phase transitions on it, as shown in Figs. 6.8(b) and 6.8(c). The angle  $\phi$  decreases discontinuously across the N-SmA and decreases continuously across SmA-SmC phase transitions. For example, at the N-SmA transition (Fig. 6.8(c)),  $\phi$  discontinuously decreases from 36  $^{0}$  to 26  $^{0}$ . Across the SmA-SmC transition (Fig. 6.8(b))  $\phi$  decreases continuously with a change of slope

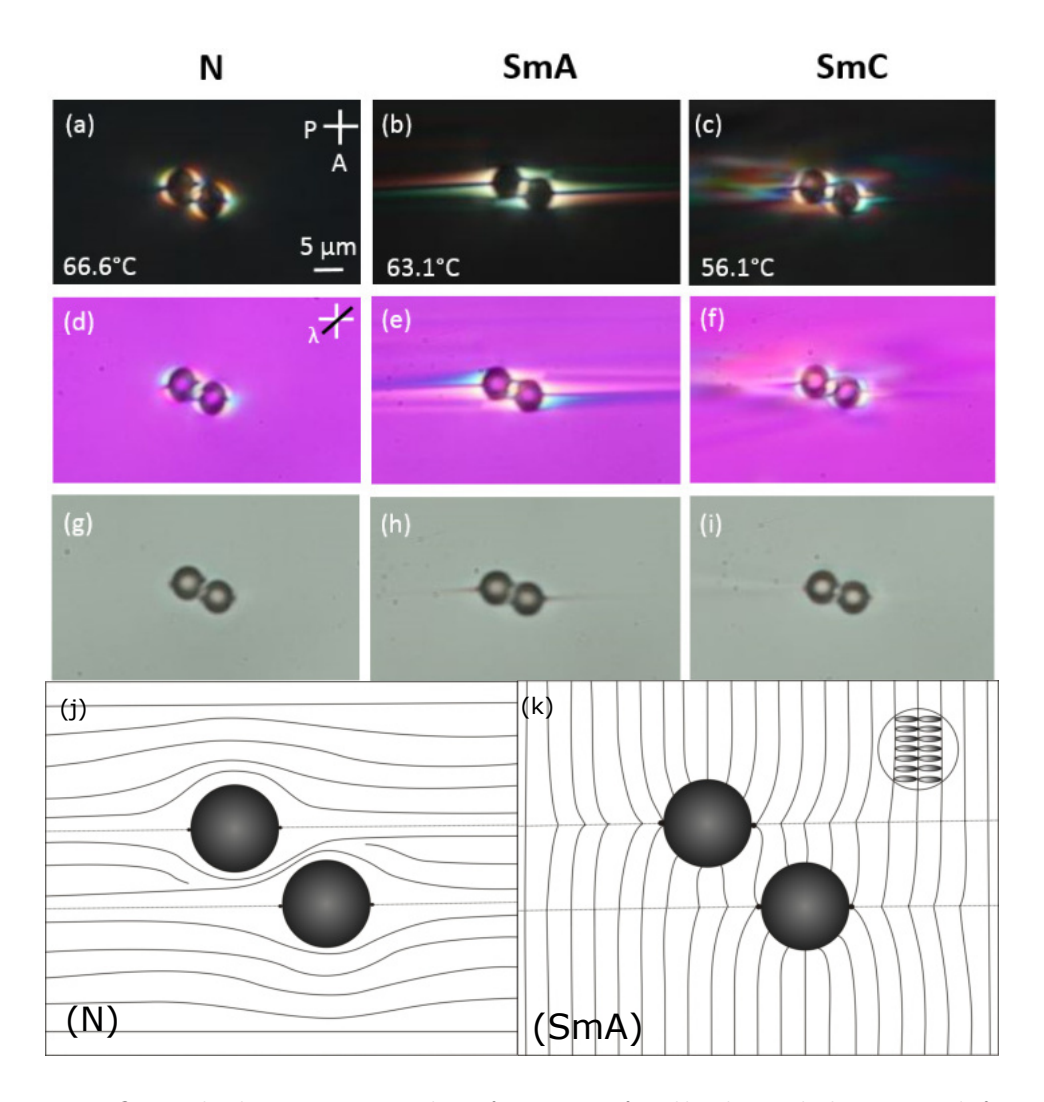


Figure 6.7: Optical photomicrographs of a pair of colloids with boojums defects in a planar cell at different temperatures in the N, SmA, and SmC phases in a planar cell. Images are taken (a-c) with crossed polarizers, (d-f) with crossed polarizers and a  $\lambda$ -plate, and (g-i) without polarizers. The diameters of the colloids and the cell thickness are 5.2  $\mu$ m and 11.5  $\mu$ m, respectively. (j) Schematic diagram showing the director field around two colloids with planar anchoring in the nematic phase. (k) Schematic diagram showing layer orientation in the SmA phase.

at the phase transition temperature (57.7 °C).

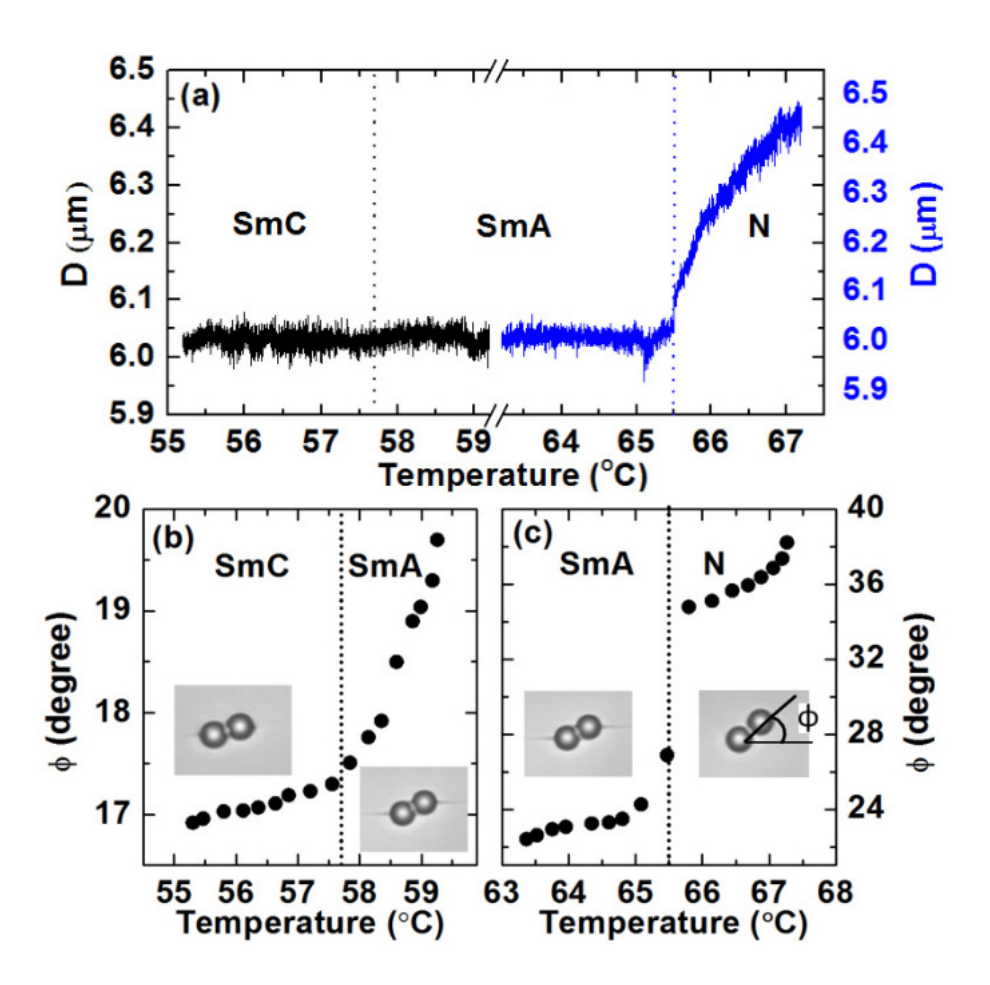


Figure 6.8: (a) Temperature dependence of center-to-center separation (D) of a pair of particles with planar anchoring in a planar cell. Temperature variation of  $\phi$  across the (b) SmA-SmC and (c) N-SmA phase transitions.  $\phi$  is the angle between the far field director and the joining line between the two centers of the particles (shown in inset). The sample was cooled at a rate of 0.2 °C/min. The diameters of the particles and the cell thickness are 5.2  $\mu$ m and 11.5  $\mu$ m, respectively.

In the case of homeotropic surface anchoring, D is sensitive to both the N-SmA and SmA-SmC phase transition. When it comes to planar surface anchoring, D is sensitive only to N-SmA transition, whereas  $\phi$  is sensitive to both the N-SmA and SmA-SmC phase transitions. The structural change that directly affects the colloidal pair across the SmA-SmC transition is the molecular tilt angle  $(\theta)$ , which is the order parameter of the SmA-SmC phase transition. Therefore, it is expected that the relative variation of D and  $\phi$  across the phase transitions is connected to the order parameters of the

respective phase transitions. Theoretical and computer simulation studies could be useful for understanding the direct link of these physical quantities.

#### 6.4 Conclusion

We have studied a pair of spherical colloids with homeotropic and planar surface anchoring across N-SmA-SmC phase transitions. The hyperbolic point defect is transformed to a smectic focal line below the N-SmA transition. The line defect is slightly shortened without any significant change in the structure below the SmA-SmC transition. The temperature dependence of the interparticle separation of a pair of collinear colloids shows a similar power-law as that of SmA-SmC order parameter. For colloids with planar surface anchoring there is no observable change in the interparticle separation across the SmA-SmC transition, although the angle made by the joining line with respect to the far field director decreases continuously with a characteristic slope change. This suggests that the interparticle separation of a pair of colloids and their orientation angle are coupled to the order parameters of the phase transitions.

#### References

- S. P. Schlotthauer, V. M. Turrion, C. K. Hall, M. G. Mazza and M. Schoen, The impact of colloidal surface-anchoring on the smectic A phase. Langmuir, vol. 33, pp. 2222–2234, 2017.
- [2] C. Blanc and M. Kleman, *The confinement of smectics with a strong anchoring*. Eur. Phys. J. E, vol. 4, pp. 241-251, 2001.
- [3] M. J. Gim, D. A. Beller and D. K. Yoon, Morphogenesis of liquid crystal topological defects during the nematic-smectic A phase transition. Nat. Commun., vol. 8, pp. 15453, 2017.
- [4] R. Pratibha, W. Park and I. I. Smalyukh, Colloidal gold nanosphere dispersions in smectic liquid crystals and thin nanoparticle-decorated smectic films. J. Appl. Phys., vol. 107, pp. 063511, 2010.
- [5] C. Bohley and R. Stannarius, Energetics of 2D colloids in free-standing smectic-C films. Eur. Phys. J. E, vol. 20, pp. 299-308, 2006.
- [6] K. P. Zuhail, P. Sathyanarayana, D. Seč, S. Čopar, M. Škarabot, I. Muševič and S. Dhara, Topological defect transformation and structural transition of twodimensional colloidal crystals across the nematic to smectic-A phase transition. Phys. Rev. E, vol. 91, pp. 030501(R), 2015.
- [7] K. P. Zuhail, S. Čopar, I. Muševič and S. Dhara, Spherical microparticles with Saturn ring defects and their self-assembly across the nematic to smectic-A phase transition. Phys. Rev. E, vol. 92, pp. 052501, 2015.
- [8] K. P. Zuhail and S. Dhara, Temperature dependence of equilibrium separation and lattice parameters of nematic boojum-colloids. Appl. Phys. Lett., vol. 106,

- pp. 211901, 2015.
- [9] C. Bohley and R. Stannarius, *Inclusions in free standing smectic liquid crystal films*. Soft Matter, vol. 4, pp. 683–702, 2008.
- [10] M. Tasinkevych and D. Andrienko, Colloidal particles in liquid crystal films and at interfaces. Cond. Mat. Phys., vol. 13, pp. 33603, 2010.
- [11] M. Tasinkevych, N. M. Silvestre and M.M. Telo da Gama, Liquid crystal boojumcolloids. New. J. Phys., vol. 14, pp. 073030, 2012.
- [12] P. Cluzeau, P. Poulin, G. Joly and H. T. Nguyen, Interactions between colloidal inclusions in two-dimensional smectic-C\* films. Phys. Rev. E, vol. 63, pp. 031702, 2001.
- [13] P. V. Dolganov and V. K. Dolganov, Director configuration and self-organization of inclusions in two-dimensional smectic membranes. Phys. Rev. E, vol. 73, pp. 041706, 2006.
- [14] P. G. de Gennes, The Physics of Liquid Crystals. Oxford University Press, Oxford, 2nd ed., 1993.
- [15] M. Benzekri, J. P. Marcerou, H. T. Nguyen and J. C. Rouillon, Critical behavior of the layer compressional elastic constant B at the smectic-A-nematic phase transition. Phys. Rev. B, vol. 41, pp. 9032-9037, 1990.
- [16] Z. Li and O. D. Lavrentovich, Surface anchoring and growth pattern of the field-driven first-order transition in a smectic-A liquid crystal. Phys. Rev. Lett., vol. 73, pp. 280-283, 1994.
- [17] C. Blanc and M. Kleman, Curvature walls and focal conic domains in a lyotropic lamellar phase. Eur. Phys. J. B, vol. 10, pp. 53-60, 1999.
- [18] J. Jeong and M. W. Kim, Confinement-induced transition of topological defects in smectic liquid crystals: from a point to a line and pearls. Phys. Rev. Lett., vol. 108, pp. 207802, 2012.

- [19] J. Fernsler, D. Wicks, D. Staines, A. Havens and N. Paszek, Birefringence suppression near the smectic A-smectic C phase transition in de Vries-type liquid crystals. Liq. Cryst., vol. 39, pp. 1204-1215, 2012.
- [20] M. Škarabot, K. Kočevar, R. Blinc, G. Heppke and I. Muševič, Critical behavior of birefringence in the smectic-A phase of chiral smectic liquid crystals. Phys. Rev. E, vol. 59, pp. R1323(R), 1999.
- [21] S. Shibahara, J. Yamamoto, Y. Takanishi, K. Ishikawa and H. Takezoe, Critical fluctuations at the untilted-tilted phase transition in chiral smectic liquid crystals. Phys. Rev. E, vol. 62, pp. R7599(R), 2000.
- [22] S. Shibahara, J. Yamamoto, Y. Takanishi, K. Ishikawa, H. Takezoe and H. Tanaka, Critical behavior of layer compression modulus near the Smectic-A-Smectic- $C_{\alpha}$ \* transition. Phys. Rev. Lett., vol. 85, pp. 1670-1673, 2000.

#### **Publications**

#### Thesis publications:

- N-SmA-SmC phase transitions probed by a pair of elastically bound colloids.
   Muhammed Rasi M., K. P. Zuhail, Arun Roy and Surajit Dhara.
   Physical Review E 97, 032702 (2018).
- Colloidal analogues of polymer chains, ribbons and 2D crystals employing orientations and interactions of nano-rods dispersed in a nematic liquid crystal.
   Muhammed Rasi M., Ravi Kumar Pujala and Surajit Dhara.
   Scientific Reports 9, 4652 (2019).
- Interactions of charged microrods in chiral nematic liquid crystals.
   Muhammed Rasi M., Ravi Kumar Pujala, Sathyanarayana Paladugu and Surajit Dhara.
   Physical Review E 104, 014706 (2021).
- Electrophoretic mobility of silica micro and nano-rods in nematic liquid crystals.
   Muhammed Rasi M., Ravi Kumar Pujala and Surajit Dhara.
   (Manuscript under preparation).

## Conferences and workshops attended:

#### **International:**

- 1. Attended International Complex Fluids Conference (Comp-Flu-2016 December) at IIIT Hyderbad.
- 2. Attended International Complex Fluids conference (CompFlu-2017 (December)) and presented a **poster** entitled "N-SmA-SmC phase transitions probed by a pair of elastically bound colloids" held at IIT Madras, Chennai.
- 3. Attended International Complex Fluids conference (CompFlu-2019 (December)) and presented a **poster** entitled "Colloidal analogues of polymer chains, ribbons and 2D crystals employing orientations and interactions of nano-rods dispersed in a nematic liquid crystal" held at IISER Bhopal, India.
- 4. Attended International Complex Fluids conference (Complex Fluids-2020 (December)) and presented a **poster** entitled "Bound state and hydrodynamic interaction of microrods in chiral nematic liquid crystals" held online conducted by IIT Bombay, India.

#### **National:**

- 1. Attended FIP (Frontiers in Physics)-2016 at School of Physics, UoH, Hyderabad.
- 2. Attended National Conference on "Physics at Small Scales and Advanced Materials" at University of Hyderabad, Hyderabad September 2017 and presented

- a **poster** entitled "N-SmA-SmC phase transitions probed by a pair of elastically bound colloids".
- 3. Attended Workshop on "Soft and Active Matter" at School of Physics, University of Hyderabad, Hyderabad February 2018 and presented a **poster** entitled "Colloidal analogues of polymer chains, ribbons and 2D crystals employing orientations and interactions of nano-rods dispersed in a nematic liquid crystal".

#### Brief biodata:

#### **Contact:**

Muhammed Rasi. M
Soft matter Lab
School of Physics
University of Hyderabad
Gachibowli, Hyderabad, India - 500046

Email: muhammed.rasi00@gmail.com

#### **Achievements:**

- 1. Qualified CSIR-NET (Physics)-2014 December
- 2. Qualified GATE-2015 with all India rank 685.
- 3. Awarded CSIR-SRF (DIRECT)-February 2019.
- 4. Awarded **Best Poster Award** at "International Complex Fluids conference (CompFlu-2019)", held at IISER Bhopal, India.

# Interaction, directed assembly and electrophoretic mobility of silica micro and nano-rods in nematic liquid crystals

by Muhammed Rasi M

**Submission date:** 15-Nov-2021 02:48PM (UTC+0530)

**Submission ID:** 1703261770

File name: Muhammed Rasi-final thesis.pdf (3.29M)

Word count: 28660 Character count: 142222 Dr. Surajit Dhara
Professor
School of Physics
University of Hyderabad
Hyderabad-500 046, INDIA.

Interaction, directed assembly and electrophoretic mobility of silica micro and nano-rods in nematic liquid crystals

ORIGINALITY REPORT

SIMILARITY INDEX

INTERNET SOURCES

**PUBLICATIONS** 

STUDENT PAPERS

**PRIMARY SOURCES** 

Muhammed Rasi M., Ravi Kumar Pujala, Sathyanarayana Paladugu, Surajit Dhara. "Interactions of charged microrods in chiral nematic liquid crystals", Physical Review E, 2021

Publication

Dr. Surajit Dhara Professor School of Physics University of Hyderabad Hyderabad-500 046. INDIA.

Muhammed Rasi M, K. P. Zuhail, Arun Roy, Surajit Dhara. " phase transitions probed by a pair of elastically bound colloids ", Physical Review E. 2018

Publication

Dr. Surajit Dhara Professor School of Physics University of Hyderabad Hyderabad-500 046, INDIA.

Muhammed Rasi M, Ravi Kumar Pujala, Surajit Dhara. "Colloidal analogues of polymer chains, ribbons and 2D crystals employing orientations and interactions of nano-rods dispersed in a nematic liquid crystal", Scientific Reports, 2019

Dr. Surajit Dhara Professor School of Physics University of Hyderabad Hyderabad-500 046, INDIA.

4

www.nature.com

Internet Source

Publication

Dr. Surajit Dhara

Professor School of Physics University of Hyderabad Hyderabad-500 046. INDIA.

5	Paul Bartlett, Stuart I. Henderson, Stev. "Measurement of the hydrodynamic forces between two polymer-coated spheres", Philosophical Transactions of The Royal Society A Mathematical Physical and Engineering Sciences, 05/15/2001 Publication	1 %
6	Submitted to Indian Institute of Technology, Kharagpure Student Paper	1 %
7	dspace.rri.res.in Internet Source	1 %
8	Igor Muševič. "Liquid Crystal Colloids", Springer Science and Business Media LLC, 2017 Publication	1 %
9	Submitted to University of Hyderabad, Hyderabad Student Paper	<1%
10	D. Demus, J. Goodby, G. W. Gray, H W. Spiess, V. Vill. "Handbook of Liquid Crystals Set", Wiley, 1998 Publication	<1%
11	etheses.whiterose.ac.uk Internet Source	<1%
12	opticaltweezers.blogspot.com Internet Source	<1%

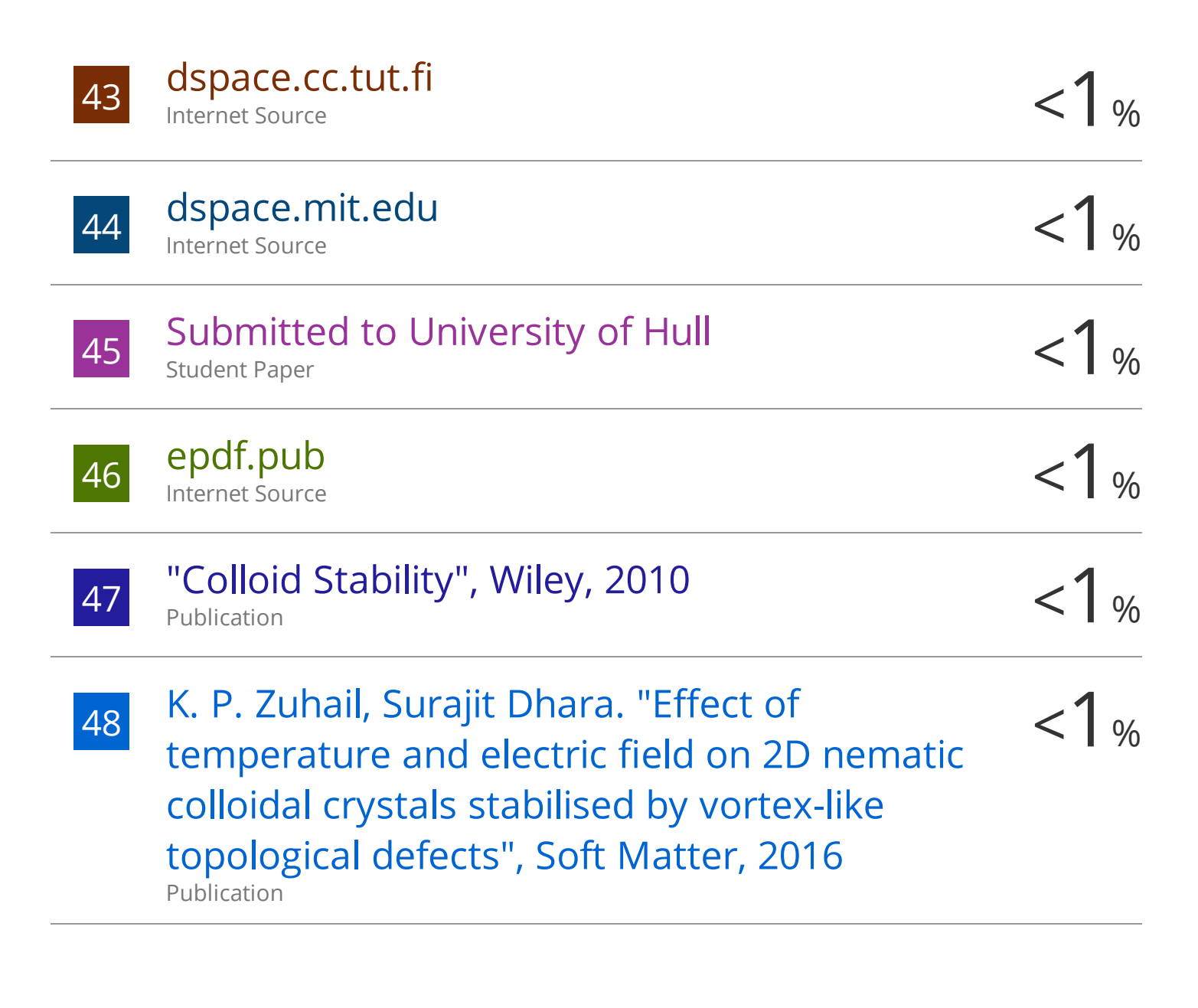
13	B. I. Lev. "Symmetry breaking and interaction of colloidal particles in nematic liquid crystals", Physical Review E, 01/2002 Publication	<1%
14	Chanjoong Kim, Souptik Mukherjee, Paul Luchette, Peter Palffy-Muhoray. "Director Orientation in Deformed Liquid Crystal Elastomer Microparticles", Soft Materials, 2014 Publication	<1%
15	www.ncbi.nlm.nih.gov Internet Source	<1%
16	B. I. Lev. "Symmetry Breaking, Elastic Interaction and Structures in Nematic Colloids", Molecular Crystals and Liquid Crystals, 1/1/2004 Publication	<1%
17	K. P. Zuhail, Surajit Dhara. "Temperature dependence of equilibrium separation and lattice parameters of nematic boojum-colloids", Applied Physics Letters, 2015	<1%
18	Submitted to University College London Student Paper	<1%
19	etheses.dur.ac.uk Internet Source	<1%

20	qmro.qmul.ac.uk Internet Source	<1%
21	C. P. Lapointe. "Shape-Controlled Colloidal Interactions in Nematic Liquid Crystals", Science, 11/20/2009	<1 %
22	"Handbook of Visual Display Technology", Springer Science and Business Media LLC, 2016 Publication	<1%
23	Shah, R.R "Meso-scale imaging of patterned surfaces by decoration with liquid crystals", Colloids and Surfaces A: Physicochemical and Engineering Aspects, 20001115 Publication	<1%
24	Patrick Oswald. "Dynamics of Dislocations in Smectic A Liquid Crystals Doped with Nanoparticles", Crystals, 2019 Publication	<1%
25	publications.rwth-aachen.de Internet Source	<1%
26	P. Zoller, G. Alber, R. Salvador. "ac Stark splitting in intense stochastic driving fields with Gaussian statistics and non-Lorentzian line shape", Physical Review A, 1981 Publication	<1%
	www.lps.ens.fr	

27	Internet Source	<1%
28	Tkalec, UroÅi, Miha Å karabot, and Igor MuÅieviÄI. "Interactions of micro-rods in a thin layer of a nematic liquid crystal", Soft Matter, 2008.  Publication	<1%
29	V. A. Raghunathan, P. Richetti, D. Roux. "Dispersion of Latex Particles in a Nematic Solution. 2. Phase Diagram and Elastic Properties", Langmuir, 1996 Publication	<1%
30	Waigh, Thomas Andrew. "Advances in the microrheology of complex fluids", Reports on Progress in Physics, 2016. Publication	<1%
31	arxiv.org Internet Source	<1%
32	B. Lev, H. Yokoyama. "Theory of Interaction and Structure Formation in Liquid Crystal Colloids and Emulsion", Molecular Crystals and Liquid Crystals, 2005 Publication	<1%
33	M. V. Rasna, K. P. Zuhail, U. V. Ramudu, R. Chandrasekar, J. Dontabhaktuni, Surajit Dhara. "Orientation, interaction and laser assisted self-assembly of organic single-	<1%

### crystal micro-sheets in a nematic liquid crystal", Soft Matter, 2015 Publication

34	Submitted to University of Strathclyde  Student Paper	<1%
35	Holger Stark. "Physics of colloidal dispersions in nematic liquid crystals", Physics Reports, 2001  Publication	<1%
36	Submitted to Glasgow Caledonian University Student Paper	<1%
37	Submitted to IIT Delhi Student Paper	<1%
38	jscholarship.library.jhu.edu Internet Source	<1%
39	Kruger, G.J "Diffusion in thermotropic liquid crystals", Physics Reports, 198202 Publication	<1%
40	S. Chandrasekhar, G.S. Ranganath. "The structure and energetics of defects in liquid crystals", Advances in Physics, 1986 Publication	<1%
41	core.ac.uk Internet Source	<1%
42	d-nb.info Internet Source	<1%



Exclude quotes On Exclude bibliography On

Exclude matches

< 14 words

#### Plagiarism-free statement

This is to certify that the thesis titled "Interaction, directed assembly and electrophoretic mobility of silica micro and nano-rods in nematic liquid crystals" has been screened by the Turnitin software at the Indira Gandhi Memorial Library of the University of Hyderabad. The software shows a 40% similarity index, out of which 32% came from the candidate's own three research articles related to this thesis, which are already published and available online. Thus, the effective similarity index excluding his research articles is 40% - 32% = 8%, which is lower than the 10% stipulated by the university guidelines. Therefore, this thesis is free from plagiarism.

Prof. Surajit Dhara

Thesis Supervisor

School of Physics

University of Hyderabad

Dr. Surajit Dhara
Professor
School of Physics
University of Hyderabad
Hyderabad-500 046. INDIA.

Date: 16/11/2021